Master's thesis

NTNU
Norwegian University of Science and Technology
Faculty of Natural Sciences
Department of Materials Science and Engineering

Hanna Kvam Herskedal

Sintering Properties and Li-ion Conductivity of Solid-State Electrolytes with Composition $Li_{7-x}La_3Zr_{2-x}Ta_xO_{12}$ (x=0.25 and x=0.6)

Master's thesis in Chemical Engineering and Biotechnology
Supervisor: Kjell Wiik
Co-supervisor: Leif Olav Jøsang and Mari-Ann Einarsrud
June 2022

NTNU
Norwegian University of Science and Technology

Hanna Kvam Herskedal

Sintering Properties and Li-ion Conductivity of Solid-State Electrolytes with Composition $Li_{7-x}La_3Zr_{2-x}Ta_xO_{12}$ (x=0.25 and x=0.6)

Master's thesis in Chemical Engineering and Biotechnology
Supervisor: Kjell Wiik
Co-supervisor: Leif Olav Jøsang and Mari-Ann Einarsrud
June 2022

Norwegian University of Science and Technology
Faculty of Natural Sciences
Department of Materials Science and Engineering

NTNU
Norwegian University of
Science and Technology

Preface

This master's thesis was written during the spring semester of 2022 at the Department of Materials Science and Engineering at the Norwegian University of Science and Technology (NTNU). The final thesis is submitted as part of the course TMT4900 - Materials Chemistry and Energy Technology, Master's Thesis.

I would like to express my greatest gratitude towards my supervisor Kjell Wiik for exceptional guidance and feedback throughout the work on this thesis. I would also like to thank my co-supervisors Leif Olav Jøsang at Cerpotech AS and Mari-Ann Einarsrud at NTNU for always showing interest and providing useful input. Your insight and experience has been invaluable. Thank you to everyone in the FACET battery group for sharing your knowledge and creating a great environment for learning. I am also deeply grateful to my family for their unconditional support. Finally, I would like to thank my fellow students for five unforgettable years. Thank you for all the experiences we have shared and for the motivation you provided me with during these amazing, but also demanding, times.

Hanna Kvam Herskedal

Trondheim, June 2022

Abstract

Recently, there has been a growing interest in solid-state electrolytes as potential substitutes for the liquid organic electrolytes employed in current Li-ion batteries. Application of solid-state electrolytes will improve battery safety, as well as allow for the use of high-capacity Li metal anodes. $Li_7La_3Zr_2O_{12}$ (LLZO) is a promising solid-state material due to its high Li-ion conductivity and chemical stability. This work investigated Ta-doped LLZO produced by spray pyrolysis. Two different compositions were studied, namely $Li_{6.75}La_3Zr_{1.75}Ta_{0.25}O_{12}$ and $Li_{6.4}La_3Zr_{1.4}Ta_{0.6}O_{12}$. The powders contained a Li excess of 24.2 mol% to compensate for Li loss. Sintering experiments were carried out in ambient air at 1150 °C, and the phase composition, microstructure, density, and ionic conductivity of the sintered samples were assessed. A high Li loss resulted in the formation of a $La_2Zr_2O_7$ secondary phase, which was found to reduce the ionic conductivity. Sintering of $Li_{6.4}La_3Zr_{1.4}Ta_{0.6}O_{12}$ samples for 6 h in MgO crucibles resulted in pure cubic Ta-doped LLZO without secondary phases. The samples were covered in a bed powder to prevent undesired reactions and provide extra Li as compensation for Li loss. This sintering program achieved the highest total ionic conductivity of $1.66 \cdot 10^{-4}$ S cm^{-1} and a relative density of 92 %.

Sammendrag

Den siste tiden har det vært en økende interesse for faststoffelektrolytter som potensielle erstatninger for de flytende organiske elektrolyttene som brukes i nåværende Li-ion-batterier. Bruk av faststoffelektrolytter vil forbedre batterisikkerheten, samt tillate bruk av Li-metallanoder med høy kapasitet. $Li_7La_3Zr_2O_{12}$ (LLZO) er et lovende faststoffmateriale på grunn av dets høye Li-ion-ledningsevne og kjemiske stabilitet. Dette arbeidet undersøkte Ta-dopet LLZO produsert ved spraypyrolyse. To ulike sammensetninger ble studert, nemlig $Li_{6.75}La_3Zr_{1.75}Ta_{0.25}O_{12}$ og $Li_{6.4}La_3Zr_{1.4}Ta_{0.6}O_{12}$. Pulverne inneholdt et Li-overskudd på 24,2 mol% for å kompensere for tap av Li. Sintringseksperimenter ble utført i åpen ovn ved 1150 °C, og fasesammensetning, mikrostruktur, tetthet og ionisk ledningsevne av de sintrede prøvene ble evaluert. Et høyt Li-tap resulterte i dannelse av en $La_2Zr_2O_7$-sekundærfase som reduserte den ioniske ledningsevnen. Sintring av $Li_{6.4}La_3Zr_{1.4}Ta_{0.6}O_{12}$ prøver i 6 timer i MgO-digler resulterte i ren kubisk Ta-dopet LLZO uten sekundære faser. Prøvene var dekket med et beskyttende pulver (≪bed powder≫) for å fohindre uønskede reaksjoner og tilføre ekstra Li som kompensasjon for Li-tap. Dette sintringsprogrammet gav den høyeste totale ioniske ledningsevnen på $1{,}66 \cdot 10^{-4}$ S cm^{-1}, og en relativ tetthet på 92 %.

Table of Contents

Abbreviations

AGG Abnormal grain growth

BP-ratio Bed powder ratio

CIP Cold isostatic pressing

EIS Electrochemical impedance spectroscopy

HT High temperature

LLZO $Li_7La_3Zr_2O_{12}$

LT Low temperature

RD Relative density

SEM Scanning electron microscopy

VLC Volatile lithium compound

XRD X-ray diffraction

List of Figures

List of Tables

1 Introduction

1.1 Background and motivation

The rising challenge of global warming and limited fossil fuel supplies have certainly sparked a worldwide interest in developing renewable sources of energy. High-power, low-cost, and efficient energy storage and conversion technologies are needed in the transition from current carbon-based fossil fuels to sustainable electrical energy [1]. This requires availability of suitable energy storage systems, namely, batteries. Lithium-ion batteries are currently dominating as the power source for portable electronic devices, such as computers, cell phones, and electric vehicles. By offering high energy density, high cell potential and design flexibility [2], they represent the state-of-the-art with respect to portable applications.

While the use of Li-ion batteries has experienced an impressive worldwide growth, their limitations have become more evident. Conventional Li-ion batteries containing liquid organic electrolytes suffer from safety issues such as flammability and leakage [1, 3]. Overheating the battery can cause the electrolyte to decompose exothermally due to thermal instability. This can lead to thermal runaway, which can further induce serious safety problems like smoke, fire and explosion [4].

The anodes of present Li-ion batteries are mostly based on graphite, where Li-ions are intercalated into the layered structure. Yet, better electrochemical performance is needed to fulfill the increasing demands of high-power electrochemical energy storage systems [5]. Li metal is a promising anode material for rechargeable batteries due to its extremely high specific capacity [6]. However, Li metal anodes combined with liquid organic electrolytes give rise to the issue of uncontrollable Li dendrite growth. Formation of dendrites may cause safety concerns and capacity loss in the battery [7–9].

In order to overcome the problems related to safety and dendritic growth, the liquid electrolyte can be replaced by a solid-state electrolyte. Inorganic solid-state electrolytes are non-flammable, and their thermal stability eliminates the risk of thermal runaway. Furthermore, solid-state electrolytes act as mechanical obstacles to dendrite growth [10].

The dendrite suppression allows for implementation of Li metal anodes, which further increases the energy density of the battery. Figure 1.1 shows the difference between a solid-state electrolyte battery and a liquid electrolyte battery. The solid electrolyte works as both the ionic conductor and the separator in the solid-state battery, and it offers a simpler cell structure and a safer battery [3].

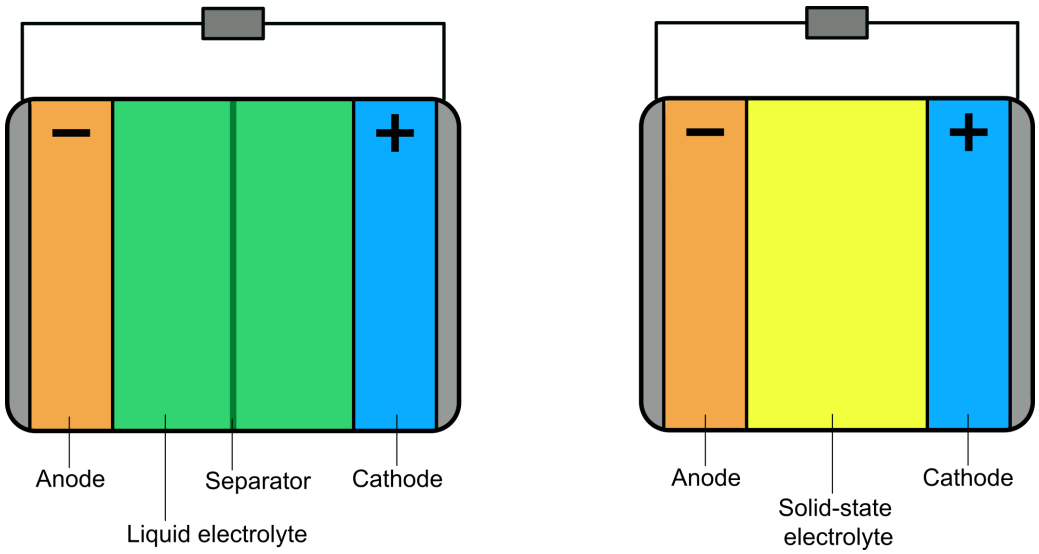

Figure 1.1: Liquid electrolyte Li-ion battery (left) and solid-state Li-ion battery (right).

Among various solid-state electrolytes, Tantalum-doped $Li_7La_3Zr_2O_{12}$ is a promising material for use in solid Li-ion batteries. It is an inorganic, ceramic compound based on garnet-type $Li_7La_3Zr_2O_{12}$ (LLZO). Ta-doped LLZO stands out due to its high Li^+ conductivity, negligible electronic conductivity, high chemical stability against Li metal, and wide electrochemical stability range [8, 11, 12]. To achieve a material with optimal electrolytic properties and good mechanical strength, the Ta-doped LLZO must acquire high phase purity, high density, and a homogeneous microstructure with small grains. Thus, it is essential to establish a suitable process for synthesizing high-quality LLZO solid-state electrolytes.

1.2 Aim and scope

In this work, the sintering properties and Li-ion conductivity of Ta-doped $Li_7La_3Zr_2O_{12}$ produced by spray pyrolysis will be investigated. The aim is to establish a sintering procedure for producing high-quality, single-phased Ta-LLZO with a dense microstructure and good ionic conductivity, suitable for use as a solid-state electrolyte. A systematic sintering study, carried out in ambient air, will be conducted to determine the optimal conditions. Both sintering time, crucible material, and amount of bed powder will be considered. In addition, the effect of Ta content on microstructure, density, and ionic conductivity of sintered samples will be studied. The sintering behavior will be established by dilatometry analysis, and the microstructure of sintered pellets will be characterized by scanning electron microscopy (SEM). Archimedes' method will be used to measure the pellet density, and the phase composition will be determined by X-ray diffraction (XRD). The ionic conductivity will be measured by electrochemical impedance spectroscopy (EIS).

2 Literature Review

The following section covers the theoretical background needed to appreciate the experimental work, results, and discussion in this thesis. The structure of the LLZO system is outlined in detail, followed by a presentation of the thermodynamics. Then, the section focuses on the effects of doping, with special attention to Ta as dopant, before the topic of secondary phases is presented in depth. Finally, sintering of Ta-doped LLZO and Li^+ conductivity is covered. The content is partly based on the theory section in the specialization project by Herskedal [13].

2.1 LLZO structure

$Li_7La_3Zr_2O_{12}$ (LLZO) is a garnet-like compound with the general formula $A_3B_2C_3O_{12}$, where A, B and C are cations in 8-coordinated, octahedral and tetrahedral lattice sites, respectively. The structure consists of La^{3+} at A-sites, Zr^{4+} at B-sites, and Li^+ at C-sites and interstitial sites. As opposed to other garnets, LLZO has four additional Li^+ ions at interstitial sites, providing the formula unit [11, 14].

LLZO exhibits two crystal structures, namely cubic (c-LLZO) and tetragonal (t-LLZO). The cubic structure (space group $Ia\bar{3}d$) is a disordered structure, in which Li^+ partly occupies the tetrahedral 24d and octahedral 96h sites. Figure 2.1 shows the structural arrangement of the cubic structure, where Li(1) and Li(2) denote Li on the 24d and 96h lattice sites, respectively. The tetragonal structure (space group $I4_1/acd$) is an ordered structure, where Li^+ fully occupy the tetrahedral 8a site, and the octahedral 16f and 32g sites [11, 15], as shown in Figure 2.2. Here, Li(1) is in the 8a tetrahedral site, connected to four oxygen atoms, and Li(2) and Li(3) are in the 16f and 32g octahedral sites, respectively, where both are connected to six oxygen atoms [15, 16]. Both garnet crystal symmetries are built of the same structural framework, where ZrO_6-octahedrons and LaO_8-dodecahedrons are connected to form the structure. The differences in Li-ion distribution of the two structures strongly affect the lithium diffusion mechanism and ionic conductivity [17]. Detailed unit cell crystal structures are shown in Figure G.1 in Appendix G.

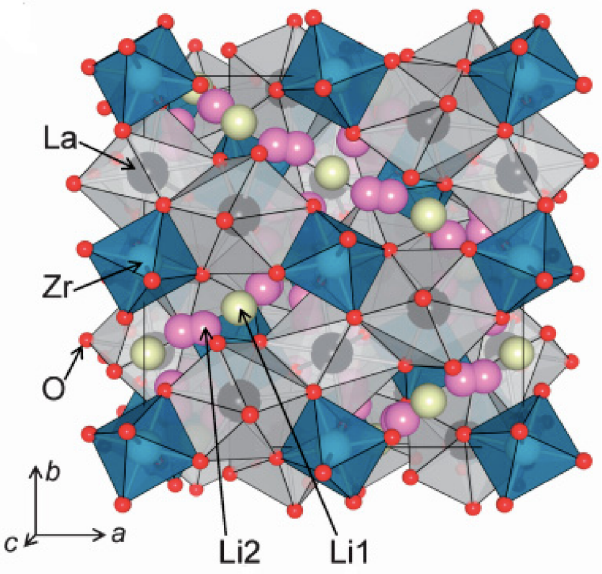

Figure 2.1: Crystal structure of cubic LLZO. The yellow spheres represent the 24d tetrahedral sites, occupied by Li(1) ions, and the pink spheres represent the 96h octahedral sites, occupied by Li(2) ions. Reprinted from [18].

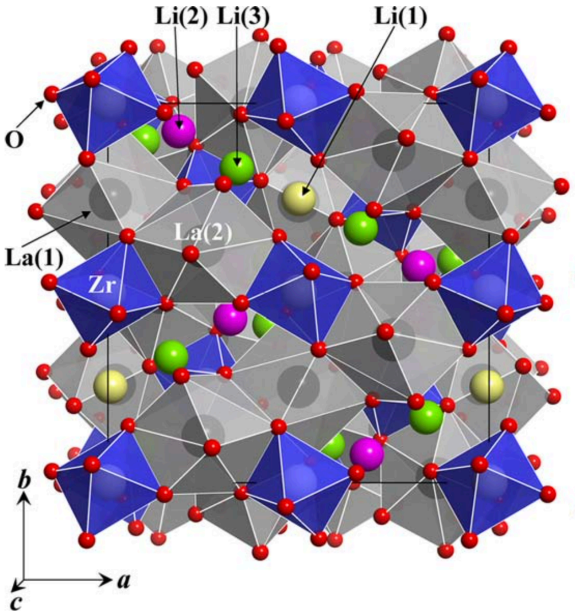

Figure 2.2: Crystal structure of tetragonal LLZO. The yellow spheres represent 8a tetrahedral sites, occupied by Li(1) ions, the pink spheres represent the 16f octahedral sites, occupied by Li(2) ions, and the green spheres represent the 32g octahedral sites, occupied by Li(3) ions. Reprinted from [19].

The LLZO structure consists of a connection of multiple loops that make up the lithium diffusion pathway in the solid electrolyte. The loops are composed of lithium ions, as shown in Figure 2.3, where g denotes the occupancy of each site [16]. In the tetragonal structure, the Li sites are completely ordered with a site occupancy of 1 for each site. This means that all sites available for Li-ions are filled, and the Li-ions are arranged such that they are not interconnected to create a pathway for movement. The cubic structure, however, has a disordered arrangement of Li^+ and the Li-site occupancy is less than 1. The Li sites are only partially filled, providing vacancies available for movement of Li-ions. Thus, the cubic crystal structure has more sites available for Li migration compared to the tetragonal structure. The large number of Li vacancies and the disordered Li sublattice in the cubic LLZO facilitate lower activation energy for transport of Li-ions along the diffusion pathway. Consequently, the Li^+ conductivity of the cubic structure is enhanced to at least two orders of magnitude compared to the tetragonal structure [15, 20]. Hence, understanding and monitoring the crystal structure is highly important for quality control of LLZO as an electrolyte.

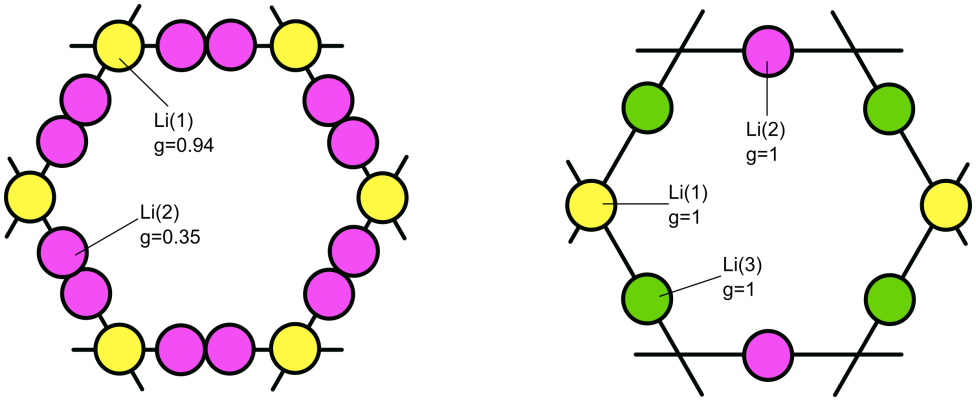

Figure 2.3: Arrangement of lithium sites in cubic (left) and tetragonal (right) LLZO [16]. The loop structure gives the conduction channel for Li^+ in the structure. g denotes the occupancy for each site.

2.2 Thermodynamics of LLZO

LLZO can occur in three distinct phases. Two of them are cubic, identified as high-temperature (HT) cubic and low-temperature (LT) cubic, and one is tetragonal. The HT-cubic phase with disordered Li sites exhibits a high ionic conductivity of $> 10^{-4}$ S

cm^{-1} [3, 14]. Every occurrence of the cubic structure in this thesis refers to the HT-cubic phase, unless stated otherwise. The LT-cubic phase is formed by reactions with H_2O or CO_2 in the surrounding atmosphere and has a much lower ionic conductivity of about 10^{-6} S cm^{-1} [14, 17, 21]. The tetragonal phase shows poor ionic conductivity in the same range as the LT-cubic phase [19]. Thus, it is crucial to understand the phase stability of LLZO.

2.2.1 Undoped LLZO

Usually for garnets, the thermodynamically stable structure at room temperature is the cubic LLZO phase. However, the stable structure of undoped LLZO at room temperature is the tetragonal [14, 17, 21–23]. The tetragonal phase stability is driven by the ordered arrangement of Li-ions. When the Li sites are completely ordered, the Coulombic repulsion between adjacent Li-ions decreases, which leads to a reduction in the free energy of the system. This ordering will also distort the ZrO_6 octahedrons as they return to their preferential high-symmetry shape. The unfavorable distortion of the crystal structure reduces the internal structural strain and causes formation of the tetragonal structure in order to maintain optimal bond angles. The ordering of the Li-ions and the cubic-tetragonal transition are simultaneous processes, where neither one takes place spontaneously without the other [24]. The tetragonal stability depends on the occurrence of both these processes. However, the cubic LLZO structure is preferred as it has the highest ionic conductivity, and several studies have reviewed how the transition from tetragonal to cubic can be induced.

The phase stability of LLZO is controlled by the free energy of the system. The tetragonal structure will spontaneously transform into the cubic structure when the free energy becomes negative. Equation 2.1 gives the expression for the tetragonal-cubic phase transition, where $\Delta G_{t\to c}$ is the free energy, $\Delta H_{t\to c}$ is the enthalpy, $\Delta S_{t\to c}$ is the entropy, and T is the absolute temperature.

$$\Delta G_{t\to c} = \Delta H_{t\to c} - T\Delta S_{t\to c} \tag{2.1}$$

The tetragonal and cubic structures have different entropies because one is ordered and the other disordered, meaning that their free energies will cross at a given temperature [24]. The disordered Li arrangement of the cubic structure yields higher entropy than the ordered tetragonal structure. Consequently, the reaction entropy for the tetragonal-cubic transformation, $\Delta S_{t\rightarrow c}$, is positive, verifying that the free energy shifts to a negative value at a specific temperature. The temperature where the free energy of transition is 0 is called the transition temperature [24].

Several studies have carried out research on the tetragonal-cubic transition temperature in undoped LLZO. Both Matsui *et al.* [21] and Larraz *et al.* [23] used high-temperature XRD to determine a phase transition temperature of 650 °C. In comparison, Janani *et al.* [25] found that the tetragonal LLZO phase transformed into the cubic phase at 700 °C by using conventional X-ray powder diffraction.

In undoped LLZO, the cubic phase undergoes a rather fast transition back to the tetragonal phase upon quenching to room temperature. Consequently, the cubic phase will not be retained when room temperature is reached. Since only the tetragonal phase with poor conductivity is stable at lower temperatures, undoped LLZO is not suitable as a solid electrolyte. However, introducing dopants into the LLZO system will lead to a slower phase transition process, so that quenching from high temperature can suppress the formation of the tetragonal phase and thereby preserve the HT-cubic phase [26].

It is important to mention that several papers have reported on undoped LLZO with a cubic crystal structure. This may be due to the high sensitivity to contamination, where exposure to CO_2 or H_2O in the atmosphere leads to stabilization of the LT-cubic phase at room temperature. Another issue is the accidental incorporation of alumina, e.g. from alumina crucibles, which can contribute to stabilizing the cubic LLZO [1, 27, 28]. In addition, there are concerns regarding the volatilization of Li, which can cause a high Li loss. Li deficiency in LLZO can lead to the formation of secondary phases, such as $La_2Zr_2O_7$, and thus, proper control of the Li amount is required [29]. Addition of extra Li to compensate for Li loss at high temperatures, as well as limiting air exposure, and using inert crucibles, are all important precautions [30].

2.2.2 Effects of dopants on LLZO

As stated, thermodynamic instability of the cubic phase in undoped LLZO at room temperature leads to the formation of the tetragonal phase with poor Li^+ conductivity. High ionic conductivity is crucial for solid-state electrolytes, and thus, stabilization of the cubic phase has gained considerable attention in LLZO research. Super valent doping is one of the most effective strategies for stabilizing the cubic phase and thereby improving the ionic conductivity [16]. This is achieved by introducing super valent cations to the LLZO crystal structure. Different cations favor different substitution sites, and they can either substitute for the Li^+, La^{3+} or Zr^{4+} site. The positive charge from the dopant cation leads to formation of Li vacancies so that electroneutrality is preserved. The Li vacancies will cause an increase in the average Li-Li interatomic distance and a decrease in the repulsive forces. The overall entropy will increase, and subsequently, the free energy gained from ordering the Li ions will be reduced [24]. The disorder of the Li^+ arrangement in the lattice will prevent the tetragonal distortion. Instead, the high-conductivity cubic phase will be stabilized [16].

Various cations have been studied as dopants, such as Al^{3+} and Ga^{3+} substituted on the Li-site, and Nb^{5+} and Ta^{5+} on the Zr-site [28]. Al^{3+} is a common dopant that appears in many studies, and it was early discovered to originate from contamination from Al_2O_3 crucibles [20, 27]. Geiger *et al.* [27] noticed that the unintentional doping of Al from crucibles into the LLZO structure during sintering at high temperature contributed to stabilize the cubic phase. Later, the impact of Al was studied by intentionally incorporating Al into the LLZO framework. The trivalent Al^{3+} ion occupies the Li^+ site, yielding two Li vacancies as charge compensation. Incorporation of Al^{3+} will thereby stabilize the cubic phase. Various studies have reported high values for the ionic conductivity of Al-doped LLZO. Tian *et al.* [12] published $3.08 \cdot 10^{-4}$ S cm^{-1} as the ionic conductivity, Matsuda *et al.* [14] found a value of $3.1 \cdot 10^{-4}$ S cm^{-1}, and Rangasamy *et al.* [31] reported a value of $4 \cdot 10^{-4}$ S cm^{-1}.

Although Al doping can give rise to LLZO with high ionic conductivity, undesired phases, such as Li_5AlO_4 and $LaAlO_3$, can form at higher doping levels [20, 32]. This will lead to an overall lower ionic conductivity. In addition, it has been reported that substitution on the

Li^+ site can reduce the Li mobility. Al^{3+} substituted at the Li^+ site can act as obstacles and block the Li^+ conduction pathway. This will obstruct the transport of Li-ions along this path and thereby reduce the ionic conductivity [20, 33].

2.2.3 Ta-doped LLZO

The challenges arising from blocking the Li^+ conduction pathways by Al-doping have drawn the attention towards cations substituting on the Zr^{4+} site. Tantalum (Ta^{5+}) is a pentavalent cation that has gained a lot of interest due to the high ionic conductivity of $\geq 1.0 \cdot 10^{-3}$ S cm^{-1} in Ta-doped LLZO [11, 33, 34]. Ta^{5+} has an ionic radius of 72 pm (c.n.= 6), which is comparable to the ionic radius of 64 pm (c.n.= 6) for Zr^{4+} [35]. When Ta^{5+} is doped into LLZO, Ta^{5+} substitutes on the Zr^{4+} site, resulting in the formation of equivalent Li^+ vacancies. This is demonstrated in Equation 2.2, where M_S^C represents species M at site S with relative charge C, "$\cdot$" denotes the positive charge of Ta^{5+} relative to the charge of Zr^{4+}, and V'_{Li} is a vacancy created on a Li^+-site (notation in accordance with Kröger-Vink).

$$Ta_2O_5 \rightarrow 2Ta^{\cdot}_{Zr} + 2V'_{Li} + 5O_O \tag{2.2}$$

The general formula of the resulting Ta-LLZO garnet is $Li_{7-x}La_3Zr_{2-x}Ta_xO_{12}$. Bernstein *et al.* [24] suggested that a critical Li vacancy concentration of 0.4-0.5 moles per LLZO formula unit is needed to stabilize the cubic phase of LLZO. This prediction has been experimentally confirmed to apply for Al^{3+} doping on the Li^+ site. Rangasamy *et al.* [31] stated that a minimum of 0.204 moles of Al in LLZO is necessary for cubic phase stabilization at room temperature. A stable cubic phase has been attained by substituting Ta for Zr, without the presence of Al [33]. Therefore, the amount of Ta in the LLZO structure is a central aspect to consider when it comes to the sintering properties, microstructure, and ionic conductivity of Ta-doped LLZO.

In literature, disagreements exist about the critical amount of Ta^{5+} required to stabilize the cubic Ta-LLZO and obtain a high ionic conductivity. Li *et al.* [34] observed a high ionic conductivity of $1.0 \cdot 10^{-3}$ S cm^{-1} at a Ta doping level of x=0.6, and a lower

conductivity of $2.8 \cdot 10^{-4}$ S cm^{-1} at x=0.2. In contrast, Wang and Lai [36] reported a higher ionic conductivity at x=0.2 ($7.3 \cdot 10^{-3}$ S cm^{-1}) compared to higher doping levels. Allen *et al.* [33] also found a high ionic conductivity for lower doping levels ($8.7 \cdot 10^{-3}$ S cm^{-1} at x=0.25). This demonstrates the controversy regarding the effect of the Ta doping level on the total Li^+ conductivity. The Li^+ conductivity also strongly depends on the samples' relative density, the sintering temperature, the holding time, and the presence of Al_2O_3 during sintering. The compositions of Ta-doped LLZO in this study are $Li_{6.75}La_3Zr_{1.75}Ta_{0.25}O_{12}$ and $Li_{6.4}La_3Zr_{1.4}Ta_{0.6}O_{12}$, which are both frequently referred to in literature. Detailed unit cell crystal structures of the cubic phases are shown in Figure G.2 in Appendix G.

2.3 Secondary phases

A potential issue is the presence of unfavorable secondary phases in the LLZO system. Such phases may reduce the ionic conductivity and weaken the performance of LLZO as a solid-state electrolyte. Thus, understanding how they occur and how they can be avoided is crucial for obtaining high-quality single-phased cubic LLZO.

2.3.1 LLZO

One of the secondary phases that may form in the LLZO system is the tetragonal LLZO, which is a phase with ordered Li^+ arrangement and low ionic conductivity. The tetragonal phase may also appear in doped LLZO if there is a large excess of Li. Controlled loss of Li during heat treatment in sufficiently doped LLZO will decrease the Li content and lead to a tetragonal-cubic transformation. The tetragonal phase can be distinguished from the cubic phase by X-ray diffraction. The cubic structure shows single peaks for each Bragg reflection, while the tetragonal structure shows two distinct peaks. These two peaks usually appear as a split peak, as their 2θ values are close. If only the tetragonal phase is present, it is expected to see only split peaks. If there is a mixture of tetragonal and cubic phase, three peaks can be observed [28]. It is important to note that peak splitting at higher 2θ values may be caused by CuKα_2 radiation. It should not be confused with

the peak splitting due to the presence of tetragonal phase.

Another secondary phase is the LT-cubic LLZO, a low-conductivity phase formed at low temperatures. This phase has the same space group as the HT-cubic phase, and their X-ray diffraction patterns are similar. However, the lattice parameter of the LT-cubic phase is slightly larger than that of the HT-cubic phase [14, 21]. The LT-cubic phase appears when tetragonal LLZO reacts with H_2O or CO_2 in the atmosphere at temperatures below 400 °C [14, 37]. H_2O and CO_2 can individually induce the transformation from tetragonal to LT-cubic [30], and the rate of absorption is highest at temperatures around 100-200 °C [23]. This is consistent with the study by Matsui *et al.* [21], who observed absorption of CO_2 in Al-free LLZO at around 100-200 °C, resulting in the formation of the LT-cubic phase. They found that at temperatures between 450 and 650 °C, the absorbed CO_2 was extracted, and the phase transformed back to the tetragonal phase. Subsequently, the HT-cubic phase was observed above 700 °C, with small amounts of $La_2Zr_2O_7$ and La_2O_3. However, after cooling to room temperature, the cubic phase transformed back to the tetragonal phase. This may indicate that the CO_2 extraction was completed. A similar transition from tetragonal to LT-cubic phase has been observed for doped LLZO through natural aging in air after storage in ambient conditions. This transition occurs, however, at a much lower rate [23, 38]. The formation of the LT-cubic LLZO phase can be reduced by minimizing the air exposure, which is especially important at temperatures where the rate of incorporation of H_2O and CO_2 are high. In addition, LLZO samples should ideally be stored in an inert atmosphere to reduce the LT-cubic formation due to aging.

Li_2CO_3 is an intermediate phase that might be added as the Li source during LLZO synthesis. Li_2CO_3 can also appear when other Li sources are used, as it is formed during spray pyrolysis when carbon is present. The formation of cubic LLZO is highly dependent on the availability of Li, which is determined by the decomposition of Li_2CO_3. The mechanism occurs in two steps, as evidenced by Herskedal [13]. First, Li_2CO_3 decomposes into nanocrystalline Li_2O, according to Equation 2.3. Subsequently, Li_2O reacts with $La_2Zr_2O_7$ and La_2O_3 to form LLZO, as shown in Equation 2.4.

$$Li_2CO_3\,(s, l) \rightarrow Li_2O\,(s) + CO_2\,(g) \tag{2.3}$$

$$7Li_2O\ (s) + 2La_2Zr_2O_7 + La_2O_3 \rightarrow 2Li_7La_3Zr_2O_{12} \tag{2.4}$$

Even though the melting temperature of Li_2CO_3 is 723 °C, the decomposition of Li_2CO_3 begins at lower temperatures. However, the partial pressure of CO_2 (g) is low at temperatures below the melting temperature, and consequently, the reaction rate of the decomposition reaction in Equation 2.3 is low. Therefore, temperatures above 723 °C is essential for obtaining a higher reaction rate of the Li_2CO_3 decomposition [13]. Both Li_2CO_3 (s) and Li_2CO_3 (l) can decompose into Li_2O (s), but from the work by Herskedal [13] it was evidenced that the reaction rate of the decomposition increases significantly when the molten phase of Li_2CO_3 (l) is formed. The completion of the decomposition of Li_2CO_3 depends on the transport of CO_2 (g). The CO_2 gas must be removed for the reaction to fully take place. If the CO_2 (g) is not sufficiently transported out of the powder, the CO_2 (g) partial pressure will be high, and the decomposition rate of Li_2CO_3 will be lower.

Paolella *et al.* [29] have suggested an alternative reaction mechanism where molten Li_2CO_3 reacts with $La_2Zr_2O_7$ and La_2O_3 to form LLZO, according to Equation 2.5. They stated that it is not Li_2O that reacts to form LLZO, but the molten Li_2CO_3.

$$7Li_2CO_3\ (l) + 2La_2Zr_2O_7 + La_2O_3 \rightarrow 2Li_7La_3Zr_2O_{12} + 7CO_2\ (g) \tag{2.5}$$

$La_2Zr_2O_7$ is a common secondary phase that commonly arises from Li deficiency. Formation of $La_2Zr_2O_7$ at high temperatures (> 1000 °C) usually originates from loss of Li and insufficient Li from the Li source [11]. The ZrO_2-La_2O_3 phase diagram, shown in Figure 2.4, indicates that $La_2Zr_2O_7$ is a potential phase in this system. According to the phase diagram, a solid solution is formed, which may affect the XRD analysis as the cell parameters slightly change. Equation 2.6 shows the reaction between La_2O_3 and ZrO_2 that forms $La_2Zr_2O_7$ [26]. LLZO is formed when $La_2Zr_2O_7$ reacts with La_2O_3 and Li_2O, according to Equation 2.4.

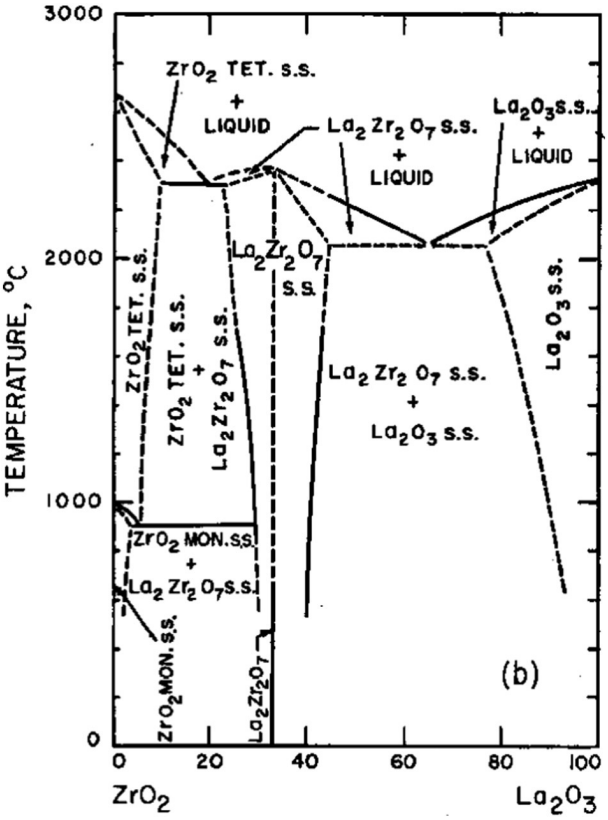

Figure 2.4: Phase diagram of the ZrO_2-La_2O_3 system. Reprinted from [39].

$$La_2O_3 + 2ZrO_2 \rightarrow La_2Zr_2O_7 \tag{2.6}$$

During heat treatment at high temperature, Li will evaporate, resulting in LLZO with insufficient Li content [12, 26]. A high Li loss promotes a transformation of LLZO back to $La_2Zr_2O_7$, according to the Equation 2.7. Therefore, adding an excess of Li to the powders will compensate for Li loss at high temperatures, giving less formation of $La_2Zr_2O_7$. Li can also be supplied by using a bed powder during sintering.

$$2Li_7La_3Zr_2O_{12} \rightarrow 2La_2Zr_2O_7 + 7Li_2O + La_2O_3 \tag{2.7}$$

La_2O_3 is a possible precursor for the LLZO synthesis, but it may appear even when other La-containing sources are used. La_2O_3 takes part in the formation of LLZO, as shown in Equation 2.4. Many studies have found residuals of unreacted La_2O_3 after heat treatment [23, 26, 40, 41]. The presence of $La_2Zr_2O_7$ and small amounts of La_2O_3

after LLZO synthesis indicates a substantial Li loss. Li evaporation during heating leads to Li-deficient LLZO, which decomposes into the La_2O_3 secondary phase, according to Equation 2.7.

Li_2ZrO_3 is a non-volatile secondary product that might appear during LLZO synthesis if the Li content is too high. The excess Li added as compensation for Li loss can suppress the formation of $La_2Zr_2O_7$. However, a very high Li content might introduce a Li_2ZrO_3 secondary phase. Equation 2.8 shows the reaction between Li_2CO_3 and ZrO_2 that results in Li_2ZrO_3 [26].

$$Li_2CO_3 + ZrO_2 \rightarrow Li_2ZrO_3 + CO_2\,(g) \tag{2.8}$$

The phase diagram for the ZrO_2-Li_2O system in Figure 2.5 shows the Li_2ZrO_3 stable phase. Other phases, like $Li_6Zr_2O_7$ and Li_8ZrO_6, are also present in the phase diagram. Although these phases are not frequently found in literature, they may appear if the Li excess is high. The system also has a low-melting eutectic point at 1055 °C.

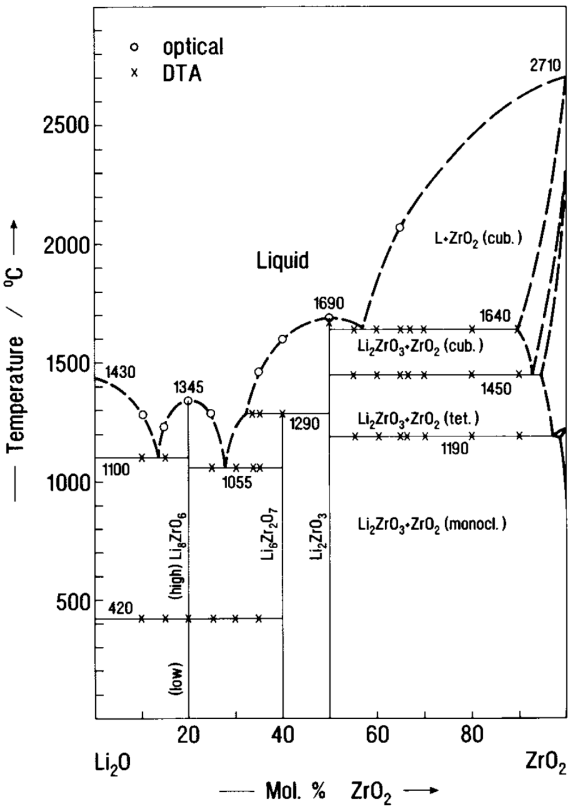

Figure 2.5: Phase diagram of the ZrO_2-Li_2O system. Reprinted from [42].

2.3.2 LLZO + Ta

When Ta is present as dopant in the LLZO system, additional secondary phases can form. Figure 2.6 shows the ternary phase diagram of the La_2O_3-Li_2O-Ta_2O_5 system, and it reveals several possible secondary phases. As seen in the phase diagram, Ta_2O_5 can react with Li_2O or La_2O_3 to form lithium tantalates (Li_3TaO_4, $LiTaO_3$ and $LiTa_3O_8$) or lanthanum tantalates (La_3TaO_7, $LaTaO_4$, $LaTa_3O_9$ and $La_2Ta_{12}O_{33}$), respectively. The existence of these oxide intermediates is not well established in literature. However, it has been reported that Li_3TaO_4 and La_3TaO_7 may segregate at grain boundaries in Ta-doped LLZO [43]. Even though there are few mentions of the other intermediate oxides in literature, they could potentially form in the system.

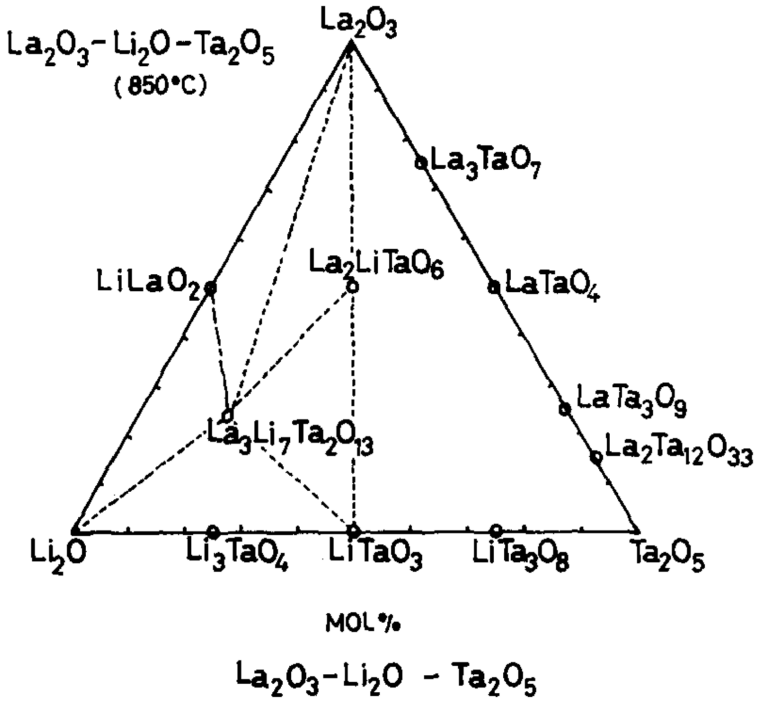

Figure 2.6: Ternary phase diagram of the La_2O_3-Li_2O-Ta_2O_5 system at 850 °C. Reprinted from [44].

2.3.3 Volatile lithium compounds

The volatility of Li at high temperatures has been established from various experiments in literature. The loss of Li can be explained by evaporation of volatile lithium compounds (VLCs), Li loss to secondary phases, and reactions with Al_2O_3 crucibles [11, 29].

Huang *et al.* [11] carried out a study on VLCs in the Ta-LLZO system where they proved the existence of VLCs and investigated their influence on the microstructure of sintered samples. For sintering in ambient conditions, the VLCs consist mainly of Li_2O gas, which is highly reactive to Al_2O_3. Thus, an Al_2O_3 sheet was used to capture the VLCs coming from the bed powder during sintering. The experiment was carried out at 1250 °C, and the bed powder used in the study was not in direct contact with the Ta-LLZO sample. The Al_2O_3 sheet was separated from the bed powder to avoid direct reactions. This way, the Al_2O_3 sheet would only react with the VLCs. The amount of bed powder provided the VLC concentration (Li_2O (g) atmosphere). During sintering, Li_2O gas evaporated from the bed powder and reacted with Al_2O_3 when captured by the sheet. Two new phases were formed, namely $LiAlO_2$ and $LiAl_5O_8$, according to Equation 2.9 and Equation 2.10, respectively. These phases can be found in the phase diagram of the Li_2O-Al_2O_3 system, shown in Figure F.1 in Appendix F. Since the Al_2O_3 sheet did not touch the bed powder, the formation of the new phases proves that the VLC gas exists in the Ta-LLZO system at high temperatures.

$$Li_2O\ (g) + Al_2O_3 \rightarrow 2LiAlO_2 \tag{2.9}$$

$$Li_2O\ (g) + 5Al_2O_3 \rightarrow 2LiAl_5O_8 \tag{2.10}$$

The VLC concentration substantially impacts the sintering and the resulting microstructure of sintered samples. If the concentration of VLCs is low, a longer sintering duration can result in uniform grain growth, where the grains are well sintered with transgranular fracture at fractured surfaces. A high VLC concentration can give a higher relative density and ionic conductivity but may lead to abnormal grain growth (AGG) at longer

sintering times. AGG causes low mechanical strength and is not desired in solid-state electrolytes [11, 45].

In addition to the concentration and evaporation of VLCs, the crucible material may influence the Li loss during sintering. Crucibles made of Al_2O_3 are highly reactive with Li, and the Al_2O_3 can extract Li from the LLZO samples upon direct contact. Using a bed powder to separate the sample from the crucible will prevent unwanted reactions. The bed powder will also supply extra Li, thereby increasing the VLC concentration in the atmosphere during sintering [11, 15]. Inert crucibles, like MgO or Pt crucibles, may be used if sintering is to be performed without bed powder. Sintering in Al_2O_3 crucibles with bed powder can still have higher Li loss compared to inert crucibles due to the reduction in VLC concentration caused by reactions between Al_2O_3 and VLCs [11].

2.4 Sintering of Ta-doped LLZO

Sintering is a thermal process where particles in a powder compact are densified into a solid mass by applying heat without melting the material. Two processes occur during solid-state sintering of ceramic samples: coarsening and densification. Densification is generally more active at high temperatures while coarsening is active at lower temperatures. The driving force for both processes is the decrease in free energy due to the reduction in surface area [46].

Several transport mechanisms control the two processes. The transport mechanisms that give coarsening are evaporation-condensation, surface diffusion, and volume diffusion from the surface. Evaporation-condensation is a gas-phase mechanism where atoms are transferred from the surface of the particle to the contact region between particles, leading to coarsening. This mechanism requires a sufficiently high vapor pressure, as the macroscopic driving force is the difference in vapor pressure on the curved surfaces. For the surface diffusion mechanism, atoms or ions on the surface of particles move along the surface into the small curvature contact regions, leading to neck formation and not densification. The driving force for surface diffusion is the difference in vacancy concentration at the particle surface. Volume diffusion from the particle surface is diffusion through the lattice, which is also driven by vacancy concentration differences [46].

The transport mechanisms for densification are volume diffusion from grain boundaries and grain boundary diffusion. These processes remove material from the grain boundary regions, leading to densification. During volume diffusion from the grain boundaries, material diffuses from the grain boundary, through the lattice, and to the neck. For the grain boundary diffusion, material diffuses along the grain boundary and not through the lattice. The driving force for both densification mechanisms is the difference in vacancy concentration on the curved surfaces. The addition of dopants can increase the vacancy concentration, thereby improving the driving force for diffusion [46].

The sintering process influences the density, microstructure, grain evolution, and ionic conductivity of the sintered samples. An optimal sintering process is crucial for obtaining high-quality solid-state electrolytes with good ionic conductivity. Ta-doped LLZO samples with high quality should be pure cubic and have high relative density and small grains with strong grain-to-grain bonding [11, 47]. High density and small grains lead to improved mechanical strength and ionic conductivity [48]. Pores and grain boundaries make the LLZO electrolytes vulnerable to moisture from the air and formation of dendrites, which can cause electrochemical instability and mechanical weakness [49]. Therefore, high density and low grain boundary concentration are desirable characteristics for LLZO as electrolytes; thus, densification should be promoted, and coarsening should be reduced [46].

Several strategies for increasing the relative density of Ta-doped LLZO can be found in literature. Allen *et al.* [33] used hot-pressing to prepare Ta-doped LLZO samples with a relative density of 96 %. Hot-pressing is a method where pressure and temperature are applied simultaneously. The pressure accelerates the densification process and allows for a lower sintering temperature. Consequently, the coarsening and grain growth can be significantly reduced. Hot-pressing also provides less porosity. Due to less grain growth and porosity, a higher mechanical strength can be achieved compared to conventional sintering [46]. The main disadvantage with hot-pressing is the complicated and expensive equipment [47]. A simpler approach that does not require extra equipment is the two-step sintering method. Huang *et al.* [48] used this strategy to achieve Ta-doped LLZO with high quality and a relative density of 98 %. The method involved a sintering step at high temperature and short holding time, followed by a sintering step at lower temperature

and longer time. Sintering with two or more holding temperatures generally allows for better control of the microstructure and density.

Sintering of LLZO samples does not come without challenges. A problem that may occur is abnormal grain growth (AGG), in which big grains grow abnormally and "swallow" smaller ones [11, 47, 48]. AGG usually takes place after the normal grain growth during the heating stage [12], and it is often found when the sintering temperature is high or the dwell time is extended. The huge grains that form tend to have loose grain boundaries, resulting in poor mechanical strength [50]. Also, it can reduce the density due to the possibility of pores being trapped inside the large grains. AGG can be prevented by employing a lower sintering temperature and holding time. However, lowering the temperature may restrict the densification process and weaken the sintered material [47]. Therefore, finding a temperature that promotes densification without inducing AGG is crucial.

Various sintering techniques aim to limit AGG. The previously mentioned two-step sintering method has been proven successful for Ga-doped LLZO [50]. When samples are heated to an elevated temperature before cooled down to a lower holding temperature, migration of grain boundaries will be suppressed without limiting grain boundary diffusion, thereby allowing densification to occur without AGG. In principle, hot pressing can also be used to reduce abnormal grain growth since the additional driving forces will reduce the sintering temperature and thereby reduce the rate of the grain growth occurring at the final sintering stage [46]. Additives, like MgO or ZnO, can also be used to control AGG. These types of grain growth inhibitors will distribute on the grain boundaries, thereby restricting grain boundary movement and slowing down grain growth. This way, the pores will stay at the grain boundaries until all pores are eliminated. This method has shown promising results in Ta-doped LLZO [48, 51].

2.5 Li^+ conductivity

In order to obtain Ta-doped LLZO samples with high ionic conductivity, the material should be pure cubic and have a sufficient amount of Li vacancies. As previously stated, the Li-ion conductivity of the cubic phase is orders of magnitude higher than that of the tetragonal. The cubic phase has Li sites with an occupancy of < 1, resulting in

Li vacancies that allow for transport of Li-ions. The activation energy for the Li-ion migration along the conduction pathway is low when the structure is cubic. A further increase in the concentration of Li vacancies is obtained by Ta doping, which contributes to an even higher ionic conductivity. That said, it is clear that both the cubic phase and the addition of dopants are required to achieve high ionic conductivity.

Moreover, it has been demonstrated that the microstructure and density of the samples can influence the ionic conductivity [8, 20]. Generally, a high bulk density and small grain size increase the ionic conductivity. Small grains give rise to a high grain boundary concentration, decreasing the segregation of impurities on the grain boundaries. Since impurities on the grain boundaries can hinder Li^+ transport, the impurity segregation should be minimized. However, the grain boundary diffusion of Li-ions is slower than the bulk diffusion, meaning that a too high grain boundary concentration is unfavorable [8]. Furthermore, one should strive for a dense microstructure, which is consistent with a low grain boundary resistance. When the contact between the grain boundaries is tighter, the Li-ion conductivity is enhanced [15, 48]. This demonstrates the importance of attaining a suitable microstructure that provides high ionic conductivity.

Even though the ionic conductivity of Ta-doped LLZO is lower than that of liquid electrolytes, it can still be sufficient for use in solid-state batteries. Bulk ionic conductivity values ranging from 10^{-4} to 10^{-3} S cm^{-1} at room temperature are generally considered sufficient [8]. As mentioned, the grain boundary ionic conductivity is typically lower than that of the bulk. The total ionic conductivity is the sum of the bulk and grain boundary conductivities. A summary of total ionic conductivity values of Ta-doped LLZO reported in literature is provided in Table 2.1, where both $Li_{6.75}La_3Zr_{1.75}Ta_{0.25}O_{12}$ (Ta=0.25) and $Li_{6.4}La_3Zr_{1.4}Ta_{0.6}O_{12}$ (Ta=0.6) samples are represented. According to the table, it should be possible to achieve ionic conductivity values $> 10^{-4}$ S cm^{-1} for both compositions of Ta-doped LLZO, even for sintering in ambient air.

Table 2.1: Relative density, RD, and total ionic conductivity, σ_t, values of Ta-doped LLZO, reported in literature. All samples sintered in ambient air were covered in bed powder, equivalent to a BP-ratio of 2.

Sintering conditions	**Sample**	**RD [%]**	$\boldsymbol{\sigma_t}$ **[$\cdot 10^{-4}$ S cm^{-1}]**	**Ref.**
Ambient air, 1230 °C, 6 h	Ta=0.25	91.5	2.20	[52]
Ambient air, 1180 °C, 36 h	Ta=0.25	96.7	5.2	[53]
Hot pressing, 40 MPa, 1050 °C, 1 h	Ta=0.25	96.0	8.70	[33]
Ambient air, 1150 °C, 5 h	Ta=0.6	79.0	0.36	[40]
Ambient air, 1200 °C, 2.5 h,	Ta=0.6	92.0	4.13	[40]
Ambient air, 1250 °C, 40 min	Ta=0.6	97.0	5.60	[11]
Ambient air, 1250 °C, 10 h	Ta=0.6	97.0	6.70	[45]
Ambient air, 1180 °C, 5 h	Ta=0.6	95.1	6.92	[48]
Ambient air, 1280 °C, 5 h	Ta=0.6	96.7	7.83	[48]
Ambient air, 1140 °C, 16 h	Ta=0.6	-	10.0	[34]

2.5.1 Electrochemical impedance spectroscopy

Electrochemical impedance spectroscopy (EIS) is an electrochemical measurement method that can be used to determine the ionic conductivity of ceramics. By applying a low amplitude sinusoidal AC voltage over a range of frequencies, the AC response signal from the sample can be measured [54, 55]. The sample impedance is the ratio between the voltage input signal and the current response signal.

Resistance is the capability of a circuit to withstand a flow of electrical current. However, resistance is limited to ideal resistors where (i) Ohms law applies for all currents and voltages, (ii) the frequency is independent of resistance, and (iii) the AC response signal through the resistor is not phase-shifted relative to the applied voltage. These simplifying properties do not apply in the complex reality. Thus, the impedance must be used for LLZO solid-state electrolytes. The concept of impedance is about a circuit's ability to resist a flow of an alternating electrical current. It is dependent on frequency and can be represented as a complex number, as shown in Equation 2.11, where $Z(\omega)$ is the

impedance, ω is the radial frequency, E is the applied voltage at time t, I is the sinusoidal current response, E_0 is the voltage amplitude of the signal, I_0 is the current amplitude, Z_0 is the magnitude, ϕ is the phase shift.

$$Z(\omega) = \frac{E}{I} = \frac{E_0 \exp(i\omega t)}{I_0 \exp(i(\omega t - \phi))} = Z_0 \exp(i\phi) = Z_0 (\cos(\phi) + i \sin(\phi)) \tag{2.11}$$

As seen in Equation 2.11, the impedance consists of a real and an imaginary part. The real part of the impedance is often denoted as Z', while the imaginary part is called Z''. The EIS data can be represented as a Nyquist plot, where Z' is plotted on the x-axis and Z'' on the y-axis. The frequency is not explicitly shown in Nyquist plots. Instead, the plot is separated into two frequency regions, where the high-frequency data are on the left, and the lower frequencies are on the right. One or more semicircles are usually found in Nyquist plots. If several semicircles overlap, only a portion of them will be visible [56].

Both the bulk and the grain boundaries contribute to the total ionic conductivity. A typical representation of the contributions from the bulk and the grain boundaries, together with the equivalent circuit providing the model for the data, is shown in Figure 2.7. The electrode response is also included in the figure. The intersection between the semicircles and the real axis defines the resistance of the different contributions.

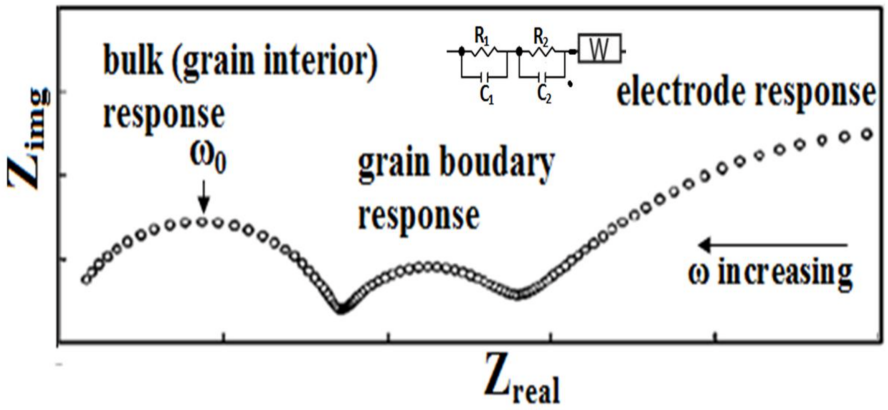

Figure 2.7: Illustration of a Nyquist diagram showing how the bulk response and the grain boundary response can be separated. The equivalent circuit is given in the figure. Reprinted from [56].

3 Experimental

3.1 Chemicals and apparatus

A list of the chemicals utilized in this work is shown in Table 3.1. Table 3.2 gives details about the applied apparatuses. Information about the different crucibles is shown in Table 3.3.

Table 3.1: Information on chemicals

Chemical	**Formula**	**State**	**Purity**	**Manufacturer**
Lithium nitrate	$LiNO_3$	s	99.0 %	RodaChem
Lanthanum nitrate	$La(NO_3)_3{\cdot}6\,H_2O$	s	$\geq$ 99.9 %	Auer-Remy
Zirconyl nitrate	$ZrO(NO_3)_2$	aq	99.9 %	Lehmann&Voss
Tantalum oxalate	Ta_2O_5	aq	$\geq$ 99.9 %	Taniobis
Citric acid	$C_6H_8O_7$	s	-	Weifang Ensign Ind.
Ammonia solution	25 % NH_4OH	aq	-	VWR Chemicals
Ethanol	96 % C_2H_5OH	l	$\geq$ 99.8 %	VWR Chemicals
Isopropanol	$(CH_2)_2CHOH$	l	$\geq$ 99.7 %	VWR Chemicals
Synthetic air	80% N_2, 20% O_2	g	5.0	Linde Group

Table 3.2: Information on apparatuses

Apparatus	**Model**	**Purpose**
Furnace	Nabertherm Muffle Furnace Alkali	Calcination, sintering
Ball mill	US stoneware	Milling
Rotavapor	Buchi R-210	Solvent evaporation
Hydraulic press	Hydraulic C-press	Uniaxial pressing
CIP	Autoclave Engineers CIP	Increase green body density
Dilatometer	Netzsch DIL 402C	Thermal analysis
Archimedes	-	Density measurement
Diffractometer	Bruker D8 A25 DaVinci	Phase identification (XRD)
Polishing machine	Struers LaboPol-21	Grinding and polishing
Polising machine	Struers Tegramin-20	Diamond polishing
SEM	Zeiss Supra 55VP	Microstructure
Carbon coater	Cressington 208 Carbon	Coating of pellets
Sputter coater	Edwards S150B	Au electrode deposition
Potentiostat	Solartron ModuLab XM ECS	Ionic conductivity (EIS)

Table 3.3: Information on crucibles

Material	**Shape**	**Diameter**	**Side length**	**Height**
Al_2O_3	Cylindrical	3.0 cm	-	5.0 cm
MgO	Squared	-	6.5 cm	2.0 cm

3.2 Procedure

The flow chart in Figure 3.1 gives an overview of the experimental procedure.

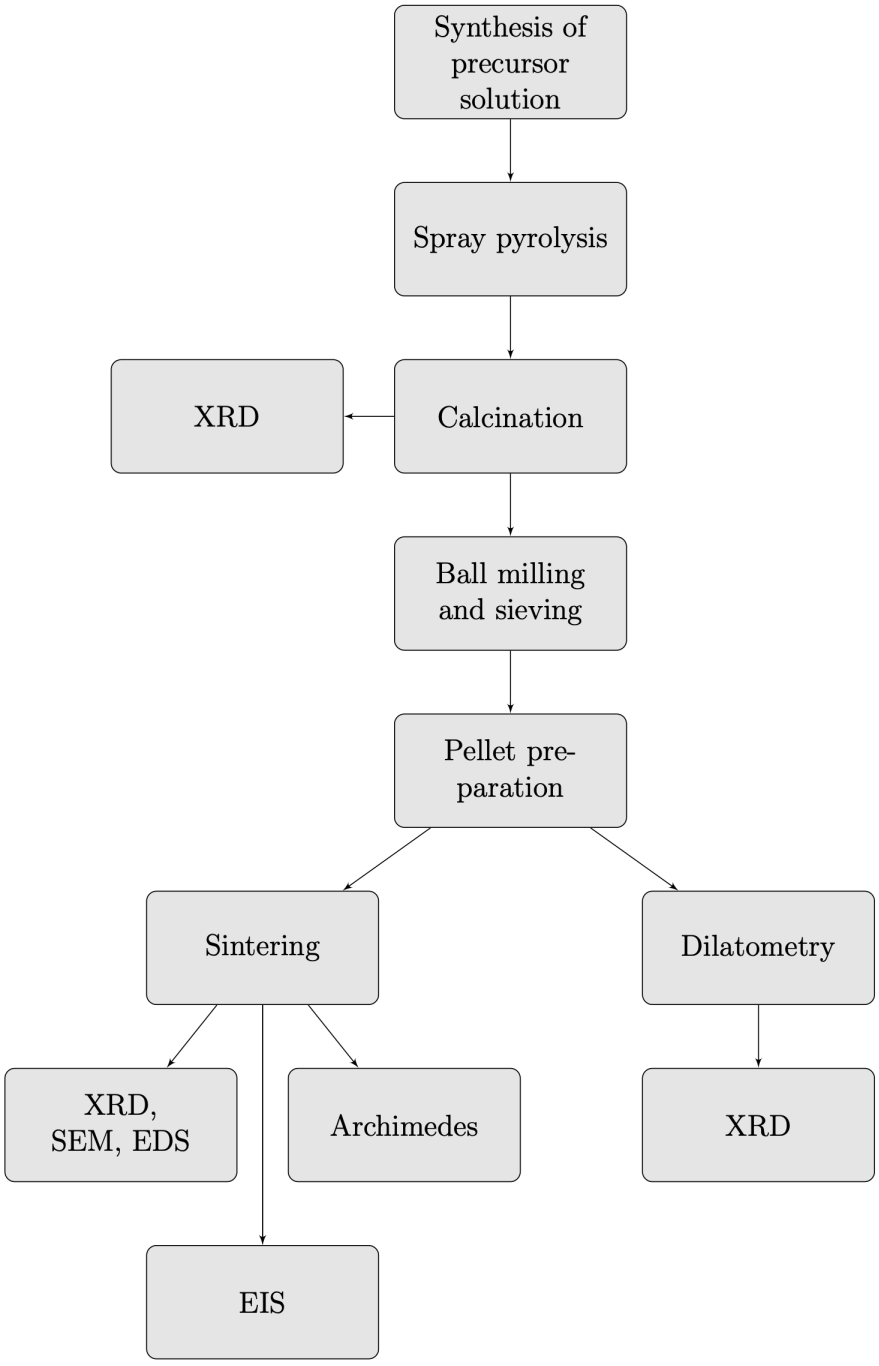

Figure 3.1: Flow chart of the experimental procedure.

3.2.1 Spray pyrolysis

Powders of Ta-doped LLZO were prepared by Cerpotech AS. Solutions were made by mixing water-soluble salts of the individual metals with organic complexing agents. The nitrate-based salts were in molar ratios according to the stoichiometric composition of Ta-doped LLZO, namely $Li_{6.75}La_3Zr_{1.75}Ta_{0.25}O_{12}$ and $Li_{6.4}La_3Zr_{1.4}Ta_{0.6}O_{12}$. In order to compensate for Li loss at high temperatures, an excess of 24.2 mol% Li was added. This provides nominal compositions of $Li_{8.38}La_3Zr_{1.75}Ta_{0.25}O_{12}$ and $Li_{7.95}La_3Zr_{1.4}Ta_{0.6}O_{12}$. Citric acid was used as complexing agent and ammonia was used to adjust the pH. Mixing of the solution proceeded until stabilized. The spray pyrolysis was carried out at 1000 °C, and the setup is illustrated in Figure 3.2. The solid powder compounds will be referred to with their stoichiometric compositions.

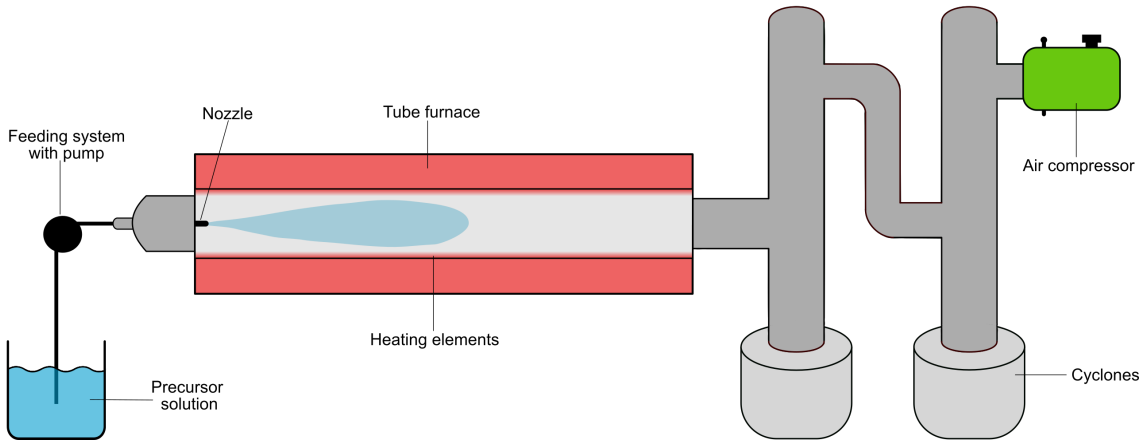

Figure 3.2: Setup of the spray pyrolysis.

3.2.2 Calcination of powder precursor for sintering

The as-received powders from spray were calcined to remove organic residue from the spray pyrolysis process and to form single-phased Ta-doped LLZO. Loose powder was placed in MgO crucibles and calcined in ambient air at 750 °C with a 12 h holding time. Lids were used to prevent contamination, and it was made sure that there was a small opening to allow formed gases to escape from the crucibles. The heating rate and cooling rate were both set to 200 °C/h. The cooling rate was not constant due to lack of active cooling in the furnace. All calcinations were stopped at 200 °C and the crucibles were

removed from the furnace into a desiccator to cool. Cooling in a desiccator prevented the samples from reacting with humidity in the air.

3.2.3 Calcination of bed powder

Powders with composition $Li_{6.75}La_3Zr_{1.75}Ta_{0.25}O_{12}$ were calcined at 800 °C for 12 h in ambient air. The high calcination temperature provided a coarser powder, suitable as bed powder. The calcinations were carried out in MgO crucibles with lids, and the heating and cooling rate were 200 °C/h. The crucibles were removed from the furnace at 200 °C and placed in a desiccator.

3.2.4 Ball milling, evaporation and sieving

After calcination, the powders were ground by wet ball milling to decrease the particle size and remove agglomerates. 250 mL flasks with a diameter of 6 cm were used for the ball milling. The calcined powder was mixed with 100 mL yttria stabilized zirconia (YSZ) balls (d = 5mm) and 75 mL isopropanol solvent. The rotation speed was set to 120 rpm, corresponding to 75 % of the critical milling speed. The milling was left for 24 h. To remove the isopropanol solvent efficiently and gently, a rotavapor was used. After drying, soft agglomerates were gently grounded with a pestle in an agate mortar. A sieve with 250 μm grit was used to obtain the final powders used for sintering.

3.2.5 Pellet preparation

Calcined powders were pressed into green pellets by double-action uniaxial pressing, using a force of approximately 1.5 tons, corresponding to 15 kN. The pressing tools that were used resulted in pellets with 5 mm or 10 mm in diameter. A solution of stearic acid and ethanol was used as lubrication on the pressing tools to ensure easy removal of the pressed pellets. To further increase the green body density, the pellets were pressed by cold isostatic pressing (CIP), where a hydrostatic pressure of 2 kbar was applied to the pellets with a holding time of 1 min.

3.2.6 Dilatometry

Dilatometry was conducted to study the pellet's dimensional change as a function of temperature to investigate the densification behavior during sintering. Pellets with a diameter of 5 mm and a thickness of 6 mm were prepared as described in Section 3.2.5. The mass of the pellets was approximately 350 mg. Figure 3.3 shows a sketch of the dilatometry setup. Platinum foil was used to prevent reactions with the alumina components in the furnace. The analysis was carried out in synthetic air with a flow rate of 30 mL/min. The pellets were heated to 1250 °C with a heating rate of 120 °C/h. The holding time was 1 h and the cooling rate was 120 °C/h.

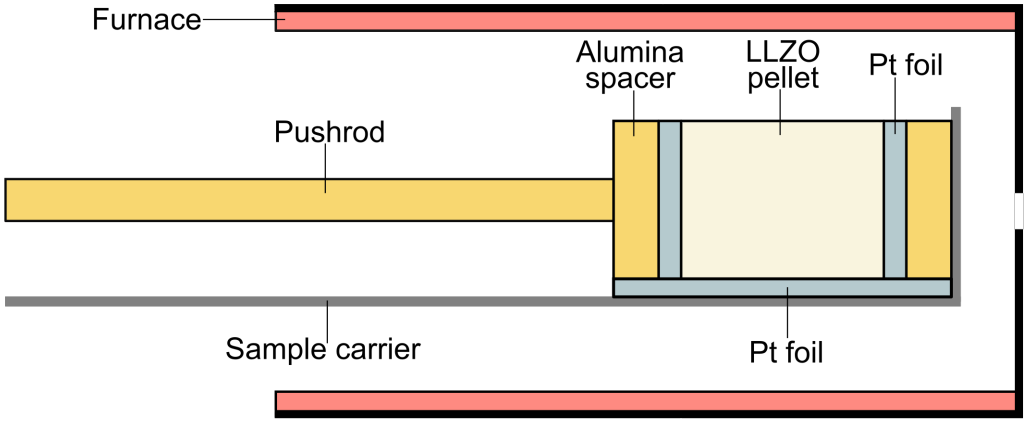

Figure 3.3: Illustration of the dilatometry setup. The opening at the back illustrates the continuous flow of synthetic air. Mer detaljer her.

3.2.7 Sintering

Pellets were prepared as explained in Section 3.2.5. and subsequently sintered with various sintering programs in ambient air to achieve dense samples. Table 3.4 gives an overview of the different sintering programs investigated in this work. All sintering programs had a heating and cooling rate of 200 °C/h. Due to the lack of active cooling in the furnace, the cooling rate was not constant. Lids were placed on top of the crucibles to limit Li loss. Bed powder was used to prevent undesired reactions and provide extra Li as compensation for Li loss. It also acted as a physical separation of the pellet and the

crucible. The bed powder ratio (BP-ratio) is defined as the mass of bed powder per mass of pellet. Two different BP-ratios were used, as shown in Figure 3.4. A BP-ratio of 1 indicates that the bed powder is placed under the pellets during sintering. A BP-ratio of 2 implies that the bed powder is completely covering the pellet. At the end of all sintering programs, the crucibles were removed from the furnace at 200 °C and cooled to room temperature in a desiccator to avoid reactions with humidity in the air. The mass, dimensions, calculated densities and relative densities of green pellets and sintered pellets for the different sintering programs are listed in Appendix A.

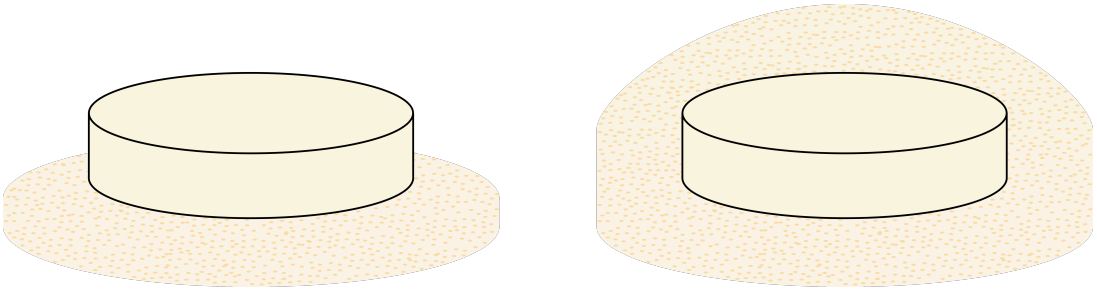

Figure 3.4: Setup for sintering of samples with BP-ratios of 1 (left) and 2 (right).

Table 3.4: Sintering programs used in this work, where T_H is the sintering holding temperature, and t_H is the sintering holding time. BP1 indicates a BP-ratio of 1 and BP2 indicates a BP-ratio of 2.

Sintering program	**T_H [°C]**	**t_H [h]**	**Crucible**	**BP-ratio**
1150@1h/BP1/MgO	1150	1	MgO	1
1150@1h/BP2/Al_2O_3	1150	1	Al_2O_3	2
1150@6h/BP2/Al_2O_3	1150	6	Al_2O_3	2
1150@1h/BP2/MgO	1150	1	MgO	2
1150@6h/BP2/MgO	1150	6	MgO	2

3.2.8 Archimedes' method

The densities of the sintered pellets were measured using the Archimedes' method with isopropanol as the immersion liquid. The pellets were placed in an evaporation dish inside a closed vacuum desiccator. Vacuumed was obtained by using a vacuum pump for about 30 min. This removed air from the pores of the pellets. Next, isopropanol was carefully added through a tube until the pellets were completely submerged. The vacuum pump was on for about 30 min to ensure that isopropanol had penetrated into all open pores. After introducing air back into the chamber, the evaporation dish was placed on a balance and each pellet were weighted while submerged. The isopropanol temperature was noted for each weighing. Lastly, the pellets were individually removed from the isopropanol, rapidly sponged with a damp tissue, and weighted immediately. The dry mass, submerged mass, wet mass, and isopropanol temperature for each pellet are presented in Table B.1 in Appendix B. The relative densities of the pellets were estimated based on the theoretical densities of 5.251 g/cm^3 and 5.469 g/cm^3 for $Li_{6.75}La_3Zr_{1.75}Ta_{0.25}O_{12}$ and $Li_{6.4}La_3Zr_{1.4}Ta_{0.6}O_{12}$, respectively. The theoretical densities were retrieved from the PDF+ database. The relative density, open porosity and total porosity of the pellets are presented in Table B.2 in Appendix B. All calculations are shown in Appendix B.

3.2.9 X-ray diffraction

X-ray diffraction (XRD) was used to determine the phase composition of as-received powders from spray pyrolysis, calcined powders and sintered pellets at ambient conditions. The XRD analysis was performed by the DaVinci 1 diffractometer with CuKα radiation (λ = 1.5406 Å) in the 2θ range of 15-75° with a step size of 0.0133° and a collection time of 60 min. The collection time was 30 min for the as-received powders from spray pyrolysis. All diffraction patterns were collected with Bragg-Brentano reflection geometry and variable slits.

XRD analysis of the as-received powders from spray pyrolysis was performed by densely packing the powders in the cavity of shallow Kapton holders. Kapton film was applied to cover the powder. The calcined powders were gently grounded with a pestle in an agate

mortar to remove any soft agglomerates. A small amount of powder was suspended in isopropanol and gently mixed with a plastic pipette to make a suspension. The suspension was dripped on a Si-flat holder and left to dry. Then, the Si-flat was placed in a Kapton covered with Kapton film. XRD analysis of the pristine surfaces of sintered pellets was carried out by placing the pellets in deep sample holders. Modelling clay was used as attachment and to level out the pellet with the sample holder edge.

The DIFFRAC.EVA V6 (Bruker AXS) software and the 2021 PDF-4+ database were used for indexing and phase identification of the collected XRD patterns. Table 3.5 presents the PDF-4+ cards used for indexing.

Table 3.5: PDF-4+ card numbers of reference patterns.

Compound	**Formula unit**	**PDF-4+ card number**
Ta-doped c-LLZO	$Li_{6.75}La_3Zr_{1.75}Ta_{0.25}O_{12}$	04-018-9300
Ta-doped c-LLZO	$Li_{6.4}La_3Zr_{1.4}Ta_{0.6}O_{12}$	04-024-7089
Pyrochlore	$La_2Zr_2O_7$	01-070-5602
Lithium carbonate	Li_2CO_3	00-022-1141
Lanthanum oxide	La_2O_3	01-071-5408
Lithium silicate	Li_4SiO_4	00-020-0637

3.2.10 Polishing

The surfaces of sintered pellets were dry polished by hand using SiC paper with European grit sizes ranging from 320 to 4000. This was done to remove the pristine surface layer prior to the X-ray diffraction analysis of the polished surfaces.

3.2.11 Scanning electron microscopy and element analysis

The microstructure of sintered pellets was analyzed by scanning electron microscopy (SEM). Both pristine surfaces, polished surfaces, and pristine fracture surfaces were studied. The samples were carbon coated to eliminate any charge effect. Both secondary and backscattered electrons were used for imaging. All images were captured using 10 kV

accelerating voltage and about 10 mm working distance. A 30 μm aperture was used for the secondary electron images, while an aperture of 60 μm was used for the backscattered electron images.

3.2.12 Electrochemical impedance spectroscopy

The ionic conductivity of selected LLZO samples was determined by electrochemical impedance spectroscopy (EIS) using a Solartron ModuLab XM ECS potentiostat. Both sides of the sintered samples were wet polished using isopropanol and SiC paper with European grit sizes ranging from 800 to 4000. The top and bottom surfaces of the pellets were made electrically conductive by sputter coating with Au. The Au layers function as Li^+ blocking electrodes. Figure 3.5 illustrates the setup with approximate dimensions. The thickness of the pellets varied and is therefore not indicated in the figure. The exact dimensions are given in Table E.1 in Appendix E. The EIS measurements were carried out with a two-electrode setup in the frequency range of 1 MHz to 0.1 Hz. The sinusoidal voltage amplitude was 10 mV and the temperature was 20 °C.

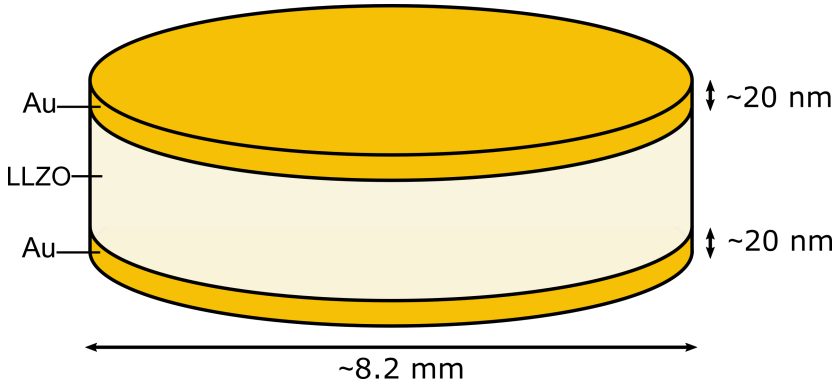

Figure 3.5: Setup for the EIS measurements. The pellet thickness varied and is therefore not given.

The data were plotted as Nyquist plots, and the EC-lab ZFit (BioLogic) software was used to fit the impedance data with an equivalent circuit. Figure 3.6 shows two different equivalent circuits. The equivalent circuit in Figure 3.6a provides a model with the total response (bulk + grain boundary) as one resistance, R_1, in parallel with a constant phase element, CPE_1. The last CPE belongs to the Au electrodes. In the equivalent circuit

in Figure 3.6b, the contributions from the bulk and the grain boundaries are considered independently. Also here, the electrodes are represented in the last CPE. All EIS data obtained in this work were fitted with the equivalent circuit in Figure 3.6b.

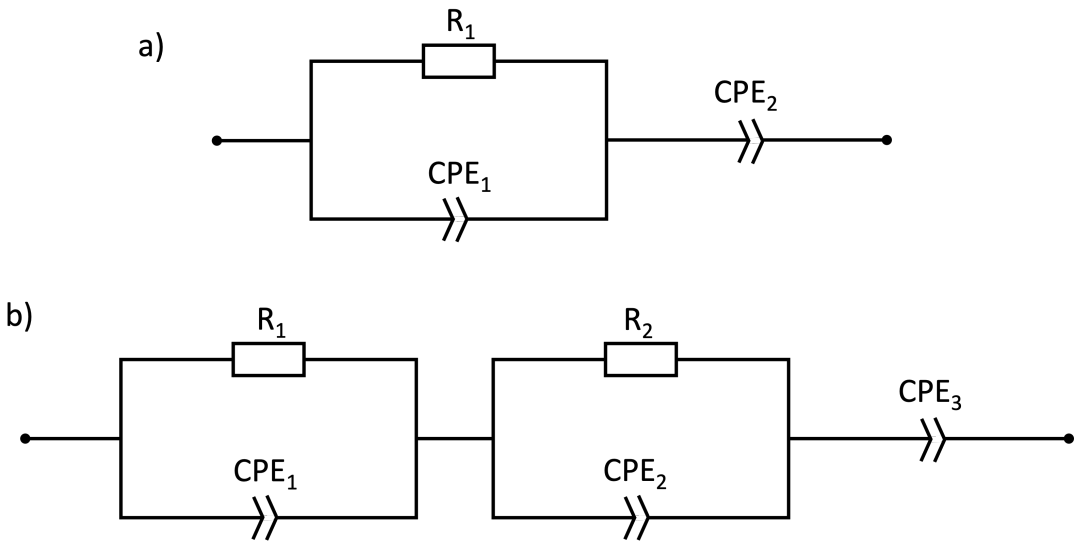

Figure 3.6: The equivalent circuits used to fit the results from the EIS. The circuit in (a) considers the bulk and grain boundary responses as one, while the circuit in (b) consider them separately. constant phase element in both circuits belongs to the Au electrodes. R is a resistor and CPE is a constant phase element.

4 Results

This section exhibits the most important results on sintering properties and Li-ion conductivity of Ta-doped LLZO. The densification behavior during sintering, relative densities, X-ray diffraction patterns describing the phase composition, and SEM micrographs highlighting the microstructure will be covered. In addition, EIS measurements that provide the ionic conductivity of sintered samples will be presented.

4.1 Calcination

Figure C.1 in Appendix C shows the phase composition of the as-received powders from spray pyrolysis. The powders consist of $La_2Zr_2O_7$ and Li_2CO_3, in addition to small amounts of Ta-doped LLZO.

Figure 4.1 presents the X-ray diffraction patterns of $Li_{6.4}La_3Zr_{1.4}Ta_{0.6}O_{12}$ powder batches calcined at 750 °C for 6 h in Al_2O_3 crucibles. The batches have different masses, which are given in the figure. The diffraction patterns of 0.2 g and 5 g were previously measured in the specialization project by Herskedal [13], whereas the diffraction pattern of the 1 g powder batch was measured in this work. The diffractograms are representative for the $Li_{6.75}La_3Zr_{1.75}Ta_{0.25}O_{12}$ samples as well. The results show that the 0.2 g powder consists of pure cubic Ta-doped LLZO, while the two other batches contain $La_2Zr_2O_7$ and Li_2CO_3 in addition to the cubic phase. The relative peak intensities indicate the relative amounts of the associated phases. Due to the low scattering factor of Li-containing compounds, the intensity of the Li_2CO_3 peaks is quite low. This means that the amount of Li_2CO_3 is higher than it appears from the diffraction patterns.

Figure 4.2 shows the X-ray diffraction patterns of $Li_{6.75}La_3Zr_{1.75}Ta_{0.25}O_{12}$ and $Li_{6.4}La_3Zr_{1.4}Ta_{0.6}O_{12}$ powders calcined at 750 °C for 12 h in MgO crucibles. Each powder batch had a mass of approximately 4 g before calcination. All diffraction peaks belong to the cubic phase of Ta-doped LLZO. The calcined powders were used as precursors for the dilatometry analysis and the sintering experiments.

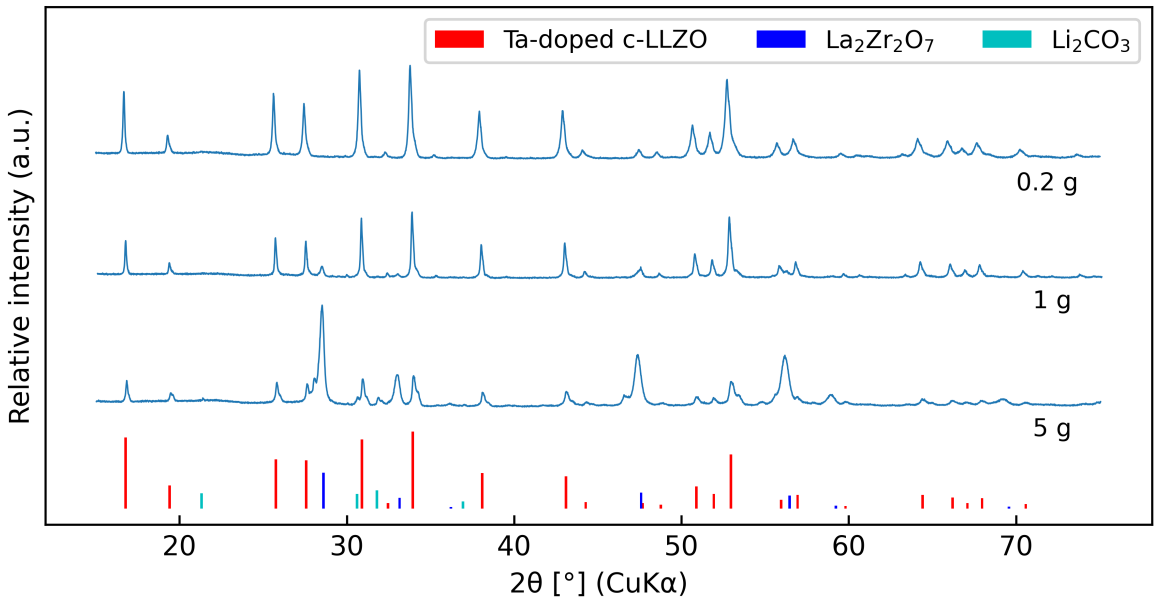

Figure 4.1: X-ray diffraction patterns of 0.2 g, 1 g and 5 g of $Li_{6.4}La_3Zr_{1.4}Ta_{0.6}O_{12}$ powders calcined at 750 °C for 6 h in Al_2O_3 crucibles. The diffraction patterns of 0.2 g and 5 g were previously measured by Herskedal [13].

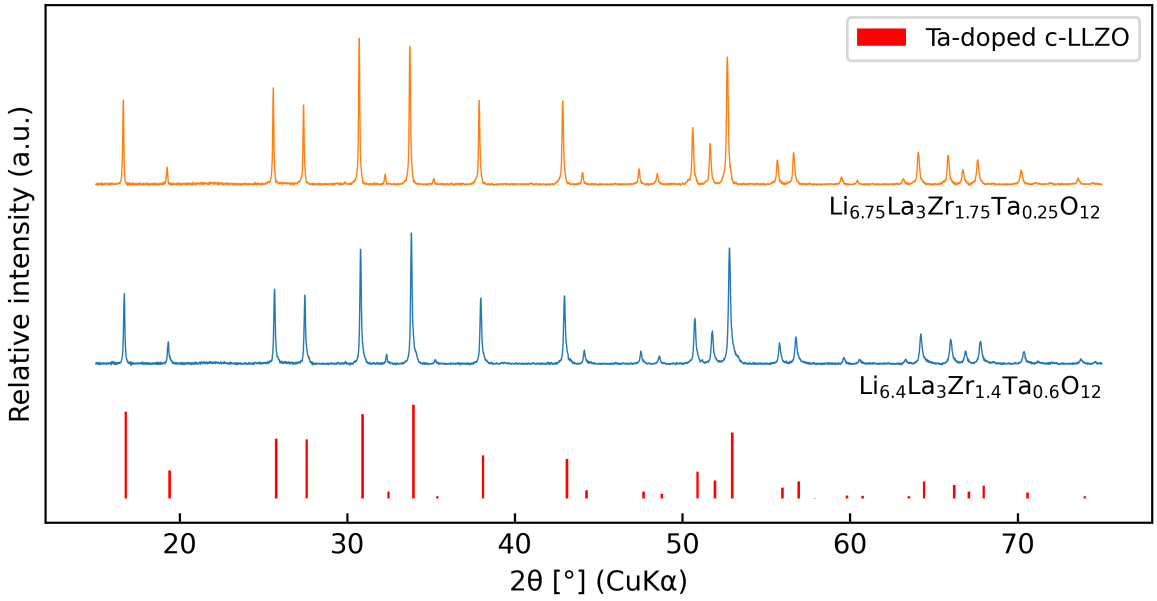

Figure 4.2: X-ray diffraction patterns of powders calcined at 750 °C for 12 h in MgO crucibles. The batch size was approximately 4 g. All peaks are indexed to cubic Ta-doped LLZO.

4.2 Dilatometry

Dilatometry analysis was performed to study the sintering behavior of Ta-doped LLZO pellets. The results are displayed in Figure 4.3, where the relative change in pellet length is plotted as a function of temperature, followed by the isothermal step at 1250 °C. The analysis was carried out with a continuous flow of synthetic air. As can be seen from the figure, the highest rate of densification occurs at approximately 1100 °C. Both curves are equally steep, but the $Li_{6.75}La_3Zr_{1.75}Ta_{0.25}O_{12}$ sample undergoes a more significant reduction in length. Based on the dilatometry analysis, a temperature of approximately 50 °C above the highest densification rate was considered to be an appropriate temperature for the subsequent sinterings.

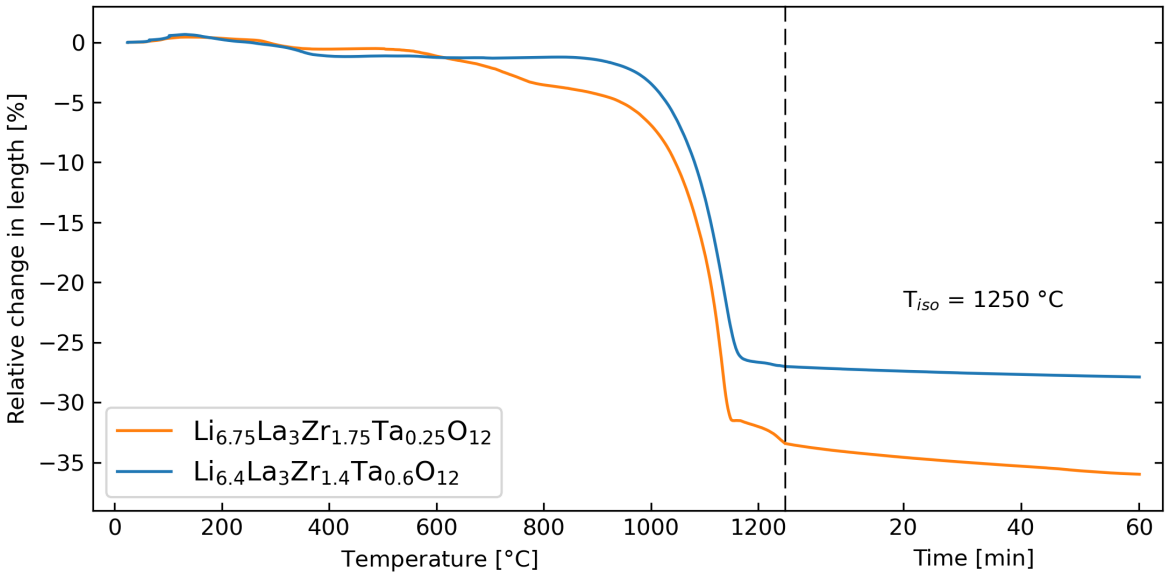

Figure 4.3: Dilatometry analysis carried out with a continuous flow of synthetic air. Pellets were heated to 1250 °C and held for 1 h before cooled down.

Figure 4.4 shows bulk representative X-ray diffraction patters of the pellets after dilatometry. The peaks are indexed to cubic Ta-doped LLZO and $La_2Zr_2O_7$. From the relative peak intensities, it is apparent that the $Li_{6.75}La_3Zr_{1.75}Ta_{0.25}O_{12}$ pellet contains more $La_2Zr_2O_7$ than the $Li_{6.4}La_3Zr_{1.4}Ta_{0.6}O_{12}$ pellet.

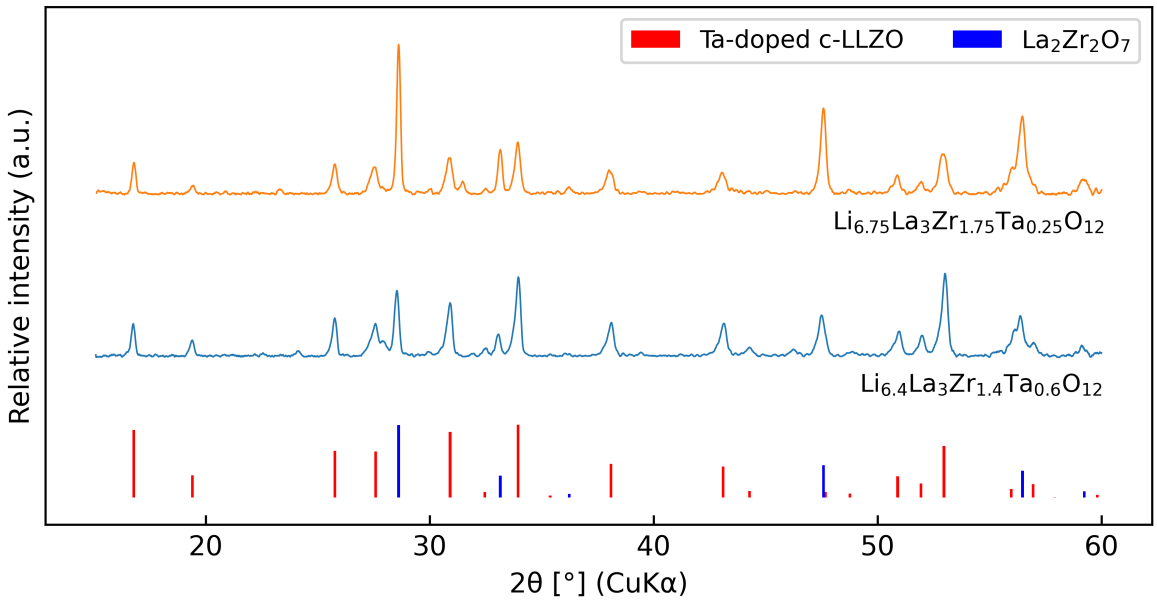

Figure 4.4: Bulk representative X-ray diffraction patters of pellets after the dilatometry analysis. The peaks belong to cubic Ta-doped LLZO and $La_2Zr_2O_7$.

4.3 Sintering

A preliminary sintering experiment was performed with a BP-ratio of 1. The sintering was carried out in a MgO crucible at 1150 °C with a holding time of 1 h. Figure C.4 in Appendix C shows the resulting X-ray diffraction patterns of the sintered samples. It can be seen that a substantial amount of $La_2Zr_2O_7$ is present in both samples. The Li loss was too severe, and thus, a larger amount of bed powder was considered necessary. All following sintering experiments are therefore carried out with a BP-ratio of 2. The first main sintering experiments were performed using Al_2O_3 crucibles. Due to the undefined amount of Li present in the crucibles, combined with the possible Al contamination of the samples, the final sintering experiments were carried out in MgO crucibles.

The mass, dimensions, calculated densities and relative densities of green pellets and sintered pellets for the various sintering programs are given in Tables A.1 to A.5 in Appendix A.

4.3.1 Sintering in Al_2O_3 crucibles

Figure 4.5 shows the bulk representative X-ray diffraction patterns of pellets sintered at 1150 °C in Al_2O_3 crucibles with holding times of 1 h and 6 h, and a BP-ratio of 2. The $Li_{6.75}La_3Zr_{1.75}Ta_{0.25}O_{12}$ samples consist of a mixture of tetragonal and cubic Ta-doped LLZO, as evidenced by the peak splitting, while the $Li_{6.4}La_3Zr_{1.4}Ta_{0.6}O_{12}$ samples are composed of the cubic phase. All samples contain varying amounts of $La_2Zr_2O_7$. According to the peak intensities, the samples sintered for 1 h contain more $La_2Zr_2O_7$ than those sintered for 6 h. The backscattered electron micrographs in Figure 4.6 show the presence of $La_2Zr_2O_7$ on the polished pellet surface of $Li_{6.75}La_3Zr_{1.75}Ta_{0.25}O_{12}$, where the white spots represent the $La_2Zr_2O_7$ phase and the gray parts are Ta-doped LLZO. Figure 4.7 shows that the highest concentration of $La_2Zr_2O_7$ is in the middle of the pellet. It may seem like the high-concentration part is shifted towards the top surface. However, the top surface was polished before being imaged, which means that the $La_2Zr_2O_7$ is in fact located in the middle of the pellet.

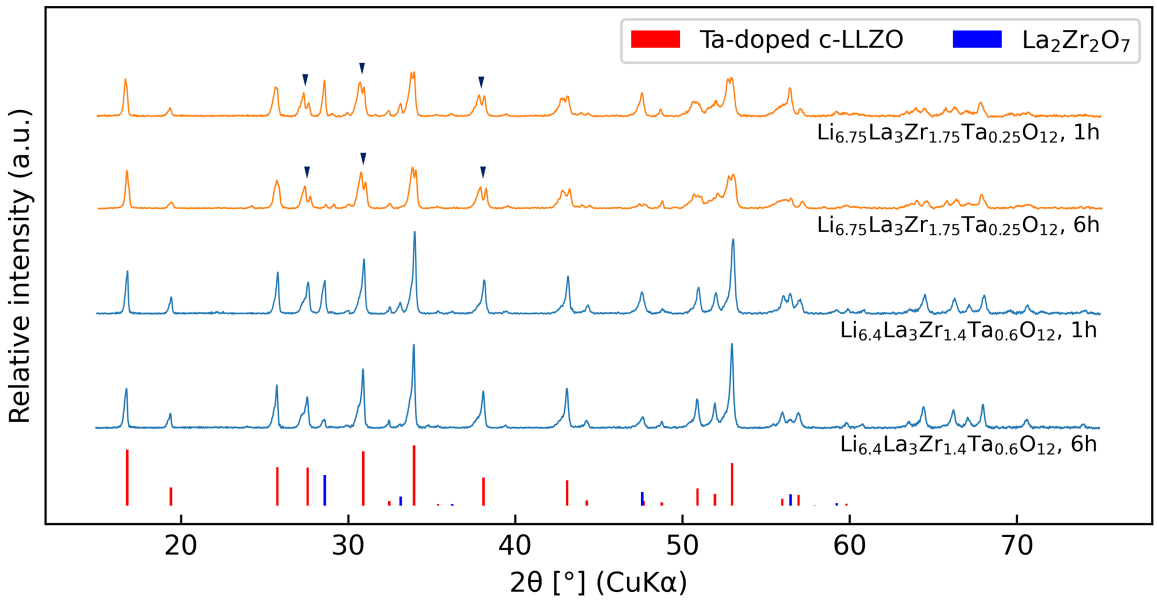

Figure 4.5: Bulk representative X-ray diffraction patterns of samples sintered at 1150 °C in Al_2O_3 crucibles with a BP-ratio of 2. The holding times are 1 h and 6 h. The peaks are indexed to cubic or tetragonal Ta-doped LLZO, and $La_2Zr_2O_7$. The arrows indicate peak splitting.

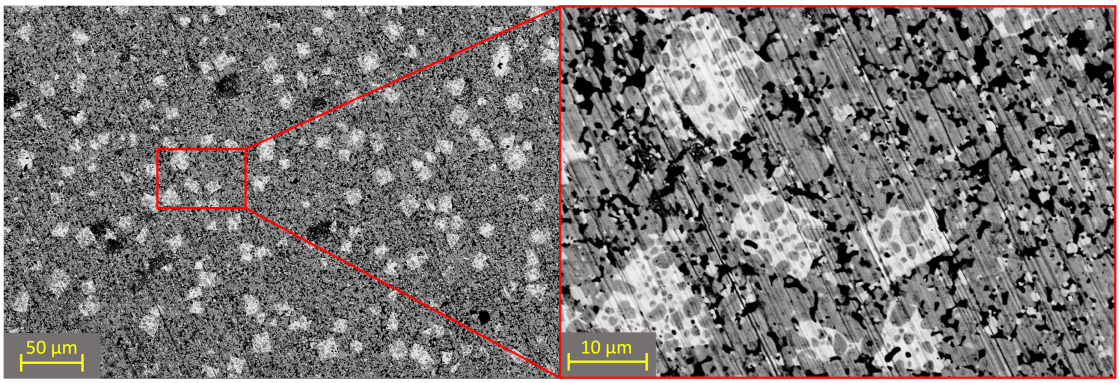

(a) 1150@1h/BP2/Al_2O_3, low mag (b) 1150@1h/BP2/Al_2O_3, high mag

Figure 4.6: Backscattered electron micrographs highlighting $La_2Zr_2O_7$ (white) on the polished surface of a $Li_{6.75}La_3Zr_{1.75}Ta_{0.25}O_{12}$ sample sintered in Al_2O_3 crucibles.

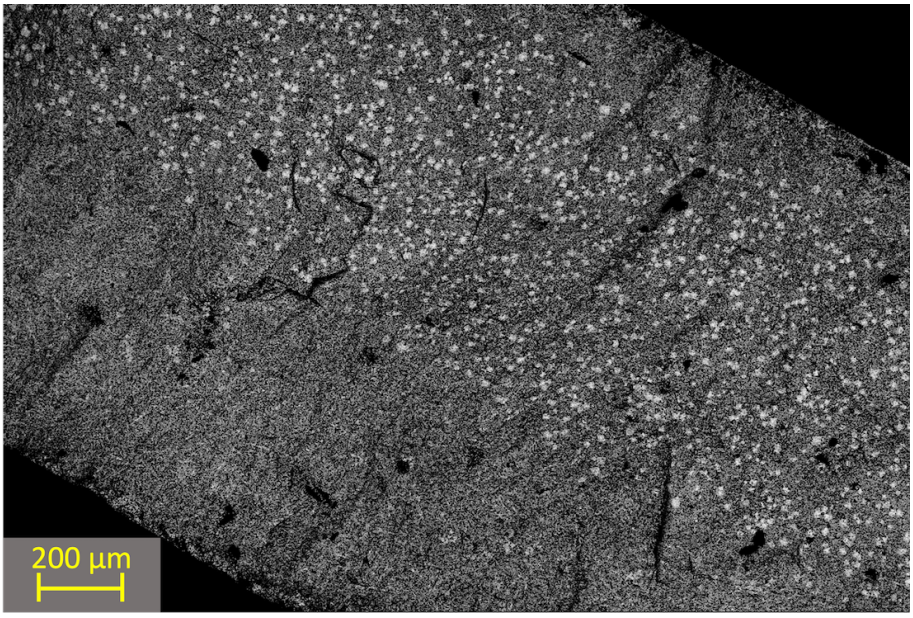

Figure 4.7: Backscattered electron micrograph of the fracture surface of $Li_{6.75}La_3Zr_{1.75}Ta_{0.25}O_{12}$ pellet sintered at 1150 °C for 1 h in Al_2O_3 crucibles with BP-ratio 2. The white spots represent $La_2Zr_2O_7$.

The relative densities measured by Archimedes' method are presented in Figure 4.8. The theoretical densities used to find the relative densities are 5.251 g/cm^3 and 5.469 g/cm^3 for $Li_{6.75}La_3Zr_{1.75}Ta_{0.25}O_{12}$ and $Li_{6.4}La_3Zr_{1.4}Ta_{0.6}O_{12}$, respectively. The calculations of these values are given in Appendix A. The pellets were sintered at 1150 °C in Al_2O_3 crucibles

with a BP-ratio of 2. The figure distinguishes between the samples sintered for 1 h and 6 h. Two samples of each composition were sintered for 1 h, while only one set was sintered for 6 h. Generally, the $Li_{6.4}La_3Zr_{1.4}Ta_{0.6}O_{12}$ samples have higher relative densities than the $Li_{6.75}La_3Zr_{1.75}Ta_{0.25}O_{12}$ samples. Keep in mind that the variations within the densities are small and that there are uncertainties related to the measurements. Therefore, no direct conclusions should be drawn from these data alone. The calculated relative green densities are given in Table B.2 in Appendix B, and the values range between 53.3 % and 55.0 %. The open porosity and total porosity of the samples are also given in the table, and the calculations are shown in Appendix B.

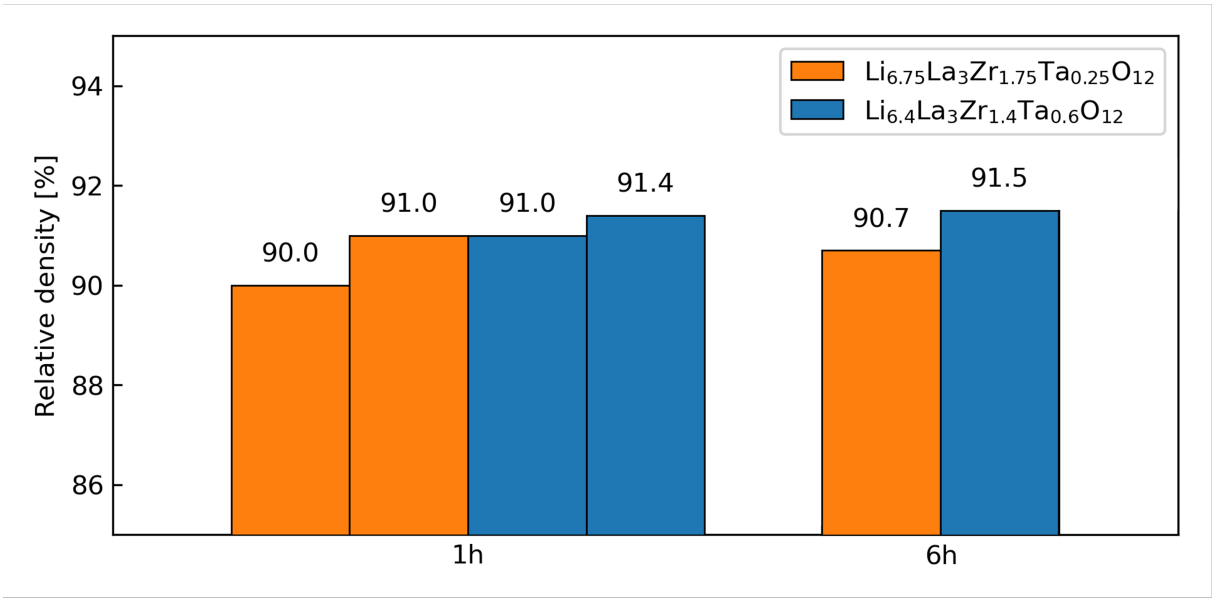

Figure 4.8: Relative density of pellets sintered at 1150 °C in Al_2O_3 crucibles with BP-ratio 2. The holding times are 1 h and 6 h. Measured by Archimedes' method.

The microstructure of the pristine fracture surface of $Li_{6.4}La_3Zr_{1.4}Ta_{0.6}O_{12}$ sintered in an Al_2O_3 crucible is shown in Figure 4.9. There seems to be a bimodal grain size distribution, with large grains (5-10 μm) surrounded by smaller grains (< 1 μm). The remaining samples sintered in Al_2O_3 crucibles have similar microstructures. A more detailed overview of the microstructures are shown in Figure D.1 in Appendix D. The only sample that displayed a significant inconsistency is the $Li_{6.4}La_3Zr_{1.4}Ta_{0.6}O_{12}$ sample sintered for 6 h, where a few large grains were present close to the surface, as shown in Figure 4.10. These large grains were only found near the pellet surface, and not elsewhere.

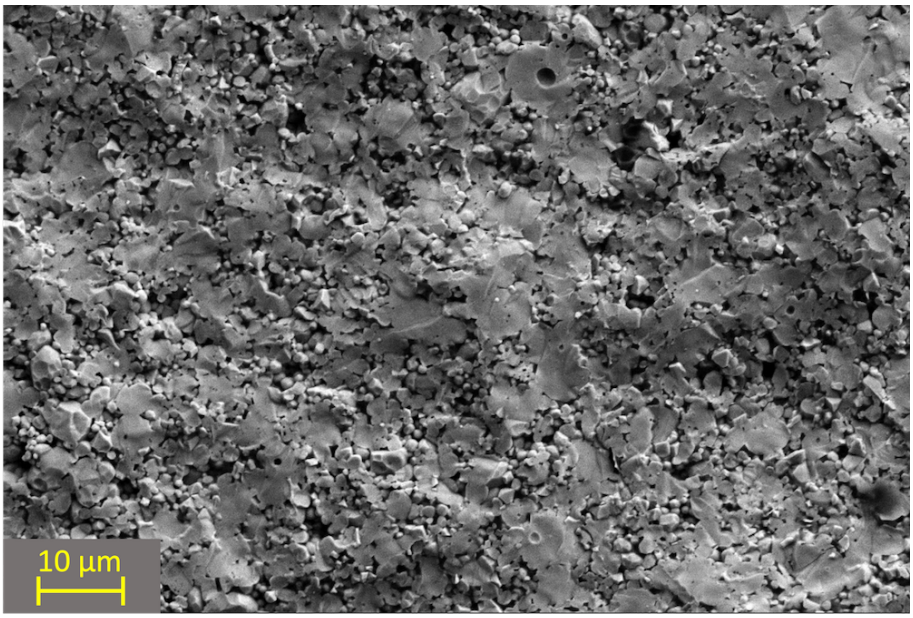

Figure 4.9: Secondary electron micrograph of the pristine fracture surface of $Li_{6.4}La_3Zr_{1.4}Ta_{0.6}O_{12}$ sintered at 1150 °C for 6 h in an Al_2O_3 crucible with BP-ratio 2. The microstructure is representative for all pellets sintered in Al_2O_3 crucibles.

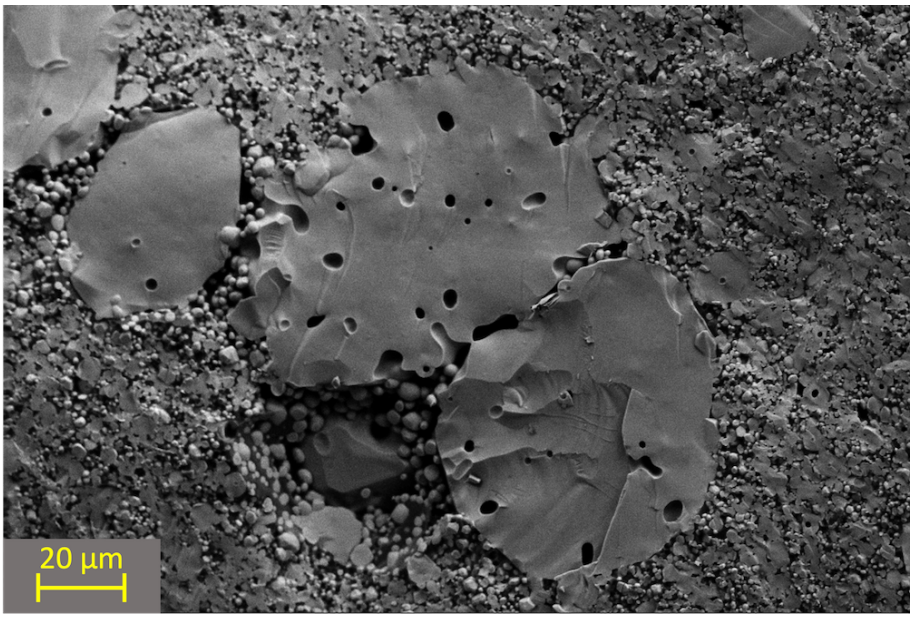

Figure 4.10: Secondary electron micrograph of large grains on the fracture surface of $Li_{6.4}La_3Zr_{1.4}Ta_{0.6}O_{12}$ pellet sintered at 1150 °C for 6 h in Al_2O_3 crucibles with BP-ratio 2.

The Al_2O_3 crucibles used in this work were utilized in the specialization project [13] as well, both for calcinations and sinterings. Therefore, the Al_2O_3 crucibles contained an undefined amount of Li, which makes it impossible to predict the effect of the Li contribution from the crucible. In addition, the crucibles could possibly contaminate the samples with Al. For these reasons, the following sintering experiments were carried out in inert MgO crucibles.

4.3.2 Sintering in MgO crucibles

Figure 4.11 shows the bulk representative X-ray diffraction patterns of pellets sintered at 1150 °C in MgO crucibles with holding times of 1 h and 6 h, and a BP-ratio of 2. A mixture of tetragonal and cubic Ta-doped LLZO is present in the $Li_{6.75}La_3Zr_{1.75}Ta_{0.25}O_{12}$ samples, while the $Li_{6.4}La_3Zr_{1.4}Ta_{0.6}O_{12}$ samples does not contain any tetragonal phase. The $La_2Zr_2O_7$ phase is only found in the samples sintered with a holding time of 1 h. Figure 4.12 demonstrates the presence of the $La_2Zr_2O_7$ phase in samples sintered for 1 h.

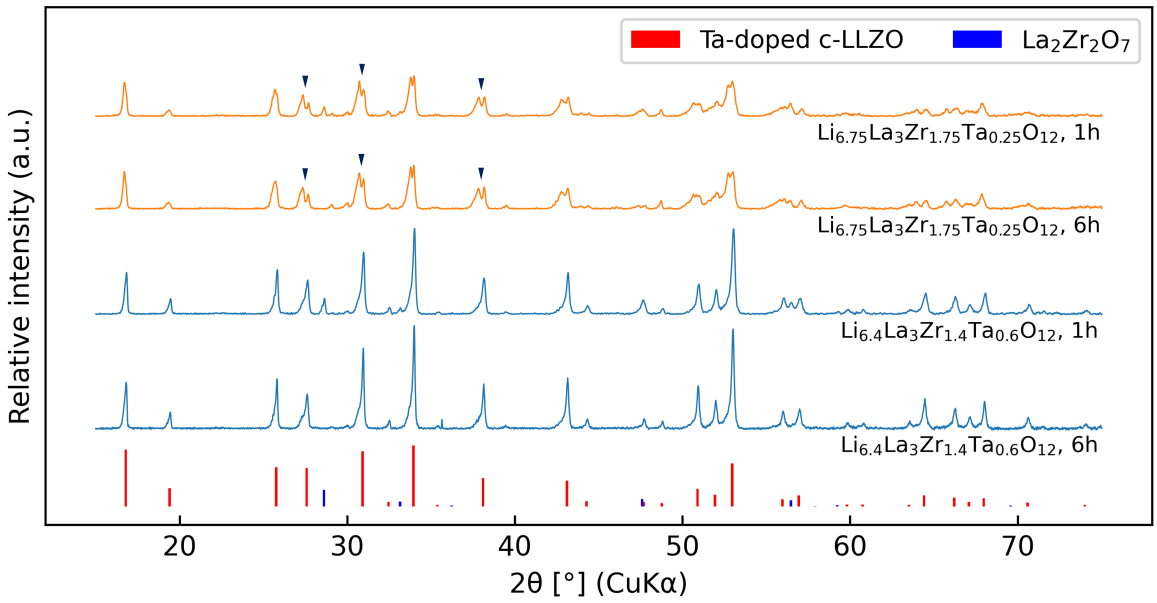

Figure 4.11: Bulk representative X-ray diffraction patterns of samples sintered at 1150 °C in MgO crucibles with a BP-ratio of 2. The holding times are 1 h and 6 h. The peaks are indexed to cubic or tetragonal Ta-doped LLZO, and $La_2Zr_2O_7$. The arrows indicate peak splitting.

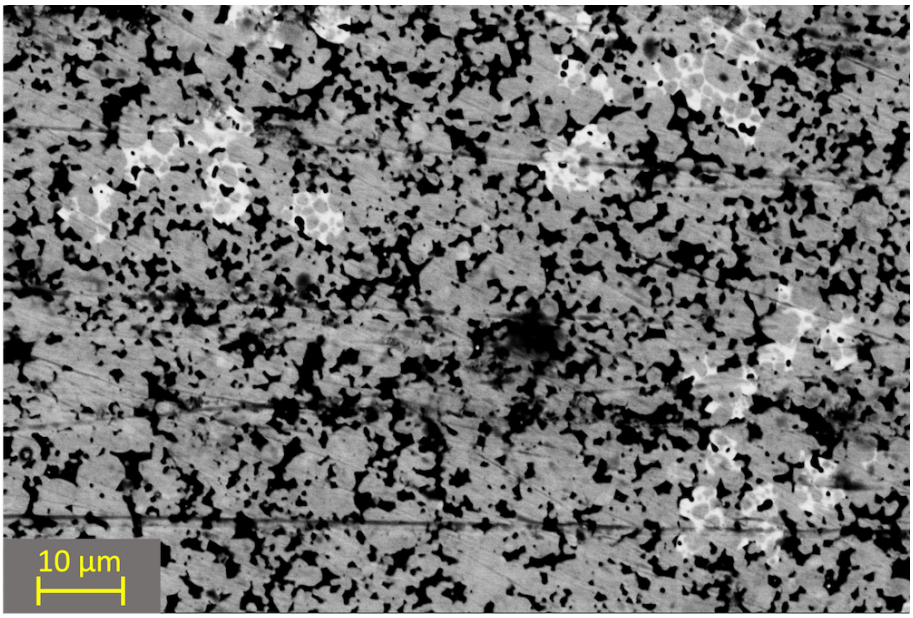

Figure 4.12: Backscattered electron micrograph of the polished surface of the pristine fracture surface of $Li_{6.75}La_3Zr_{1.75}Ta_{0.25}O_{12}$ sintered at 1150 °C for 1 h in an MgO crucible with BP-ratio 2. The white areas represent the $La_2Zr_2O_7$ phase.

Figure 4.13 gives an overview of the relative densities of the samples sintered in MgO crucibles, measured by Archimedes' method. There is a trend of increasing density with increasing holding time. Also, the $Li_{6.4}La_3Zr_{1.4}Ta_{0.6}O_{12}$ pellets are generally denser than the $Li_{6.75}La_3Zr_{1.75}Ta_{0.25}O_{12}$ pellets. Similar to the relative densities of the samples sintered in Al_2O_3 crucibles, there are measurement uncertainties and small variations within the results for the samples sintered in MgO crucibles as well. The calculated relative densities of the green pellets, together with the open porosity and total porosity of the samples, are given in Table B.2 in Appendix B. The values for the relative green density of samples sintered in MgO crucibles with BP-ratio 2 range from 54.1 % to 57.4 %.

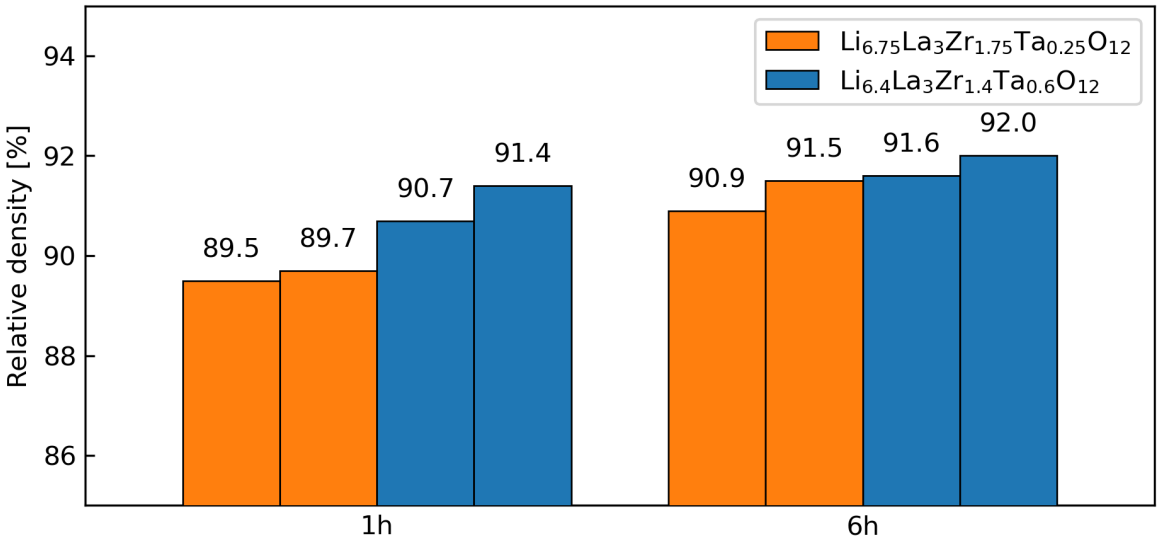

Figure 4.13: Relative density of pellets sintered at 1150 °C in MgO crucibles with a BP-ratio of 2. The holding times are 1 h and 6 h. Measured by Archimedes' method.

Figure 4.14 shows the microstructure of pristine fracture surfaces of pellets sintered in MgO crucibles with holding times of 1 h and 6 h. The mixture of rather large grains surrounded by smaller grains indicates a bimodal grain size distribution. The $Li_{6.75}La_3Zr_{1.75}Ta_{0.25}O_{12}$ samples appear to have a more significant proportion of smaller grains compared to the $Li_{6.4}La_3Zr_{1.4}Ta_{0.6}O_{12}$ samples, which is consistent with the observed difference in density. Furthermore, there is a tendency that transgranular fracture takes place in the large grains, while intergranular fracture is typical for the smaller grains.

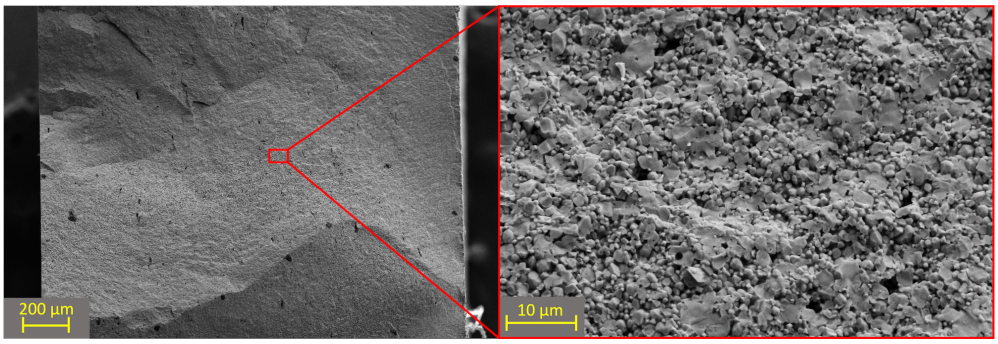

(a) Ta=0.25, 1150@1h/BP2/MgO (b) Ta=0.25, 1150@1h/BP2/MgO

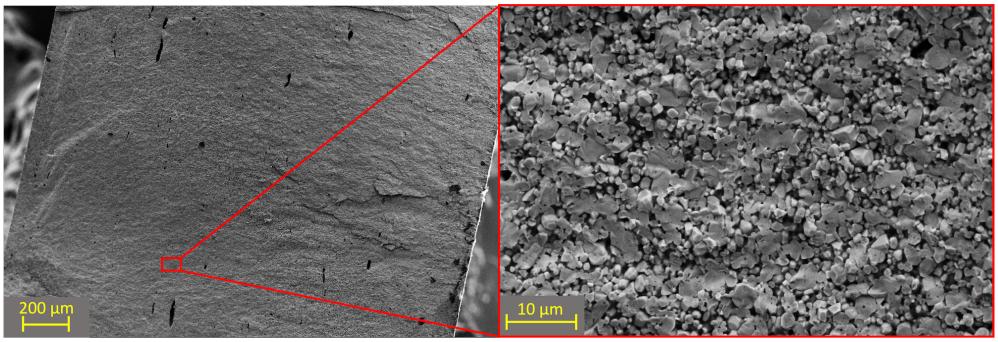

(c) Ta=0.25, 1150@6h/BP2/MgO (d) Ta=0.25, 1150@6h/BP2/MgO

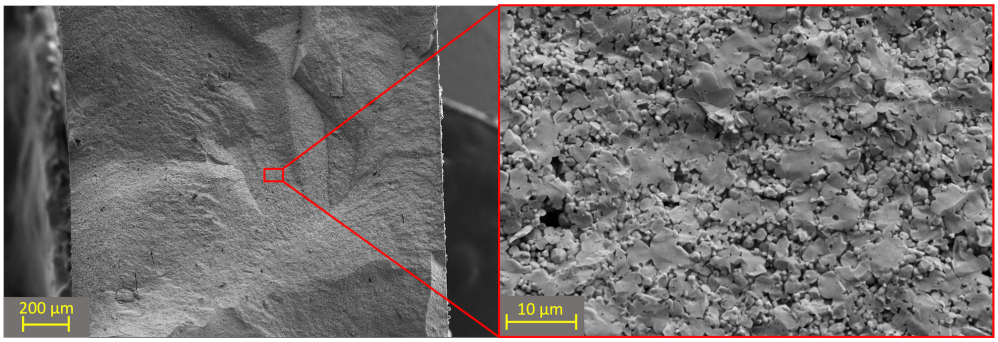

(e) Ta=0.6, 1150@1h/BP2/MgO (f) Ta=0.6, 1150@1h/BP2/MgO

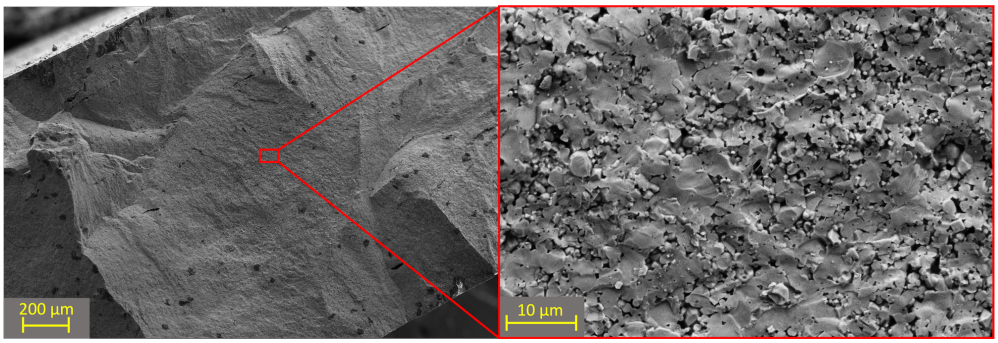

(g) Ta=0.6, 1150@6h/BP2/MgO (h) Ta=0.6, 1150@6h/BP2/MgO

Figure 4.14: Secondary electron micrographs of pristine fracture surfaces of $Li_{6.75}La_3Zr_{1.75}Ta_{0.25}O_{12}$ and $Li_{6.4}La_3Zr_{1.4}Ta_{0.6}O_{12}$ pellets sintered at 1150 °C in MgO crucibles with BP-ratio 2. The holding times are 1 h and 6 h.

4.3.3 Challenges with impurities

X-ray diffraction of the pristine surfaces of sintered pellets revealed the presence of both a La_2O_3 phase and a Li_4SiO_4 impurity phase. The X-ray diffraction patterns in Figure 4.15 show that Li_4SiO_4 is present on the surface of the pellet but not in the bulk. Thus, the presence of this impurity phase is a surface phenomenon that can be removed by polishing. The diffraction patterns represent all pellets and sintering programs in the main sintering study. All X-ray diffractograms of the pellet surfaces, both for sintering in Al_2O_3 and MgO crucibles, are respectively shown in Figure C.5 and Figure C.6 in Appendix C. These figures give more details about each sample and sintering program.

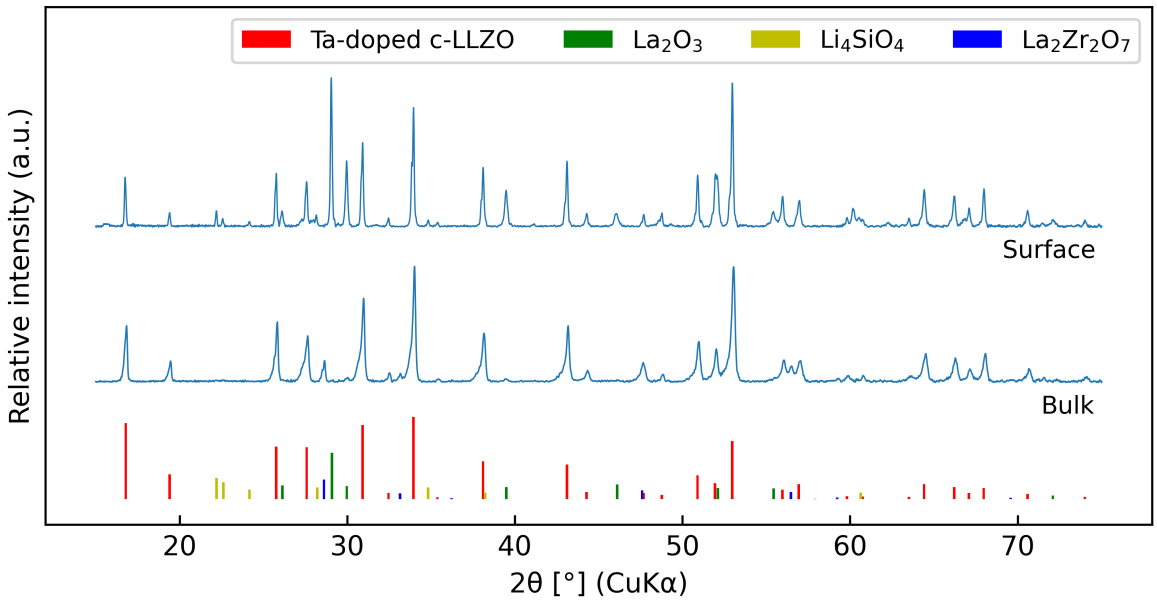

Figure 4.15: X-ray diffraction patterns of the pristine pellet surface and the bulk of $Li_{6.4}La_3Zr_{1.4}Ta_{0.6}O_{12}$ sintered at 1150 °C for 1 h in an MgO crucible with BP-ratio 2. The impurity phase Li_4SiO_4 is present on the surface but not in the bulk.

4.4 Ionic conductivity measurements

EIS measurements were performed to determine the bulk and total Li-ion conductivities of pellets sintered at 1150 °C in MgO crucibles with a BP-ratio of 2. The phase composition of the pellets used for the measurements is shown in Figure 4.11. Figure 4.16 and Figure 4.17 show the resulting Nyquist diagrams, together with the best model fits, of samples sintered for 1 h and for 6 h, respectively. Each curve consists of two overlapping semicircles in the high-frequency region and a tail in the low-frequency region. The two semicircles represent the two contributions to the total ionic conductivity, namely the bulk and the grain boundaries. To determine the best fit parameters, the Nyquist curves were fitted with the equivalent circuit in Figure 3.6b. The resistance values obtained from the fitting, together with the diameter and thickness of the pellets, are listed in Table E.1 in Appendix E. The bulk and total ionic conductivity are given in Table 4.1. The equations used for the calculations are shown in Appendix E. $Li_{6.75}La_3Zr_{1.75}Ta_{0.25}O_{12}$ sintered at 1150 °C for 1 h in a MgO crucible with BP-ratio 2 has the highest bulk ionic conductivity of $4.00 \cdot 10^{-4}$ S cm^{-1}. The highest total ionic conductivity is found for the $Li_{6.4}La_3Zr_{1.4}Ta_{0.6}O_{12}$ sample sintered at 1150 °C for 6 h in a MgO crucible with BP-ratio 2, and it is $1.66 \cdot 10^{-4}$ S cm^{-1}.

Table 4.1: The bulk ionic conductivity, σ_b, and the total Li-ion conductivity, σ_t, of samples sintered in MgO crucibles, measured at 20 °C. The values are calculated from the best fit of the Nyquist diagrams.

Sintering program	**Sample**	$\boldsymbol{\sigma_b}$ **[$\cdot 10^{-4}$ S cm^{-1}]**	$\boldsymbol{\sigma_t}$ **[$\cdot 10^{-4}$ S cm^{-1}]**
1150@1h/BP2/MgO	Ta=0.25	4.00 ± 0.05	1.49 ± 0.03
1150@1h/BP2/MgO	Ta=0.6	2.80 ± 0.05	1.36 ± 0.03
1150@6h/BP2/MgO	Ta=0.25	3.95 ± 0.07	1.17 ± 0.04
1150@6h/BP2/MgO	Ta=0.6	3.70 ± 0.07	1.66 ± 0.04

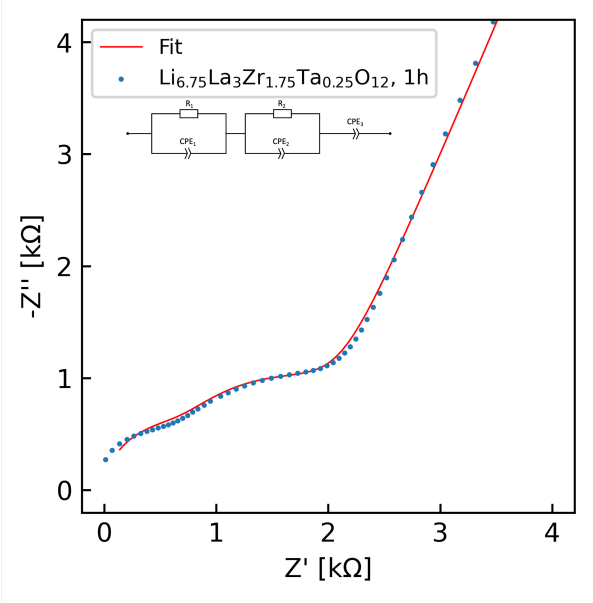

(a) Ta=0.25, 1150@1h/BP2/MgO

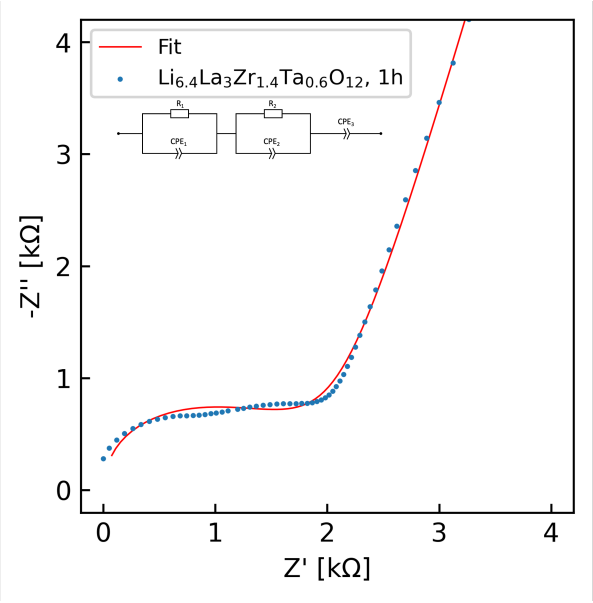

(b) Ta=0.6 1150@1h/BP2/MgO

Figure 4.16: Nyquist diagrams for Ta-doped LLZO samples sintered at 1150 °C for 1 h in MgO crucibles with BP-ratio 2. Z' is the real part and Z" is the imaginary part of the impedance. The best fit of the data is included.

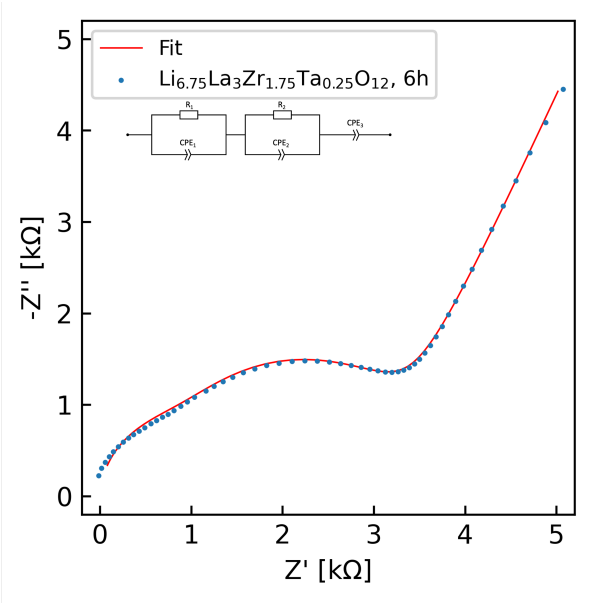

(a) Ta=0.25, 1150@6h/BP2/MgO

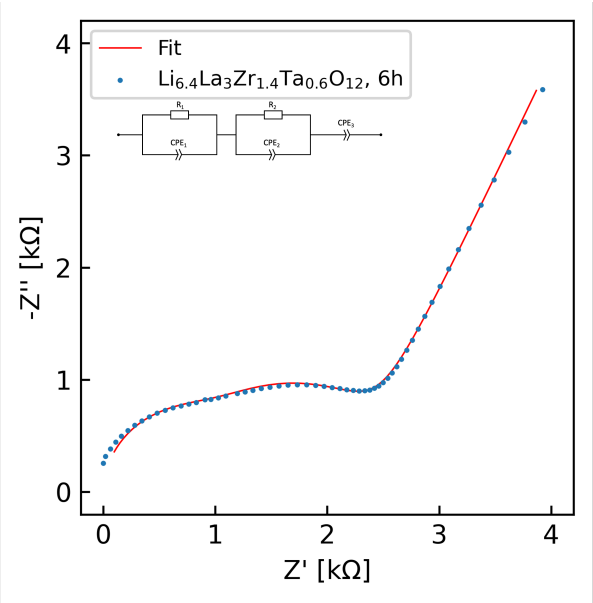

(b) Ta=0.26, 1150@6h/BP2/MgO

Figure 4.17: Nyquist diagrams for Ta-doped LLZO samples sintered at 1150 °C for 6 h in MgO crucibles with BP-ratio 2. Z' is the real part and Z" is the imaginary part of the impedance. The best fit of the data is included.

5 Discussion

5.1 Phase composition

LLZO powders with different Ta content were investigated in this work. Doping with Ta is performed to achieve a high concentration of Li vacancies and thereby obtain a higher ionic conductivity compared to undoped LLZO. Both powders had a Li excess of 24.2 mol% to compensate for Li loss. Achieving a sample with good ionic conductivity requires a high degree of phase purity, high density, and a homogeneous microstructure. Controlling the phase composition is therefore essential. The samples in this work have different Ta content, and thus different Li vacancy concentration, which is expected to influence the phase composition.

5.1.1 Phase composition of calcined powders

The phase composition of as-received powders from spray pyrolysis was previously established by Herskedal [13], and the X-ray diffractogram is shown in Figure C.1 in Section C. It was found to consist of $La_2Zr_2O_7$, Li_2CO_3 and Ta-doped LLZO. Rietveld refinement revealed that approximately 80 % was $La_2Zr_2O_7$ [13]. Upon calcination, $La_2Zr_2O_7$ reacts with La_2O_3 and Li_2O to form LLZO (Equation 2.3). The optimal calcination temperature for Ta-doped LLZO was determined to be 750 °C by Herskedal [13]. It was also noted that the size of the powder batch strongly influences the phase composition of the as-calcined powders. This is exemplified in Figure 4.1, where $Li_{6.4}La_3Zr_{1.4}Ta_{0.6}O_{12}$ powders with different batch sizes were calcined at 750 °C for 6 h. The batch with 5 g of powder contained substantially more $La_2Zr_2O_7$ compared to the others, and it is obvious that larger amounts of powder results in more $La_2Zr_2O_7$ in the as-calcined powders.

The strong dependence on batch size is likely related to the decomposition of Li_2CO_3. During calcination of larger powder batches, the decomposition of Li_2CO_3 into Li_2O and CO_2 (g), as shown in Equation 2.3, creates a CO_2 rich atmosphere in the furnace. Consequently, there will be insufficient transport of CO_2 (g) out of the powder batch, and the high CO_2 (g) partial pressure will slow down the Li_2CO_3 decomposition rate.

Li_2CO_3 needs to decompose into Li_2O to acquire formation of LLZO (Equation 2.4). A short calcination time can give rise to residual $La_2Zr_2O_7$ if not all Li_2CO_3 is able to decompose. Based on this, there is reason to believe that pure cubic Ta-doped LLZO can be achieved by employing a longer holding time when calcining larger batches. In the work by Herskedal [13], 0.2 g was found to be the appropriate amount of powder for a 6 h holding time calcination. In this work, however, batches of at least 4 g were preferred due to the need to produce large quantities of calcined powder. Therefore, a longer holding time was applied to explore the influence on CO_2 transport and Li_2CO_3 decomposition. As seen in Figure 4.2, calcination at 750 °C with a 12 h holding time resulted in cubic Ta-doped LLZO without $La_2Zr_2O_7$. This further supports the hypothesis that a longer duration is needed for all Li_2CO_3 to decompose, and it shows that a calcination time of 12 h is sufficient to get a complete transformation of $La_2Zr_2O_7$ into LLZO.

It is important to mention that Al_2O_3 crucibles were used for the calcinations with 6 h holding times, while MgO crucibles were used for the 12 h holding times. The MgO crucibles were chosen for the calcinations in this work as it was most convenient considering the high production level.

5.1.2 Phase composition of sintered pellets

After sintering in both Al_2O_3 and MgO crucibles, all $Li_{6.75}La_3Zr_{1.75}Ta_{0.25}O_{12}$ pellets contained a mixture of cubic and tetragonal phase, as evidenced by the peak splitting in Figure 4.5 and Figure 4.11. The presence of the tetragonal phase after sintering was not observed for any of the $Li_{6.4}La_3Zr_{1.4}Ta_{0.6}O_{12}$ pellets. $Li_{6.75}La_3Zr_{1.75}Ta_{0.25}O_{12}$ has a lower Ta content and thereby fewer Li vacancies, and the low concentration of Li vacancies can explain the existence of the tetragonal phase. What is surprising is that the $Li_{6.75}La_3Zr_{1.75}Ta_{0.25}O_{12}$ precursor powders were pure cubic before sintering (Figure 4.2). The fact that the tetragonal phase occurred after sintering indicates that Li was supplied to the pellets during sintering, which reduced the vacancy concentration. The Li likely came from the bed powder that was in direct contact with the pellets. This hypothesis is supported by the fact that the $Li_{6.75}La_3Zr_{1.75}Ta_{0.25}O_{12}$ pellets sintered with a BP-ratio of 1 had less peak splitting, as seen in Figure C.4 in Appendix C, compared to the sintering

with a BP-ratio of 2. If the amount of bed powder is higher and the contact surface between the pellet and bed powder is larger, it is likely that more Li is taken up by the pellet, thus leading to more tetragonal phase formed. As stated in Section 2.2.1, the tetragonal phase has lower ionic conductivity than the cubic phase. Hence, presence of the tetragonal phase in the sintered pellets is not beneficial, as it can reduce the final ionic conductivity.

5.2 Secondary phases

5.2.1 $La_2Zr_2O_7$ in pellets after sintering

The X-ray diffraction patterns representing the bulk of samples sintered in Al_2O_3 and MgO crucibles (Figure 4.5 and Figure 4.11) indicate the presence of $La_2Zr_2O_7$ in varying amounts. Detection of the $La_2Zr_2O_7$ secondary phase after sintering at high temperatures is frequently reported in literature. As explained in Section 2.3, it commonly arises from Li deficiency, an issue related to Li loss. As shown in Equation 2.7, LLZO is transformed back to $La_2Zr_2O_7$ when there is a shortage of Li. $La_2Zr_2O_7$ slows down the sintering, which can help limit grain growth. Still, $La_2Zr_2O_7$ is an undesired phase because it reduces the Li-ion conductivity. Section 2.3.1 presented different causes of Li loss. Formation of VLCs during sintering is likely the main contribution to the Li loss observed in this work. Although reactions between the pellets and the crucible material are possible, the separation provided by the bed powder makes it unlikely. The small amounts of Li4SiO4 on the pellet surface may give rise to some Li loss, but only to a small extent. Hence, the major cause is assumed to be evaporation of VLCs at high temperatures.

The Li loss must be considerably reduced to avoid $La_2Zr_2O_7$ formation. The bed powder compensates for some of the lost Li. However, the presence of $La_2Zr_2O_7$ even after sintering with a BP-ratio of 2 indicates a significantly higher Li loss than expected. Addition of an even larger amount of bed powder could suppress more of the Li loss. However, La and Ta are rare and expensive elements that will give high raw-material costs [47]. Using a tetragonal bed powder can possibly contribute to suppressing some Li loss. The tetragonal phase contains more Li in the structure than the cubic phase, which can be

beneficial for reducing the formation of La2Zr2O7 during sintering. In this work, the bed powder was pure cubic, as shown in Figure C.2. An alternative solution is to use a tetragonal Ta-doped LLZO powder as precursor for the sintering. However, this requires a tetragonal-cubic transformation to avoid the presence of the tetragonal phase after sintering, as this will lower the ionic conductivity.

According to Figure 4.5 and Figure 4.11, the general trend is that a holding time of 1 h results in more $La_2Zr_2O_7$ compared to 6 h, regardless of crucible material. The pellets sintered for 6 h in the MgO crucible were the only samples that completely avoided $La_2Zr_2O_7$ in the bulk. This is surprising, as a longer dwell time is expected to increase the Li loss and thereby increase the amount of $La_2Zr_2O_7$ secondary phase. The unpredicted reduction in $La_2Zr_2O_7$ with increasing holding time may suggest that the Li loss decreases as a longer sintering time is approached. However, this is contrary to expectations and not likely. Another hypothesis is that a longer dwell time allows more Li to be transferred from the bed powder and into the pellet. It seems that a fairly long holding time, up to 6 h, is necessary for the amount of Li transferred to be significant. The Li that is supplied to the pellet from the bed powder after 1 h does not seem to affect the $La_2Zr_2O_7$ formation. A holding time closer to 6 h allows more Li to be transferred, which results in less $La_2Zr_2O_7$. This theory seems to be the most plausible explanation for the unexpected observations.

Furthermore, it was discovered that the samples sintered in MgO crucibles generally had less $La_2Zr_2O_7$ present after sintering compared to those sintered in Al_2O_3, based on the relative peak intensities. Micrographs of the polished surface (Figure 4.6) show the presence of $La_2Zr_2O_7$ in pellets sintered in Al_2O_3 crucibles, appearing as spots. The micrograph of the polished surface of a pellet sintered in an MgO crucible (Figure 4.12) confirms that the concentration of $La_2Zr_2O_7$ is substantially lower. This agrees with the phase compositions from the X-ray diffractograms (Figure 4.5 and Figure 4.11) and supports the proposition that sintering in Al_2O_3 crucibles results in more $La_2Zr_2O_7$. A possible explanation for these results may be that the Al_2O_3 crucibles did not contain large amounts of Li after all. It was initially believed that the crucibles had taken up lots of Li during previous calcinations and sinterings. However, this was not possible to verify. If the crucibles actually consumed Li during the sintering in this work, and thus removed

it from the bed powder or pellets, there would be a lower Li content and consequently more $La_2Zr_2O_7$ formation in the pellets sintered in the Al_2O_3 crucibles.

The largest amount of $La_2Zr_2O_7$ was found in the 1 h-sintering in the Al_2O_3 crucible, as seen in Figure 4.5. The micrograph in Figure 4.7 demonstrates that it is mostly located in the middle of the pellet. The X-ray diffraction pattern of the pristine pellet surface in Figure C.5 show no peaks for $La_2Zr_2O_7$, which also indicates the absence of $La_2Zr_2O_7$ at the surface. This applies to the sinterings in MgO crucibles as well (Figure C.6). The bed powder likely supplied extra Li to the surface of the pellet it was in contact with. If the bulk was not provided with Li, the $La_2Zr_2O_7$ formation in the bulk could not be suppressed. The fact that the concentration of $La_2Zr_2O_7$ is high in the middle corroborates this theory.

Overall, the high degree of $La_2Zr_2O_7$ formation during sintering is unexpected since the powders are supposed to contain a Li excess of 24.2 mol%, which was added before the spray pyrolysis. Throughout this work, it has been assumed that the powders contain this surplus of Li. However, there is no assurance that the amount of excess Li corresponds to what was initially added. Li may be lost not only during sintering, but also during spray pyrolysis, calcination, and powder processing. If large amounts of Li are lost in these steps, the Li surplus in the pellets is in fact lower than anticipated from the nominal compositions, which can explain the large amount of $La_2Zr_2O_7$ formed in the pellets. Thus, a Li excess $>$ 24.2 mol% is likely beneficial.

When it comes to the effect of Ta-content, the amount of $La_2Zr_2O_7$ present in the pellets does not seem to be particularly affected. It is expected that the $Li_{6.4}La_3Zr_{1.4}Ta_{0.6}O_{12}$ samples contain more $La_2Zr_2O_7$ than $Li_{6.75}La_3Zr_{1.75}Ta_{0.25}O_{12}$ due to the higher Ta-content providing a higher Li vacancy concentration. An example of this can be seen in Figure 4.11, where the $Li_{6.4}La_3Zr_{1.4}Ta_{0.6}O_{12}$ samples sintered for 1 h contain more $La_2Zr_2O_7$ than the $Li_{6.75}La_3Zr_{1.75}Ta_{0.25}O_{12}$ samples with the same holding time. However, the differences between the two compositions are relatively small.

5.2.2 $La_2Zr_2O_7$ in pellets after dilatometry

A high amount of $La_2Zr_2O_7$ was also found in the pellets after dilatometry (Figure 4.4). Interestingly, there was drastically more $La_2Zr_2O_7$ after the dilatometry analysis compared to the other sinterings. Similar to the sinterings, the occurrence of $La_2Zr_2O_7$ also originates from Li loss for the dilatometry analysis. The significantly higher amount of $La_2Zr_2O_7$ in the pellets after sintering implies a considerably high Li loss. There are two causes for the remarkably high Li loss. Firstly, there was a continuous flow of synthetic air throughout the dilatometry analysis. The flowing air effectively removes the volatile Li from the sample, drastically increasing the Li loss. Secondly, there was no bed powder that could provide extra Li to reduce the loss. An additional explanation is the high temperature of 1250 °C, which probably increased the total loss even more.

5.2.3 Secondary phases on the surface

As mentioned, no $La_2Zr_2O_7$ was observed at the surface of the sintered pellets. However, La_2O_3 and Li_4SiO_4 were found on the pristine pellet surfaces, as demonstrated in Figure 4.15. In the same way as for $La_2Zr_2O_7$, the presence of La_2O_3 may point to a substantial Li loss and decomposition of LLZO (Equation 2.7).

Figure C.5 and Figure C.6 show that the lithium silicate impurity phase, Li_4SiO_4, was discovered at all pellet surfaces after sintering, both for sintering in Al_2O_3 and MgO crucibles. In reviewing the literature, no discoveries of lithium silicate contaminations are reported. Therefore, it is somewhat surprising that Li_4SiO_4 was located on all surfaces. It is believed that the lithium silicate phase originates from Si (s), unintentionally supplied to the pellet surface from an external source. Si can oxidize into acidic SiO_2, which can further react with alkaline Li_2O to form Li_4SiO_4. The phase diagram of the Li_2O-SiO_2 system, presented in Figure F.2 in Appendix F, verifies that Li_4SiO_4 is a possible phase in this system. One particular concern with the Li_4SiO_4 impurity phase is that it can accumulate at grain boundaries and thereby diminish the ionic transport. However, a few studies have reported that Li_4SiO_4 can be used as a sintering aid, leading to a slight increase in ionic conductivity [57, 58]. Only small amounts of Li_4SiO_4 were found to

be beneficial, as larger amounts decreased the relative density. Note that these studies intentionally added the Li_4SiO_4 into the powder before pressing pellets. There is probably a difference between intentional addition to the bulk and unintentional contamination of the surface when it comes to the presence of Li_4SiO_4.

It seems possible that the Si stems from residues of Si-containing compounds present on the lab equipment used for powder preparation. However, this theory does not fully explain why Li_4SiO_4 was located only on the pellet surfaces. It is more likely that Si was present on the pressing tools and thereby contaminated the external surfaces of the pellets during pressing. Another explanation can be that Si dust from the refractory material inside the furnace has come in contact with the pellets. However, this seems unlikely as the lids and bed powder provided complete protection against dust and sprinkles from the furnace. Regardless of the source of Si, the presence of impurities emphasized the importance of cleanliness and precautions when working in a shared lab. A thorough assessment of the possible source of contamination was not conclusive. The absence of Li_4SiO_4 peaks in the X-ray diffraction patterns for all sintered pellets implies a low concentration of this impurity phase in the bulk of the samples. The fact that Li_4SiO_4 is only present on the surface is encouraging, as it can be removed by polishing, which is beneficial for the subsequent EIS measurements.

5.3 Microstructure and densification

5.3.1 Dilatometry analysis

The dilatometry analysis was conducted to observe the densification behavior of Ta-doped LLZO. Figure 4.3 shows that the highest rate of densification occurs at approximately 1100 °C for both samples. This was the basis for the choice of sintering temperature. It was considered reasonable to choose a temperature 50 °C above the point where the grain growth rate increased sharply, as the minimum temperature required for sintering is assumed to be somewhat higher than the maximum densification rate. The main difference between the samples is the discrepancy observed in the curve for $Li_{6.75}La_3Zr_{1.75}Ta_{0.25}O_{12}$, occurring just before reaching 1250 °C. The densification is expected to continue increas-

ing when approaching the holding temperature, but instead, it slightly decreases. This sintering setback is likely due to the formation of $La_2Zr_2O_7$, which is known to slow down the sintering. As previously stated, $La_2Zr_2O_7$ forms due to high Li loss. The particularly high Li loss that starts before reaching 1250 °C indicates that such high sintering temperatures should be avoided.

According to the dilatometry curves, the $Li_{6.75}La_3Zr_{1.75}Ta_{0.25}O_{12}$ sample undergoes the largest shrinkage. However, the deviation between the Archimedes' relative densities for the two compositions is not particularly large, as seen in Figure 4.8 and Figure 4.13. Generally, within the same sintering program, the $Li_{6.4}La_3Zr_{1.4}Ta_{0.6}O_{12}$ samples are denser. This is consistent with the microstructures shown in Figure 4.14. For instance, by comparing the 6 h sinterings, it is clear that the $Li_{6.4}La_3Zr_{1.4}Ta_{0.6}O_{12}$ sample (Figure 4.14h) has a larger proportion of large grains compared to the $Li_{6.75}La_3Zr_{1.75}Ta_{0.25}O_{12}$ sample (Figure 4.14d). There is no apparent explanation for these observations. However, a closer inspection of the data in Table B.2 shows a potential correlation between the green relative density and the Archimedes' relative density. A higher green relative density seems to give a higher sintered relative density. This is especially evident for the samples sintered in MgO crucibles. The fact that the $Li_{6.4}La_3Zr_{1.4}Ta_{0.6}O_{12}$ samples tend to have a higher green density than the $Li_{6.75}La_3Zr_{1.75}Ta_{0.25}O_{12}$ samples may explain their high Archimedes' relative density.

5.3.2 Effect of holding time

As expected, the difference between samples sintered for 1 h and 6 h is more significant. Longer holding times generally lead to higher sintered density and less porosity. This may be due to enhanced diffusion, which decreases the porosity. The grains tend to be coarser when the holding time increases, probably because the grain boundary surface area is reduced. The difference in density between 1 h and 6 h is most apparent for the sinterings in MgO crucible (Figure 4.13). Based on the Archimedes' relative densities found in this work, the sintering holding time seems to be the factor with the most significant influence on the density. It is important to keep in mind that there are uncertainties related to the Archimedes' measurements, which may obscure the differences between the

relative density of the samples. Also, it is reasonable to assume that the relative density is influenced by other factors, like powder processing, milling, or other steps prior to the pressing.

5.3.3 Presence of coarse grains

Figure 4.10 shows the presence of large grains in the $Li_{6.4}La_3Zr_{1.4}Ta_{0.6}O_{12}$ sample sintered for 6 h in an Al_2O_3 crucible. These grains were only found near the surface and not in the rest of the bulk. The largest observed grains had a size of approximately 90 μm. As seen in the figure, there are isolated pores within some of the grains. This indicates that the grain boundaries moved very fast during sintering, resulting in trapped pores inside the grains. Such pores are difficult to eliminate, and they can reduce the cross-sectional area available for transport of Li-ions and consequently reduce the ionic conductivity. Such large grains can also cause mechanical weakness due to their loose grain boundaries.

Since the large grains were not abnormally large, their occurrence is not considered to be AGG. However, the coarse grains deviate from the rest due to their size; thus, it is probably an early stage of AGG. Nevertheless, the coarse grains probably result from a discontinuous grain growth during sintering, where some grains grow much faster than the average [49]. The varying growth rate can be caused by a non-uniform particle size in the powders used to press the pellets. A wide distribution in particle size may be due to insufficient ball milling of the powders. The presence of agglomerates can also be an explanation. Hard agglomerates will be sintered first and tend to grow into large grains. A finer powder with a more narrow particle size distribution could provide a denser sample with a more homogeneous microstructure. In addition, a wide particle size distribution or the presence of agglomerates in the powders may also explain the observed bimodal grain size distribution in the sintered pellets.

Another possible explanation for the unusual coarse grains is Al-contamination from the Al_2O_3 crucibles. The coarse grains were only present in the sample sintered in an Al_2O_3 crucible, and not in any of the samples sintered in MgO crucibles. It is believed that the bed powder did not provide a sufficient barrier between the sample and the crucible during sintering of the pellet containing these large grains. This could cause Al from the

crucible to contaminate the pellet surface and initiate AGG. AGG usually occurs during sintering at high temperatures and long dwell times, and in the presence of Al. AGG is more frequently observed in Al-doped LLZO than in Ta-doped LLZO.

5.4 Ionic conductivity

The ionic conductivity of sintered Ta-doped LLZO samples depends on the phase composition, Ta content, density, and microstructure. The Nyquist diagrams, shown in Figure 4.16 and Figure 4.17, all have two semicircles arising from the bulk and grain boundary contributions. This means that the contribution from the grain boundaries is significant and should not be neglected. The bulk resistance is expected to be lower than that of the grain boundaries because the cubic phased Ta-doped LLZO is a good Li-ion conductor.

5.4.1 Total ionic conductivity

The bulk and total ionic conductivity values are given in Table 4.1. The highest total ionic conductivity was found to be $1.66 \cdot 10^{-4}$ S cm^{-1} for $Li_{6.4}La_3Zr_{1.4}Ta_{0.6}O_{12}$ sintered at 1150 °C for 6 h in a MgO crucible with BP-ratio 2. This is somewhat lower than the total ionic conductivity values in the literature (Table 2.1). However, all total ionic conductivities achieved in this work are $> 10^{-4}$ S cm^{-1}, which is in line with what is expected for sintering in ambient air. Both $Li_{6.75}La_3Zr_{1.75}Ta_{0.25}O_{12}$ samples consisted of a mixture of cubic and tetragonal phase after sintering (Figure 4.11) and are therefore expected to have a lower total ionic conductivity than the pure cubic $Li_{6.4}La_3Zr_{1.4}Ta_{0.6}O_{12}$ samples. This is true for the samples sintered for 6 h, as the $Li_{6.75}La_3Zr_{1.75}Ta_{0.25}O_{12}$ sample has lower total ionic conductivity than the $Li_{6.4}La_3Zr_{1.4}Ta_{0.6}O_{12}$ sample. Surprisingly, the opposite is true for the samples sintered for 1 h. This unexpected outcome may have been affected by the presence of $La_2Zr_2O_7$. As can be seen in Figure 4.11, the $Li_{6.4}La_3Zr_{1.4}Ta_{0.6}O_{12}$ sample sintered for 1 h contained the highest amount of $La_2Zr_2O_7$, according to the relative peak intensities. It seems possible that the $La_2Zr_2O_7$ caused the reduced total ionic conductivity.

For the $Li_{6.4}La_3Zr_{1.4}Ta_{0.6}O_{12}$ samples, the total ionic conductivity increases with sintering

time and density, which is expected. However, the $Li_{6.75}La_3Zr_{1.75}Ta_{0.25}O_{12}$ samples unexpectedly show the opposite. This outcome may suggest that the total ionic conductivity is likely more affected by the presence $La_2Zr_2O_7$ rather than the sintering time and density. It seems that a large amount of $La_2Zr_2O_7$, like in $Li_{6.4}La_3Zr_{1.4}Ta_{0.6}O_{12}$ sintered for 1h, lowers the total ionic conductivity more than when the $La_2Zr_2O_7$ amount is low. Keep in mind that the densities were quite similar. A greater variation in density values would probably clarify how the density impacts the ionic conductivity. Regarding the tetragonal phase, there is no indication that its presence results in an exceedingly lower total ionic conductivity. The literature clearly states that the tetragonal phase has a significantly lower ionic conductivity than the cubic phase. Therefore, it was highly unexpected to observe the lack of impact it had on the total ionic conductivity. It should be emphasized that the amount of tetragonal phase is not determined in this work. Hence, there may be only a small amount of tetragonal phase present, which can explain why its presence seems to have such a small impact on the ionic conductivity.

Overall, it seems like a high $La_2Zr_2O_7$ content is what lowers the total ionic conductivity most, even more than the presence of the tetragonal phase. The fact that no other clear trends were observed for the total ionic conductivities makes it challenging to point to distinct reasons for the outcome. Either way, the highest value achieved in this work was for the pure cubic $Li_{6.4}La_3Zr_{1.4}Ta_{0.6}O_{12}$ sample sintered for 6 h in an MgO crucible, which had the highest relative density as well.

5.4.2 Bulk ionic conductivity

Turning now to the bulk ionic conductivities, the $Li_{6.75}La_3Zr_{1.75}Ta_{0.25}O_{12}$ samples have the highest values, of $4.00 \cdot 10^{-4}$ S cm^{-1} and $3.95 \cdot 10^{-4}$ S cm^{-1} for 1 h and 6 h holding times, respectively. In contrast, their total ionic conductivities differ more, with $1.49 \cdot 10^{-4}$ S cm^{-1} for 1 h and $1.17 \cdot 10^{-4}$ S cm^{-1} for 6 h. The fact that the bulk conductivities are approximately equal indicates that the difference in total conductivity is caused by the grain boundaries. The grain boundary contribution is higher for the 1 h sample, which may be due to the larger amount of smaller grains and thus also the higher fraction of grain boundaries. The $Li_{6.4}La_3Zr_{1.4}Ta_{0.6}O_{12}$ samples have a somewhat lower bulk ionic

conductivity compared to the $Li_{6.75}La_3Zr_{1.75}Ta_{0.25}O_{12}$ samples. However, bulk ionic conductivity values between 10^{-4} S cm^{-1} and 10^{-3} S cm^{-1} are generally considered sufficient [8], as stated in Section 2.5.

From the ionic conductivity values obtained in this work, there is no clear trend on the effect of Ta content. The absence of clear trends has generally been a recurring issue regarding the ionic conductivity results. Uncertainties, both in the measurements and fitting, have probably influenced the results to a certain degree and affected the accuracy of the reported values. Besides, Ta-doped LLZO is a sensitive system that seems to be easily affected by external factors like atmosphere, temperature, storage, and time of the day. This increases the challenges with reproducibility. In addition, few samples were sintered in each sintering program. Ideally, more parallels should have been conducted to improve the reproducibility of the results. However, the obtained ionic conductivity values showed a somewhat low variance, even though there were no apparent trends.

6 Conclusion

This work studied the sintering properties and Li-ion conductivity of Ta-doped LLZO with compositions $Li_{6.75}La_3Zr_{1.75}Ta_{0.25}O_{12}$ and $Li_{6.4}La_3Zr_{1.4}Ta_{0.6}O_{12}$, produced by spray pyrolysis. The goal was to obtain a material with high phase purity, high relative density, and high ionic conductivity. The key findings in this work are summarized as follows:

- A total ionic conductivity of $1.66 \cdot 10^{-4}$ S cm^{-1} and a relative density of 92 % were achieved for $Li_{6.4}La_3Zr_{1.4}Ta_{0.6}O_{12}$ samples sintered in ambient air at 1150 °C for 6 h in a MgO crucible with a BP-ratio of 2. This sintering program resulted in pure cubic Ta-doped LLZO without secondary phases. Sintering in Al_2O_3 crucibles was found to be suboptimal for Ta-doped LLZO due to the risk of Al contamination.

- The presence of $La_2Zr_2O_7$ in sintered samples significantly influenced on the ionic conductivity. A higher amount of $La_2Zr_2O_7$ was found to give a substantial decrease in ionic conductivity, as opposed to lower amounts. The formation of $La_2Zr_2O_7$ is prominent when the Li loss is high. Due to the repeated occurrence of $La_2Zr_2O_7$ in sintered samples, the Li excess of 24.2 mol% in Ta-doped LLZO is likely too low.

- $Li_{6.75}La_3Zr_{1.75}Ta_{0.25}O_{12}$ samples contained a mixture of tetragonal and cubic phase after sintering. The presence of the tetragonal phase did not have a considerable effect on the ionic conductivity, probably due to the low amount. No apparent influence of Ta content on ionic conductivity was found in this work.

- It was revealed that a sintering holding time of 6 h reduces the $La_2Zr_2O_7$ formation compared to sintering for 1 h. A longer holding time makes it possible to transfer a significant amount of Li from the bed powder and into the pellet, thus suppressing the formation of $La_2Zr_2O_7$ to a greater extent.

7 Further work

Future studies should focus on measures to eliminate the $La_2Zr_2O_7$ secondary phase in sintered pellets. A good strategy to retain more Li during sintering should be established. Suggestions can be to add a larger Li excess or to use more bed powder. Since the tetragonal phase contains more Li than the cubic phase, it would be beneficial to use a tetragonal bed powder. The Li loss during spray pyrolysis, calcination, and powder processing resulted in a lower Li excess than anticipated according to nominal compositions. Therefore, ICP (inductively coupled plasma) should be applied to determine the correct stoichiometry of the powders, both as received from spray pyrolysis and calcined.

A further process should aim to increase the relative density of sintered samples. Sintering techniques like two-step sintering, hot isostatic pressing, or spark plasma sintering can be applied to achieve higher pellet densities. Actions to improve the microstructure should also be implemented. A process that produces small grains with tight grain boundaries should be developed. A denser sample with a more homogeneous microstructure can further increase the ionic conductivity. Furthermore, efforts should be made to improve the reproducibility of the results. Performing multiple parallels for each sintering program is an important action. It is also possible to test other sintering temperatures and holding times to get a better insight into their effect on microstructure and ionic conductivity.

8 Acknowledgement

I would like to express my deepest appreciation to Cerpotech AS for making this work possible. I would also like to thank Assoc. Prof. Daniel Rettenwander for his encouragement, generosity and valuable advice. My sincere thanks go to Ph.D. candidate Florian Flatscher for his assistance with preparing and executing the EIS measurements. His contributions to my work have been beyond helpful. I am also grateful for the help offered by Ph.D. candidate Hung Quoc Nguyen regarding fitting of the EIS data.

Furthermore, I gratefully recognize senior engineer Yingda Yu for his help operating the SEM. Thank you for taking the time to facilitate my work and for not hesitating to share knowledge. A special thanks go to staff engineer Pei Na Kui for all training and assistance regarding the dilatometry analysis. I would also like to acknowledge the rest of the engineers and laboratory staff at IMA for their technical assistance and guidance.

Bibliography

[1] S. R. Yeandel, B. J. Chapman, P. R. Slater and P. Goddard, "Structure and lithium-ion dynamics in fluoride-doped cubic $Li_7La_3Zr_2O_{12}$ (LLZO) garnet for Li solid-state battery application", *The Journal of Physical Chemistry C*, vol. 122, pp. 27 811–27 819, Nov. 2018. DOI: 10.1021/acs.jpcc.8b07704. [Online]. Available: https://pubs.acs.org/doi/10.1021/acs.jpcc.8b07704.

[2] J.-M. Tarascon and M. Armand, "Issues and challenges facing rechargeable lithium batteries", *Nature*, vol. 414, pp. 359–367, Nov. 2001. [Online]. Available: https://www.nature.com/articles/35104644.

[3] J. G. Kim, B. Son, S. Mukherjee, N. Schuppert, A. Bates, O. Kwon, M. J. Choi, H. Y. Chung and S. Park, "A review of lithium and non-lithium based solid state batteries", *Journal of Power Sources*, vol. 282, pp. 299–322, May 2015. DOI: 10.1016/j.jpowsour.2015.02.054. [Online]. Available: https://www.sciencedirect.com/science/article/abs/pii/S0378775315002773.

[4] X. Feng, M. Ouyang, X. Liu, L. Lu, Y. Xia and X. He, "Thermal runaway mechanism of lithium ion battery for electric vehicles: A review", *Energy Storage Materials*, vol. 10, pp. 246–267, May 2017. DOI: http://dx.doi.org/10.1016/j.ensm.2017.05.013. [Online]. Available: https://www.sciencedirect.com/science/article/abs/pii/S2405829716303464.

[5] H. Z. anf Yang Yang, D. Ren, L. Wang and X. He, "Graphite as anode materials: Fundamental mechanism, recent progress and advances", *Energy Storage Materials*, vol. 36, pp. 147–170, Apr. 2021. DOI: 10.1016/j.ensm.2020.12.027. [Online]. Available: https://www.sciencedirect.com/science/article/pii/S2405829720304906.

[6] W. Xu, J. Wang, F. Ding, X. Chen, E. Nasybulin, Y. Zhang and J.-G. Zhang, "Lithium metal anodes for rechargeable batteries", *Energy Environ. Sci.*, vol. 7, no. 2, pp. 513–537, 2014. DOI: 10.1039/C3EE40795K. [Online]. Available: https://pubs.rsc.org/en/content/articlelanding/2014/EE/C3EE40795K.

[7] Z. Hu, J. Li, X. Zhang and Y. Zhu, "Strategies to improve the performance of li metal anode for rechargeable batteries", *Frontiers in Chemistry*, vol. 8, May 2020. DOI: 10.3389/fchem.2020.00409. [Online]. Available: https://www.frontiersin.org/articles/10.3389/fchem.2020.00409/full.

[8] Q. Liu, Z. Geng, C. Han, Y. Fu, S. Li, Y.-b. He, F. Kang and B. Li, "Challenges and perspectives of garnet solid electrolytes for all solid-state lithium batteries", *Journal of Power Sources*, vol. 389, pp. 120–134, Jun. 2018. DOI: 10.1016/j.jpowsour.2018.04.019. [Online]. Available: https://www.sciencedirect.com/science/article/abs/pii/S0378775318303628.

[9] X.-B. Cheng, R. Zhang, C.-Z. Zhao and Q. Zhang, "Toward safe lithium metal anode in rechargeable batteries: A review", *Chemical Reviews*, vol. 117, no. 55, pp. 10 403–10 473, Aug. 2017. DOI: 10.1021/acs.chemrev.7b00115. [Online]. Available: https://pubs.acs.org/doi/10.1021/acs.chemrev.7b00115.

[10] F. Wu, J. Maier and Y. Yu, "Guidelines and trends for next-generation rechargeable lithium and lithium-ion batteries", *Chemial Society Reviews*, vol. 49, no. 5, pp. 1569–1614, Feb. 2020. DOI: 10.1039/c7cs00863e. [Online]. Available: https://pubs.rsc.org/en/content/articlelanding/2020/CS/C7CS00863E.

[11] X. Huang, Y. Lu, Z. Song, K. Rui, Q. Wang and T. Xiu, "Manipulating Li_2O atmosphere for sintering dense $Li_7La_3Zr_2O_{12}$ solid electrolyte", *Energy Storage Materials*, vol. 22, pp. 207–217, Nov. 2019. DOI: 10.1016/j.ensm.2019.01.018. [Online]. Available: https://www.sciencedirect.com/science/article/abs/pii/S2405829718313552.

[12] Y. Tian, Y. Zhou, Y. Liu, C. Zhao, W. Wang and Y. Zhou, "Formation mechanism of sol-gel synthesized $Li_{7-3x}Al_xLa_3Zr_2O_{12}$ and the influence of abnormal grain growth on ionic conductivity", *Solid State Ionics*, vol. 354, p. 115 407, Oct. 2020. DOI: 10.1016/j.ssi.2020.115407. [Online]. Available: https://www.sciencedirect.com/science/article/abs/pii/S0167273820304616?.

[13] H. K. Herskedal, "Phase stability and sintering properties of $Li_{7-x}La_3Zr_{2-x}Ta_xO_{12}$ produced by spray pyrolysis (x = 0.25 and 0.6)", NTNU, Trondheim, Tech. Rep., Dec. 2021.

[14] Y. Matsuda, K. Sakamoto, M. Matsui, O. Yamamoto, Y. Takeda and N. Imanishi, "Phase formation of a garnet-type lithium-ion conductor $Li_{7-3x}Al_xLa_3Zr_2O_{12}$", *Solid State Ionics*, vol. 277, pp. 23–29, Sep. 2015. DOI: 10.1016/j.ssi.2015.04.011. [Online]. Available: https://www.sciencedirect.com/science/article/abs/pii/S0167273815001587.

[15] L. Dhivya and R. Murugan, "Effect of simultaneous substitution of Y and Ta on the stabilization of cubic phase, microstructure, and Li^+ conductivity of $Li_7La_3Zr_2O_{12}$ lithium garnet", *ACS Appl. Mater. Interfaces*, vol. 6, no. 20, pp. 17 606–17 615, Sep. 2014. DOI: 10.1021/am503731h. [Online]. Available: https://pubs.acs.org/doi/10.1021/am503731h.

[16] S. Cao *et al.*, "Modeling, preparation, and elemental doping of $Li_7La_3Zr_2O_{12}$ garnet-type solid electrolytes: A review", *Journal of the Korean Ceramic Society*, vol. 56, no. 2, pp. 111–129, 2019. DOI: 10.4191/kcers.2019.56.2.01. [Online]. Available: https://www.jkcs.or.kr/journal/view.php?doi=10.4191/kcers.2019.56.2.01.

[17] A. Kim, S. Woo, M. Kang, H. Park and B. Kang, "Research progresses of garnet-type solid electrolytes for developing all-solid-state li batteries", *Frontiers in Chemistry*, vol. 8, no. 468, Jun. 2020. DOI: 10.3389/fchem.2020.00468. [Online]. Available: https://www.frontiersin.org/article/10.3389/fchem.2020.00468.

[18] J. Awaka, A. Takashima, K. Kataoka, N. Kijima, Y. Idemoto and J. Akimoto, "Crystal structure of fast lithium-ion-conducting cubic $Li_7La_3Zr_2O_{12}$", *Chemistry Letters*, vol. 40, pp. 60–62, Jan. 2011. DOI: 10.1246/cl.2011.60. [Online]. Available: https://www.journal.csj.jp/doi/10.1246/cl.2011.60.

[19] J. Awaka, N. Kijima, H. Hayakawa and J. Akimoto, "Synthesis and structure analysis of tetragonal $Li_7La_3Zr_2O_{12}$ with the garnet-related type structure", *Journal of Solid State Chemistry*, vol. 182, no. 8, pp. 2046–2052, Aug. 2019. DOI: 10.1016/j.jssc.2009.05.020. [Online]. Available: https://www.sciencedirect.com/science/article/abs/pii/S002245960900228X.

[20] X. Zhang, T.-S. Oh and J. W. Fergus, "Densification of Ta-doped garnet-type $Li_{6.75}La_3Zr_{1.75}Ta_{0.25}O_{12}$ solid electrolyte materials by sintering in a lithium-rich air atmosphere", *Journal of The Electrochemical Society*, vol. 166, no. 15, A3753–A3759, Nov. 2019. DOI: 10.1149/2.1031915jes. [Online]. Available: https://iopscience.iop.org/article/10.1149/2.1031915jes.

[21] M. Matsui, K. Takahashi, K. Sakamoto, A. Hirano, Y. Takeda, O. Yamamoto and N. Imanishi, "Phase stability of a garnet-type lithium ion conductor $Li_7La_3Zr_2O_{12}$", *Dalton Transactions*, vol. 43, no. 3, pp. 1019–1024, Oct. 2013. DOI: 10.1039/C3DT52024B. [Online]. Available: https://pubs.rsc.org/en/content/articlelanding/2014/DT/C3DT52024B.

[22] G. Larraz, A. Orera, J. Sanz, I. Sobrados, V. Diez-Gómez and M. L. Sanjuán, "Nmr study of Li distribution in $Li_{7-x}H_xLa_3Zr_2O_{12}$ garnets", *Journal of Materials Chemistry A*, vol. 3, no. 3, pp. 5683–5691, Jan. 2015. DOI: 10.1039/c4ta04570j. [Online]. Available: https://pubs.rsc.org/en/content/articlelanding/2015/TA/C4TA04570J.

[23] G. Larraz, A. Orera and M. L. Sanjuán, "Cubic phases of garnet-type $Li_7La_3Zr_2O_{12}$: The role of hydration", *Journal of Materials Chemistry A*, vol. 1, no. 37, pp. 11 419–11 428, Jul. 2013. DOI: 10.1039/c3ta11996c. [Online]. Available: https://pubs.rsc.org/en/content/articlelanding/2013/TA/c3ta11996c.

[24] N. Bernstein, M. D. Johannes and K. Hoang, "Origin of the structural phase transition in $Li_7La_3Zr_2O_{12}$", *Physical Review Letters*, vol. 109, no. 20, p. 205 702, Nov. 2012. DOI: 10.1103/PhysRevLett.109.205702. [Online]. Available: https://journals.aps.org/prl/abstract/10.1103/PhysRevLett.109.205702.

[25] N. Janani, S. Ramakumar, L. Dhivya, C. Deviannapoorani, K. Saranya and R. Murugan, "Synthesis of cubic $Li_7La_3Zr_2O_{12}$ by modified sol–gel process", *Ionics*, vol. 17, no. 575, pp. 575–580, Aug. 2011. DOI: 10.1007/s11581-011-0611-x. [Online]. Available: https://link.springer.com/article/10.1007/s11581-011-0611-x.

[26] Y. Chen, E. Rangasamy, C. R. dela Cruz, C. Liangb and K. An, "A study of suppressed formation of low-conductivity phases in doped $Li_7La_3Zr_2O_{12}$ garnets by in situ neutron diffraction", *Journal of Materials Chemistry A*, vol. 3, no. 45, pp. 22 868–22 876, Sep. 2015. DOI: 10.1039/c5ta04902d. [Online]. Available: https://pubs.rsc.org/en/content/articlelanding/2015/TA/C5TA04902D.

[27] C. A. Geiger, E. Alekseev, B. Lazic, M. Fisch, T. Armbruster, R. Langner, M. Fechtelkord, N. Kim, T. Pettke and W. Weppner, "Crystal chemistry and stability of "$Li_7La_3Zr_2O_{12}$" garnet: A fast lithium-ion conductor", *Inorganic Chemistry*, vol. 50, no. 3, pp. 1089–1097, Dec. 2010. DOI: 10.1021/ic101914e. [Online]. Available: https://pubs.acs.org/doi/10.1021/ic101914e.

[28] T. Thompson, J. Wolfenstine, J. L. Allen, M. Johannes, A. Huq, I. N. David and J. Sakamoto, "Tetragonal vs. cubic phase stability in Al–free Ta doped $Li_7La_3Zr_2O_{12}$ (LLZO)", *Journal of Materials Chemistry A*, vol. 2, no. 33, pp. 13 431–13 436, Jun. 2014. DOI: 10.1039/c4ta02099e. [Online]. Available: https://pubs.rsc.org/en/content/articlelanding/2014/TA/C4TA02099E.

[29] A. Paolella *et al.*, "Discovering the influence of lithium loss on garnet $Li_7La_3Zr_2O_{12}$ electrolyte phase stability", *ACS Applied Energy Materials*, vol. 3, no. 4, pp. 3415–3424, Feb. 2020. DOI: 10.1021/acsaem.9b02401. [Online]. Available: https://pubs.acs.org/doi/10.1021/acsaem.9b02401.

[30] Y. Wang and W. Lai, "Phase transition in lithium garnet oxide ionic conductors $Li_7La_3Zr_2O_{12}$: The role of Ta substitution and H_2O/CO_2 exposure", *Journal of Power Sources*, vol. 275, pp. 612–620, Feb. 2015. DOI: 10.1016/j.jpowsour.2014.11.062. [Online]. Available: https://www.sciencedirect.com/science/article/pii/S0378775314018898.

[31] E. Rangasamy, J. Wolfenstine and J. Sakamoto, "The role of Al and Li concentration on the formation of cubic garnet solid electrolyte of nominal composition $Li_7La_3Zr_2O_{12}$", *Solid State Ionics*, vol. 206, pp. 28–32, Nov. 2012. DOI: 10.1016/j.ssi.2011.10.022. [Online]. Available: https://www.sciencedirect.com/science/article/abs/pii/S0167273811005297.

[32] H. Salimkhani, S. A. Gursel and A. Yurum, "A glance at the influence of different dopant elements on $Li_7La_3Zr_2O_{12}$ garnets", *Ionics*, vol. 27, no. 9, pp. 3673–3698, Sep. 2021. DOI: 10.1007/s11581-021-04152-4. [Online]. Available: https://link.springer.com/article/10.1007/s11581-021-04152-4.

[33] J. Allen, J. Wolfenstine, E. Rangasamy and J. Sakamoto, "Effect of substitution (Ta, Al, Ga) on the conductivity of $Li_7La_3Zr_2O_{12}$", *Journal of Power Sources*, vol. 206, pp. 315–319, Jan. 2011. DOI: 10.1016/j.jpowsour.2012.01.131. [Online]. Available: https://www.sciencedirect.com/science/article/abs/pii/S0378775312002753.

[34] Y. Li, J.-T. Han, C.-A. Wang, H. Xieb and J. B. Goodenough, "Optimizing Li^+ conductivity in a garnet framework", *Journal of Materials Chemistry*, vol. 22, no. 30, pp. 15 357–15 361, Jun. 2012. DOI: 10.1039/c2jm31413d. [Online]. Available: https://pubs.rsc.org/en/content/articlelanding/2012/JM/c2jm31413d.

[35] R. Shannon, *Revised Effective Ionic Radii and Systematic Studies of Interatomic Distances in Halides and Chalcogenides*, A32. Acta Crystallographica, 1976, pp. 751–767.

[36] Y. Wang and W. Lai, "High ionic conductivity lithium garnet oxides of $Li_{7-x}La_3Zr_{2-x}Ta_xO_{12}$ compositions", *Electrochemical and Solid-State Letters*, vol. 16, A68, Feb. 2012. DOI: 10.1149/2.024205esl. [Online]. Available: https://iopscience.iop.org/article/10.1149/2.024205esl.

[37] M. Matsui, K. Sakamoto, K. Takahashi, A. Hirano, Y. Takeda, O. Yamamoto and N. Imanishi, "Phase transformation of the garnet structured lithium ion conductor: $Li_7La_3Zr_2O_{12}$", *Solid State Ionics*, vol. 262, pp. 155–159, Oct. 2014. DOI: 10.1016/j.ssi.2013.09.027. [Online]. Available: https://www.sciencedirect.com/science/article/pii/S0167273813004360.

[38] J. Cai *et al.*, "Stoichiometric irreversibility of aged garnet electrolytes", *Materials Today Energy*, vol. 20, p. 100 669, Feb. 2021. DOI: 10.1016/j.mtener.2021.100669. [Online]. Available: https://www.sciencedirect.com/science/article/pii/S2468606921000344.

[39] R. S. Roth, "Pyrochlore-type compounds containing double oxides of trivalent and tetravalent ions", *Journal of Research of the National Bureau of Standards*, vol. 56, no. 1, pp. 17–25, Jan. 1956. [Online]. Available: https://nvlpubs.nist.gov/nistpubs/jres/56/jresv56n1p17_A1b.pdf.

[40] X. Huang, C. Shen, K. Rui, J. Jin, M. Wu, X. Wu and Z. Wen, "Influence of $La_2Zr_2O_7$ additive on densification and Li^+ conductivity for Ta-doped $Li_7La_3Zr_2O_{12}$ garnet", *JOM*, vol. 68, no. 10, pp. 2593–2600, Aug. 2016. DOI: 10.1007/s11837-016-2065-0. [Online]. Available: https://link.springer.com/article/10.1007/s11837-016-2065-0.

[41] M. Kotobuki, E. Hanc, B. Yan, J. Molenda and L. Lu, "Stabilization of cubic $Li_7La_3Zr_2O_{12}$ by Al substitution in various atmospheres", *Solid State Ionics*, vol. 350, p. 115 323, Jul. 2020. DOI: 10.1016/j.ssi.2020.115323. [Online]. Available: https://www.sciencedirect.com/science/article/abs/pii/S0167273820300217.

[42] A. Skokan, "Phase stability investigations in the ceramic breeder systems Li2O-Al2O3 and Li2O-ZrO2", in *Fusion Technology 1990*, B. KEEN, M. HUGUET and R. HEMSWORTH, Eds., Oxford: Elsevier, 1991, pp. 772–776, ISBN: 978-0-444-88508-1. DOI: 10.1016/B978-0-444-88508-1.50139-0. [Online]. Available: https://www.sciencedirect.com/science/article/pii/B9780444885081501390.

[43] B. Gao, R. Jalem and Y. Tateyama, "Atomistic insight into the dopant impacts at the garnet $Li_7La_3Zr_2O_{12}$ solid electrolyte grain boundaries", *Journal of Materials Chemistry A*, vol. 10, no. 18, pp. 10 083–10 091, Apr. 2022. DOI: 10.1039/d2ta00545j. [Online]. Available: https://pubs.rsc.org/en/content/articlelanding/2022/TA/D2TA00545J.

[44] K. Hayashi, H. Noguchi and S. Fujiwara, "Guidelines and trends for next-generation rechargeable lithium and lithium-ion batteries", *Materials Research Bulletin*, vol. 21, no. 3, pp. 289–293, 1986. DOI: 10.1016/0025-5408(86)90184-4. [Online]. Available: https://www.sciencedirect.com/science/article/pii/0025540886901844.

[45] X. Huang, C. Liu, Y. Lu, T. Xiu, J. Jin, M. E. Badding and Z. Wen, "A Li-garnet composite ceramic electrolyte and its solid-state Li-S battery", *Journal of Power Sources*, vol. 382, pp. 190–197, Apr. 2018. DOI: 10.1016/j.jpowsour.2017.11.074. [Online]. Available: https://www.sciencedirect.com/science/article/abs/pii/S0378775317315574.

[46] I. McColm and N. Clark, *High-Performance Ceramics*. Blackie and Son, 1988, pp. 208–246.

[47] L. Yang, Q. Dai, L. Liu, D. Shao, K. Luo, S. Jamil, H. Liu, Z. Luo, B. Chang and X. Wang, "Rapid sintering method for highly conductive $Li_7La_3Zr_2O_{12}$ ceramic electrolyte", *Ceramics International*, vol. 46, no. 8, Part A, pp. 10 917–10 924, Jan. 2020. DOI: 10.1016/j.ceramint.2020.01.106. [Online]. Available: https://www.sciencedirect.com/science/article/pii/S0272884220301073.

[48] X. Huang, T. Xiu, M. E. Badding and Z. Wen, "Two-step sintering strategy to prepare dense Li-garnet electrolyte ceramics with high Li^+ conductivity", *Ceramics International*, vol. 44, no. 5, pp. 5660–5667, Apr. 2018. DOI: 10.1016/j.ceramint.2017.12.217. [Online]. Available: https://www.sciencedirect.com/science/article/pii/S0272884217329255.

[49] X. Zeng, A. J. Martinolich, K. A. See and K. T. Faber, "Dense garnet-type electrolyte with coarse grains for improved air stability and ionic conductivity", *Journal of Energy Storage*, vol. 27, p. 101 128, Dec. 2020. DOI: 10.1016/j.est.2019.101128. [Online]. Available: https://www.sciencedirect.com/science/article/pii/S2352152X19306528.

[50] J. Su, X. Huang, Z. Song, T. Xiu, M. E. Badding, J. Jin and Z. Wen, "Overcoming the abnormal grain growth in ga-doped $Li_7La_3Zr_2O_{12}$ to enhance the electrochemical stability against Li metal", *Ceramics International*, vol. 45, no. 12, pp. 14 991–14 996, Aug. 2019. DOI: 10.1016/j.ceramint.2019.04.236. [Online]. Available: https://www.sciencedirect.com/science/article/pii/S0272884219310739.

[51] X. Huang, Y. Lu, Z. Song, T. Xiu, M. E. Badding and Z. Wen, "Preparation of dense Ta-LLZO/MgO composite Li-ion solid electrolyte: Sintering, microstructure, performance and the role of MgO", *Journal of Energy Chemistry*, vol. 39, pp. 8–16, Jan. 2019. DOI: 10.1016/j.jechem.2019.01.013. [Online]. Available: https://www.sciencedirect.com/science/article/abs/pii/S2095495618309161.

[52] Y. Li, Y. Cao and X. Guo, "Influence of lithium oxide additives on densification and ionic conductivity of garnet-type $Li_{6.75}La_3Zr_{1.75}Ta_{0.25}O_{12}$ solid electrolytes", *Solid State Ionics*, vol. 253, pp. 76–80, Dec. 2013. DOI: 10.1016/j.ssi.2013.09.005. [Online]. Available: https://www.sciencedirect.com/science/article/pii/S0167273813004049.

[53] K. Ishiguro, H. Nemori, S. Sunahiro, Y. Nakata, R. Sudo, M. Matsui, Y. Takeda, O. Yamamoto and N. Imanishi, "Ta-doped $Li_7La_3Zr_2O_{12}$ for water-stable lithium electrode of lithium-air batteries", *Journal of The Electrochemical Society*, vol. 161, no. 5, A668–A674, Mar. 2014. DOI: 10.1149/2.013405jes. [Online]. Available: https://iopscience.iop.org/article/10.1149/2.013405jes.

[54] "Basics of electrochemical impedance spectroscopy". (Apr. 2021), [Online]. Available: https://www.gamry.com/application-notes/EIS/basics-of-electrochemical-impedance-spectroscopy (visited on 4th Mar. 2022).

[55] K. H. Masaki Kato and S. Seki, "Investigation of the ionic conduction mechanism of polyether/$Li_7La_3Zr_2O_{12}$ composite solid electrolytes by electrochemical impedance spectroscopy", *Journal of The Electrochemical Society*, vol. 167, no. 7, Apr. 2020. DOI: 10.1149/1945-7111/ab8478. [Online]. Available: https://iopscience.iop.org/article/10.1149/1945-7111/ab8478.

[56] M. Joshi, "Importance of impedance spectroscopy technique in materials characterization: A brief review", *Mechanics, Materials Science & Engineering MMSE Journal*, Apr. 2017. DOI: 10.2412/mmse.42.57.345. [Online]. Available: https://hal.archives-ouvertes.fr/hal-01504661.

[57] P. Wakudkar and A. Deshpande, "Effect of Li_4SiO_4 addition in $Li_{6.22}Al_{0.16}La_3Zr_{1.7}Ta_{0.3}O_{12}$ garnet type solid electrolyte for lithium ion battery application", *Ceramics International*, vol. 45, no. 16, pp. 20 113–20 120, Nov. 2019. DOI: 10.1016/j.ceramint.2019.06.276. [Online]. Available: https://www.sciencedirect.com/science/article/pii/S0272884219317894.

[58] N. Janani, C. Deviannapoorani, L. Dhivya and R. Murugan, "Influence of sintering additives on densification and Li^+ conductivity of Al doped $Li_7La_3Zr_2O_{12}$ lithium garnet", *RSC Advances*, vol. 4, no. 93, pp. 51 228–51 238, Oct. 2014. DOI: 10.1039/C4RA08674K. [Online]. Available: https://pubs.rsc.org/en/content/articlelanding/2014/RA/C4RA08674K.

[59] N. S. Kulkarni, T. M. Besmann and K. E. Spear, "Thermodynamic optimization of lithia–alumina", *Journal of the American Ceramic Society*, vol. 19, no. 12, pp. 4074–4083, Dec. 2008. DOI: 10.1111/j.1551-2916.2008.02753.x. [Online]. Available: https://ceramics.onlinelibrary.wiley.com/doi/10.1111/j.1551-2916.2008.02753.x.

[60] A. A. Popovich, P. A. Novikov, A. O. Silin, N. G. Razumov and Q. S. Wang, "Synthesis of a Li_2FeSiO_4/c nanocrystalline cathode material for lithium-ion batteries", *Russian Journal of Applied Chemistry*, vol. 87, pp. 1268–1273, Dec. 2014. DOI: 10.1134/S1070427214090134. [Online]. Available: https://link.springer.com/article/10.1134/S1070427214090134.

Appendices

A Mass and density of pellets

The green density of pellets before sintering, ρ_i [g/cm^3], is calculated according to Equation A.1, where m_i is the pellet mass, d_i is the pellet diameter and t_i is the pellet thickness, all measured before sintering.

$$\rho_i = \frac{m_i}{V_i} = \frac{m_i}{\pi \cdot \left(\frac{d_i}{2}\right)^2 \cdot t_i} \tag{A.1}$$

The calculated density of pellets after sintering, ρ_f [g/cm^3], is found by Equation A.2, where m_f is the pellet mass, d_f is the pellet diameter and t_f is the pellet thickness, all measured after sintering.

$$\rho_f = \frac{m_f}{V_f} = \frac{m_f}{\pi \cdot \left(\frac{d_f}{2}\right)^2 \cdot t_f} \tag{A.2}$$

The theoretical densities of $Li_{6.75}La_3Zr_{1.75}Ta_{0.25}O_{12}$ and $Li_{6.4}La_3Zr_{1.4}Ta_{0.6}O_{12}$ are calculated according to Equation A.3 and Equation A.4, respectively. M_i is the molar mass of specie i, N_A is the Avogadro constant and a is the lattice constant.

$$\begin{aligned} \rho_{t\ (Ta=0.25)} &= \frac{m}{V} = \frac{nM}{V} = \frac{zM}{N_A a^3} = \frac{8M_{LLZTO}}{N_A a^3} \\ &= \frac{8}{N_A a^3}\left(6.75M_{Li} + 3M_{La} + 1.75M_{Zr} + 0.25M_{Ta} + 12M_O\right) \\ &= 5.251\ g/cm^3 \end{aligned} \tag{A.3}$$

$$\begin{aligned} \rho_{t\ (Ta=0.6)} &= \frac{m}{V} = \frac{nM}{V} = \frac{zM}{N_A a^3} = \frac{8M_{LLZTO}}{N_A a^3} \\ &= \frac{8}{N_A a^3}\left(6.4M_{Li} + 3M_{La} + 1.4M_{Zr} + 0.6M_{Ta} + 12M_O\right) \\ &= 5.469\ g/cm^3 \end{aligned} \tag{A.4}$$

The relative density (RD) of the green pellets, RD_i, and of the sintered pellets, RD_f, are calculated according to Equation A.5.

$$RD_{i,f} = \frac{\rho_{i,f}}{\rho_t} \tag{A.5}$$

The mass, dimensions, calculated densities and relative densities of green pellets and sintered pellets are presented in the following tables. Table A.1 belongs to the preliminary sintering where the BP-ratio is 1, and Tables A.2 to A.5 belong to the main sintering experiments with BP-ratios of 2.

Table A.1: Pellet measurements for 1150@1h/BP1/MgO. m_i, d_i, t_i, ρ_i and RD_i are the initial mass, diameter, thickness, calculated density and relative density (before sintering), respectively. m_f, d_f, t_f, ρ_f and RD_f are the final mass, diameter, thickness, calculated density and relative density (after sintering), respectively.

Parameter	**Sample**	
	1150@1h/BP1/MgO	
	Ta = 0.25	Ta = 0.6
$\mathbf{m_i}$ **[mg]**	578.2	570.2
$\mathbf{d_i}$ **[mm]**	9.89	9.90
$\mathbf{t_i}$ **[mm]**	2.71	2.69
$\boldsymbol{\rho_i}$ **[g/cm^3]**	2.78	2.75
$\mathbf{RD_i}$ **[%]**	52.9	50.3
$\mathbf{m_f}$ **[mg]**	535.0	535.9
$\mathbf{d_f}$ **[mm]**	8.06	8.03
$\mathbf{t_f}$ **[mm]**	2.28	2.19
$\boldsymbol{\rho_f}$ **[g/cm^3]**	4.50	4.83
$\mathbf{RD_f}$ **[%]**	85.7	88.3

Table A.2: Pellet measurements for 1150@1h/BP2/Al_2O_3. m_i, d_i, t_i, ρ_i and RD_i are the initial mass, diameter, thickness, calculated density and relative density (before sintering), respectively. m_f, d_f, t_f, ρ_f and RD_f are the final mass, diameter, thickness, calculated density and relative density (after sintering), respectively.

Parameter	**Sample**			
	1150@1h/BP2/Al_2O_3			
	Ta = 0.25	Ta = 0.25	Ta = 0.6	Ta = 0.6
$\mathbf{m_i}$ **[mg]**	598.7	612.4	602.9	593.7
$\mathbf{d_i}$ **[mm]**	9.90	9.91	9.92	9.90
$\mathbf{t_i}$ **[mm]**	2.78	2.77	2.61	2.60
$\boldsymbol{\rho_i}$ **[g/cm^3]**	2.80	2.87	2.99	2.97
$\mathbf{RD_i}$ **[%]**	53.3	54.7	54.6	54.2
$\mathbf{m_f}$ **[mg]**	535.4	546.8	538.5	529.1
$\mathbf{d_f}$ **[mm]**	8.27	8.15	8.30	8.27
$\mathbf{t_f}$ **[mm]**	2.33	2.27	2.22	2.16
$\boldsymbol{\rho_f}$ **[g/cm^3]**	4.28	4.62	4.48	4.56
$\mathbf{RD_f}$ **[%]**	81.5	88.0	81.9	83.4

Table A.3: Pellet measurements for 1150@6h/BP2/Al_2O_3. m_i, d_i, t_i, ρ_i and RD_i are the initial mass, diameter, thickness, calculated density and relative density (before sintering), respectively. m_f, d_f, t_f, ρ_f and RD_f are the final mass, diameter, thickness, calculated density and relative density (after sintering), respectively.

Parameter	**Sample**	
	1150@6h/BP2/Al_2O_3	
	Ta = 0.25	Ta = 0.6
$\mathbf{m_i}$ **[mg]**	610.8	624.2
$\mathbf{d_i}$ **[mm]**	9.82	9.87
$\mathbf{t_i}$ **[mm]**	2.80	2.70
$\boldsymbol{\rho_i}$ **[g/cm^3]**	2.88	3.02
$\mathbf{RD_i}$ **[%]**	54.8	55.0
$\mathbf{m_f}$ **[mg]**	543.5	565.5
$\mathbf{d_f}$ **[mm]**	8.07	8.15
$\mathbf{t_f}$ **[mm]**	2.40	2.30
$\boldsymbol{\rho_f}$ **[g/cm^3]**	4.43	4.71
$\mathbf{RD_f}$ **[%]**	84.4	86.1

Table A.4: Pellet measurements for 1150@1h/BP2/MgO. m_i, d_i, t_i, ρ_i and RD_i are the initial mass, diameter, thickness, calculated density and relative density (before sintering), respectively. m_f, d_f, t_f, ρ_f and RD_f are the final mass, diameter, thickness, calculated density and relative density (after sintering), respectively.

Parameter	**Sample**			
	1150@1h/BP2/MgO			
	Ta = 0.25	Ta = 0.25	Ta = 0.6	Ta = 0.6
$\mathbf{m_i}$ **[mg]**	615.2	617.7	623.6	619.7
$\mathbf{d_i}$ **[mm]**	9.89	9.85	9.96	9.97
$\mathbf{t_i}$ **[mm]**	2.82	2.85	2.55	2.53
$\boldsymbol{\rho_i}$ **[g/cm^3]**	2.84	2.84	3.14	3.14
$\mathbf{RD_i}$ **[%]**	54.1	54.2	57.4	57.4
$\mathbf{m_f}$ **[mg]**	547.1	549.3	575.0	571.6
$\mathbf{d_f}$ **[mm]**	8.22	8.22	8.48	8.43
$\mathbf{t_f}$ **[mm]**	2.41	2.42	2.21	2.22
$\boldsymbol{\rho_f}$ **[g/cm^3]**	4.28	4.28	4.61	4.61
$\mathbf{RD_f}$ **[%]**	81.5	81.5	84.3	84.3

Table A.5: Pellet measurements for 1150@6h/BP2/MgO. m_i, d_i, t_i, ρ_i and RD_i are the initial mass, diameter, thickness, calculated density and relative density (before sintering), respectively. m_f, d_f, t_f, ρ_f and RD_f are the final mass, diameter, thickness, calculated density and relative density (after sintering), respectively.

Parameter	**Sample**			
	1150@6h/BP2/MgO			
	Ta = 0.25	Ta = 0.25	Ta = 0.6	Ta = 0.6
$\mathbf{m_i}$ **[mg]**	599.4	609.2	620.0	604.1
$\mathbf{d_i}$ **[mm]**	9.86	9.86	9.85	9.85
$\mathbf{t_i}$ **[mm]**	2.76	2.80	2.68	2.60
$\boldsymbol{\rho_i}$ **[g/cm^3]**	2.84	2.85	3.04	3.05
$\mathbf{RD_i}$ **[%]**	54.2	54.3	55.6	55.8
$\mathbf{m_f}$ **[mg]**	531.7	542.5	554.5	540.5
$\mathbf{d_f}$ **[mm]**	8.16	8.17	8.16	8.15
$\mathbf{t_f}$ **[mm]**	2.32	2.37	2.28	2.23
$\boldsymbol{\rho_f}$ **[g/cm^3]**	4.38	4.37	4.65	4.65
$\mathbf{RD_f}$ **[%]**	83.4	83.2	85.0	85.0

B Archimedes' method

Table B.1 presents the dey pellet mass before sintering together with the measurements taken during Archimedes' method for different samples and sintering programs.

Table B.1: Measurements established during the Archimedes' method for different samples and sintering programs. m_{dry} is the mass of the dry pellet after sintering, m_{sub} is the pellet mass while submerged in isopropanol, m_{wet} is the pellet mass with isopropanol in open pores, and ρ_{iso} is the calculated isopropanol density.

Sintering program	**Sample**	$\mathbf{m_{dry}}$ **[mg]**	$\mathbf{m_{sub}}$ **[mg]**	$\mathbf{m_{wet}}$ **[mg]**	$\boldsymbol{\rho_{iso}}$ **[g/cm^3]**
1150@1h/BP1/MgO	Ta=0.25	535.0	449.1	538.3	0.785
1150@1h/BP1/MgO	Ta=0.6	535.9	454.0	540.3	0.784
1150@1h/BP2/Al_2O_3	Ta=0.25	535.4	448.1	537.2	0.787
1150@1h/BP2/Al_2O_3	Ta=0.25	546.8	458.1	548.2	0.787
1150@1h/BP2/Al_2O_3	Ta=0.6	538.5	454.4	539.5	0.787
1150@1h/BP2/Al_2O_3	Ta=0.6	529.1	447.1	530.4	0.787
1150@6h/BP2/Al_2O_3	Ta=0.25	543.5	454.8	544.6	0.787
1150@6h/BP2/Al_2O_3	Ta=0.6	565.5	477.8	566.7	0.787
1150@1h/BP2/MgO	Ta=0.25	547.1	457.2	548.8	0.787
1150@1h/BP2/MgO	Ta=0.25	549.3	458.8	550.5	0.787
1150@1h/BP2/MgO	Ta=0.6	575.0	485.2	576.4	0.786
1150@1h/BP2/MgO	Ta=0.6	571.6	482.6	572.5	0.786
1150@6h/BP2/MgO	Ta=0.25	531.7	444.9	532.6	0.788
1150@6h/BP2/MgO	Ta=0.25	542.5	454.7	543.6	0.788
1150@6h/BP2/MgO	Ta=0.6	554.5	468.3	555.5	0.788
1150@6h/BP2/MgO	Ta=0.6	540.5	456.8	543.4	0.788

The relative density obtained from the Archimedes' method is calculated using the theoretical density, ρ_t [g/cm^3], and the bulk density, ρ_b [g/cm^3], for the cubic phase Ta-doped LLZO according to Equation A.3 and Equation A.4. The isopropanol density, ρ_{iso} [g/cm^3], is given by Equation B.1, where T_{iso} [°C] is the measured isopropanol temperature.

$$\rho_{iso} = -0.0009 \cdot T_{iso} + 0.8018 \tag{B.1}$$

The bulk density, ρ_b [g/cm^3], is calculated from the data in Table B.1, according to Equation B.2.

$$\rho_b = \frac{m_{dry}}{m_{wet} - m_{sub}} \cdot \rho_{iso} \tag{B.2}$$

The relative density, RD [%], can then be found according to Equation B.3.

$$RD = \frac{\rho_b}{\rho_t} \cdot 100\% \tag{B.3}$$

The open porosity, π_o [vol%], is calculated according to Equation B.4. The total porosity, π_t [vol%], is the sum of the open porosity and the closed porosity, and it is given in Equation B.5.

$$\pi_o = \frac{m_{wet} - m_{dry}}{m_{wet} - m_{sub}} \cdot 100\% \tag{B.4}$$

$$\pi_t = \frac{\rho_t - \rho_b}{\rho_t} \cdot 100\% = (1 - RD) \cdot 100\% \tag{B.5}$$

Table B.2 gives an overview of the relative density, open porosity, and total porosity resulting from Archimedes' method. The green density is also included.

Table B.2: Calculated densities and porosities for different samples and sintering programs. RD_i is the relative density of the green pellets, RD is the relative density obtained from Archimedes' method, π_o is the open porosity, and π_t is the total porosity.

Sintering program	**Sample**	$\mathbf{RD_i}$ [%]	**RD** [%]	$\boldsymbol{\pi_o}$ [vol%]	$\boldsymbol{\pi_t}$ [vol%]
1150@1h/BP1/MgO	Ta=0.25	52.9	89.6	3.7	10.4
1150@1h/BP1/MgO	Ta=0.6	50.3	89.1	5.1	10.9
1150@1h/BP2/Al_2O_3	Ta=0.25	53.3	90.0	2.0	10.0
1150@1h/BP2/Al_2O_3	Ta=0.25	54.7	91.0	1.6	9.0
1150@1h/BP2/Al_2O_3	Ta=0.6	54.6	91.0	1.2	9.0
1150@1h/BP2/Al_2O_3	Ta=0.6	54.2	91.4	1.6	8.6
1150@6h/BP2/Al_2O_3	Ta=0.25	54.8	90.7	1.2	9.3
1150@6h/BP2/Al_2O_3	Ta=0.6	55.0	91.5	1.4	8.5
1150@1h/BP2/MgO	Ta=0.25	54.1	89.5	1.9	10.5
1150@1h/BP2/MgO	Ta=0.25	54.2	89.7	1.3	10.3
1150@1h/BP2/MgO	Ta=0.6	57.4	90.7	1.5	9.3
1150@1h/BP2/MgO	Ta=0.6	57.4	91.4	1.0	8.6
1150@6h/BP2/MgO	Ta=0.25	54.2	90.9	1.0	9.1
1150@6h/BP2/MgO	Ta=0.25	54.3	91.5	1.2	8.5
1150@6h/BP2/MgO	Ta=0.6	55.6	91.6	1.1	8.4
1150@6h/BP2/MgO	Ta=0.6	55.8	92.0	1.1	8.0

C X-ray diffractograms

The X-ray diffraction patterns of as-received powders from spray pyrolysis are presented in Figure C.1. Both powders are composed of cubic Ta-doped LLZO, $La_2Zr_2O_3$ and Li_2CO_3. The amount of Li_2CO_3 is higher than it appears from the peak intensity due to the low scattering factor of Li-containing compounds. The measurements were previously performed by Herskedal [13].

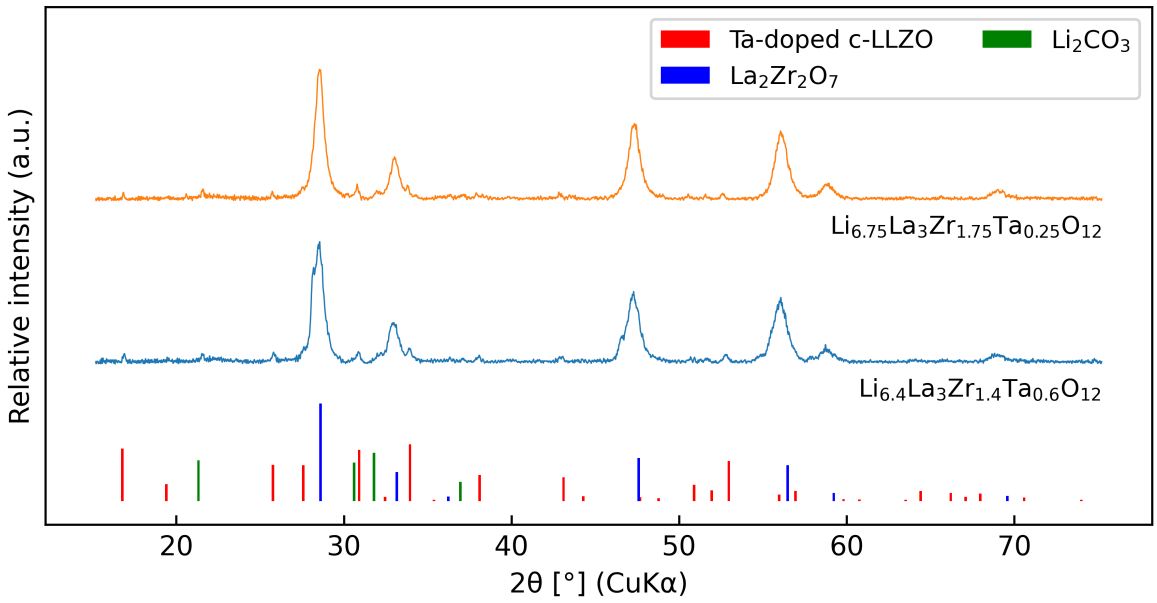

Figure C.1: X-ray diffraction patterns of as-received powders from spray pyrolysis. The peaks are indexed to cubic LLZTO, $La_2Zr_2O_3$ and Li_2CO_3. Previously measured by Herskedal [13].

Figure C.2 shows the X-ray diffraction pattern of the calcined $Li_{6.75}La_3Zr_{1.75}Ta_{0.25}O_{12}$ bed powder. The powder was calcined at 800 °C for 12 h in MgO crucibles. Batches of approximately 4 g of powder were used for each calcination. All peaks were indexed to the cubic phase of Ta-doped LLZO. The diffraction patterns are representative of all bed powders used in this work.

After calcination at 750 °C for 12 h, the powders were milled to remove agglomerates and reduce the particle size. The milling was carried out as described in Section 3.2.4. The X-ray diffraction patterns in Figure C.3 show the phase composition of the powders after milling. No secondary phases or impurities were present.

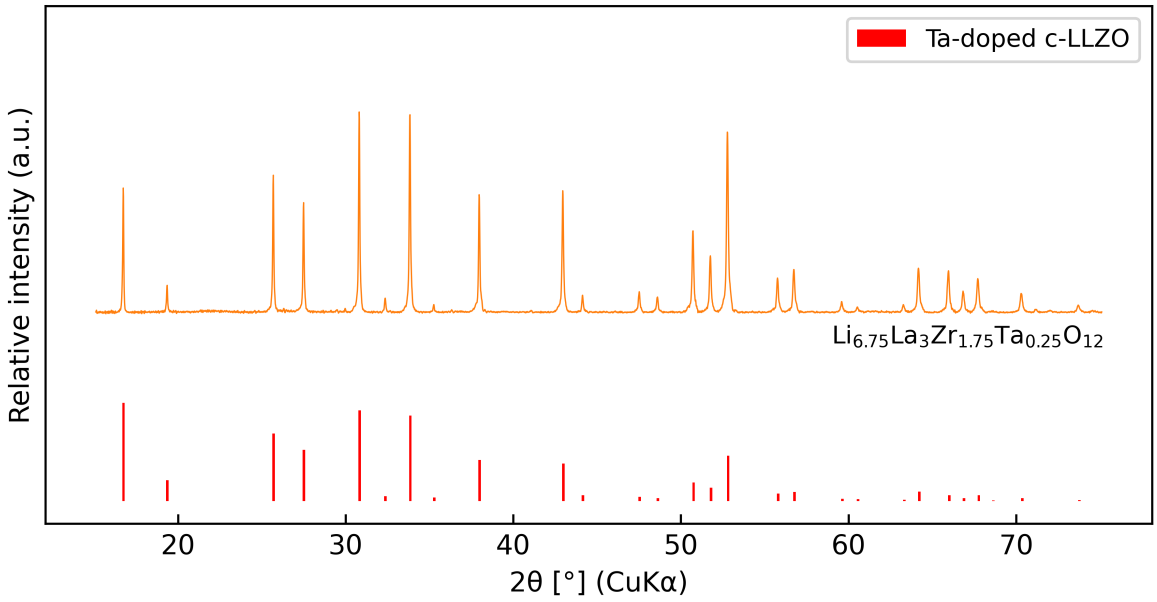

Figure C.2: Representaitve X-ray diffraction pattern of bed powder calcined at 800 °C for 12h in MgO crucibles. ll peaks are indexed to cubic Ta-doped LLZO.

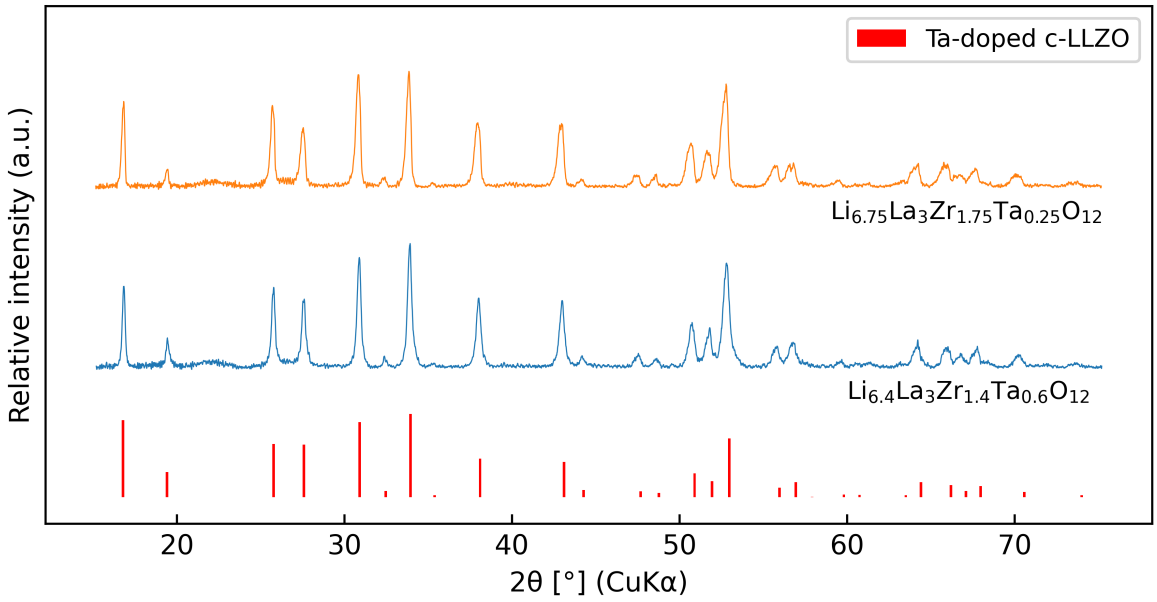

Figure C.3: X-ray diffraction patterns of the powders after calcination and milling. All peaks are indexed to cubic Ta-doped LLZO.

Figure C.4 shows the X-ray diffraction patterns of the preliminary sintering, where the pellets were sintered at 1150 °C for 1 h in MgO crucibles with a BP-ratio of 1. The insufficient amount of bed powder did not provide enough Li to compensate for the Li loss. Therefore, high amounts of $La_2Zr_2O_7$ were present in the samples.

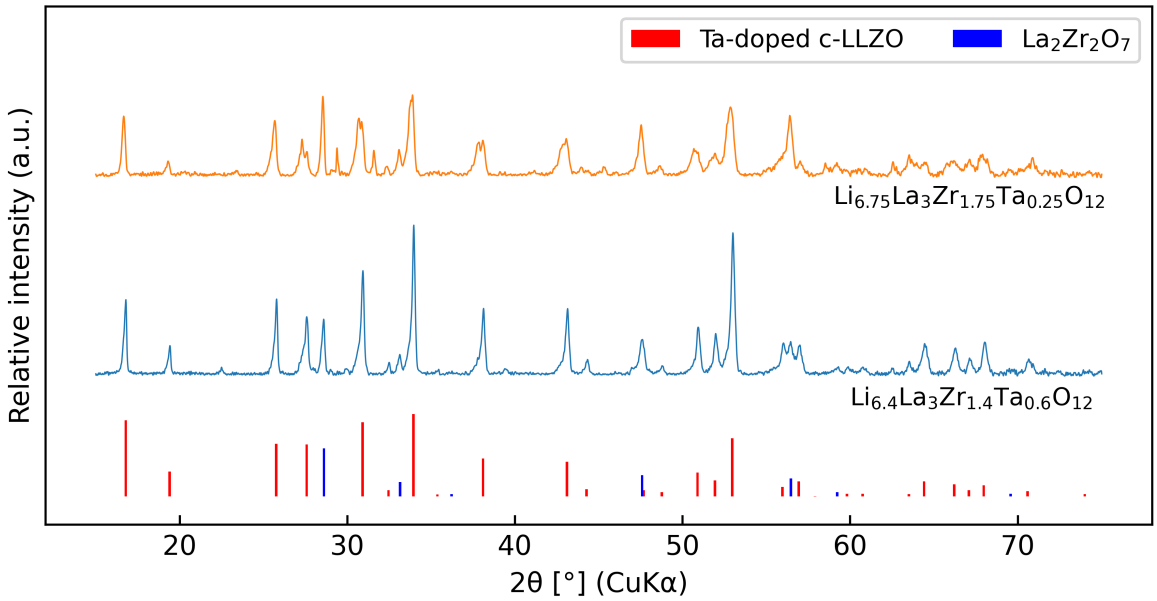

Figure C.4: Bulk representative X-ray diffraction pattern of samples sintered in the preliminary sintering study. The pellets were sintered at 1150 °C for 1 h in MgO crucibles with a BP-ratio of 1. The peaks are indexed to Ta-doped LLZO and $La_2Zr_2O_7$.

X-ray diffraction patterns of the pristine surface of pellets sintered in Al_2O_3 crucibles for the main sintering study are shown in Figure C.5. The samples were sintered at 1150 °C with a BP-ratio of 2. The holding times were 1 h and 6 h. The peaks are indexed to cubic or tetragonal Ta-doped LLZO, La_2O_3, and Li_4SiO_4.

Figure C.6 shows the X-ray diffraction patterns of the pristine surface of pellets sintered in MgO crucibles for the main sintering study. The samples were sintered at 1150 °C with a BP-ratio of 2 and holding times of 1 h and 6 h. The peaks are indexed to cubic or tetragonal Ta-doped LLZO, La_2O_3, and Li_4SiO_4.

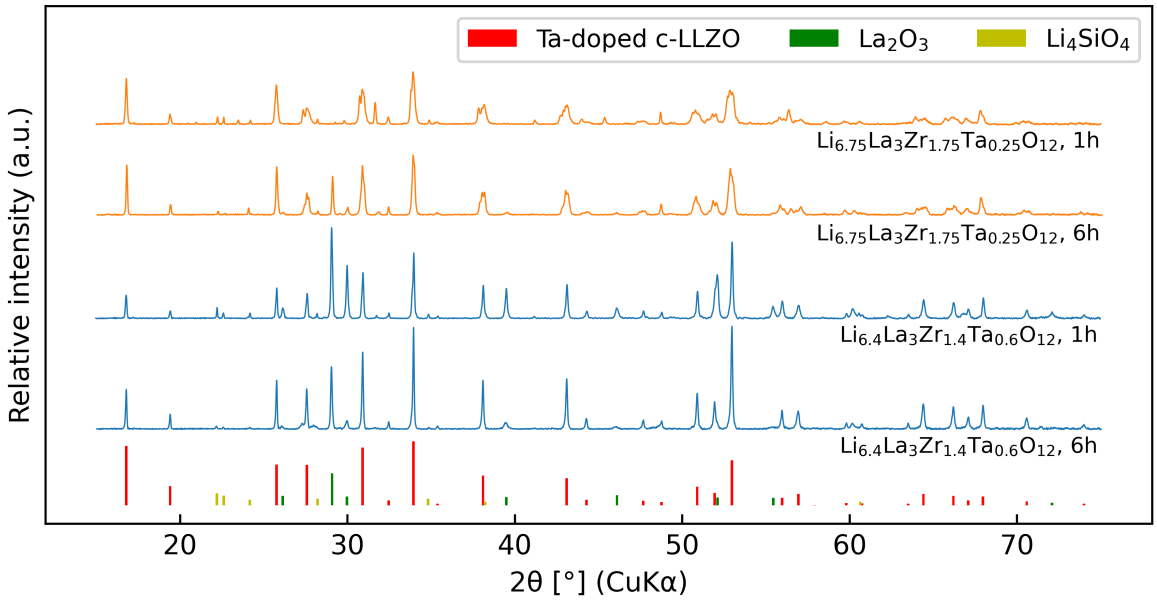

Figure C.5: X-ray diffraction patterns of the surface of pellets sintered at 1150 °C in Al_2O_3 crucibles. The BP-ratio is 2 and the holding times are 1 h and 6 h.

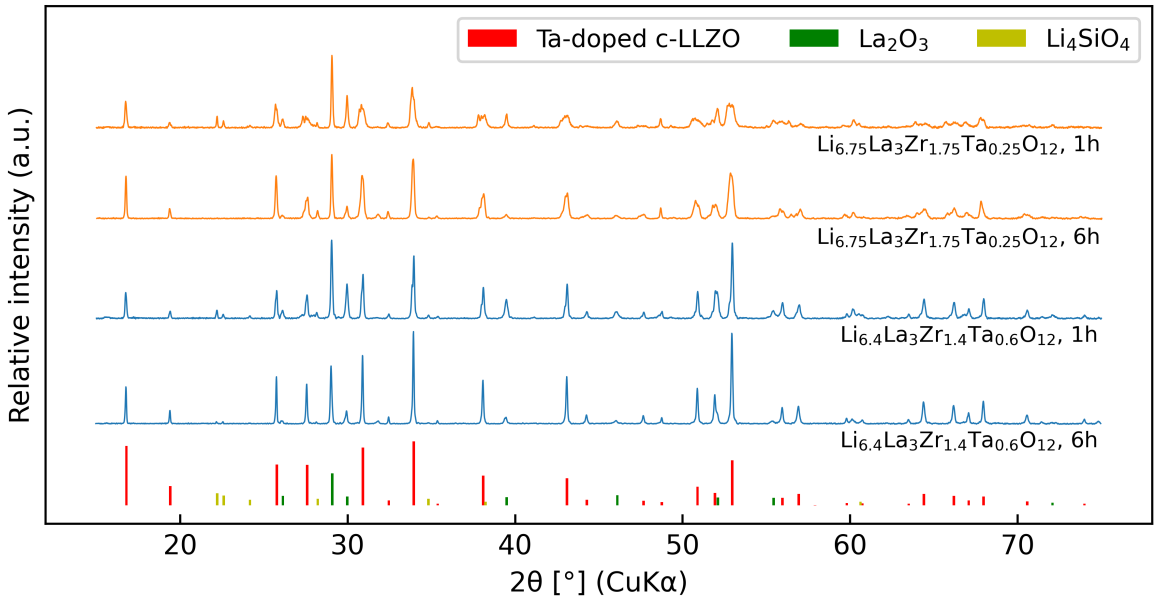

Figure C.6: X-ray diffraction patterns of the surface of pellets sintered at 1150 °C in MgO crucibles. The BP-ratio is 2 and the holding times are 1 h and 6 h.

D SEM micrographs

The micrographs in Figure D.1 present the microstructure of pristine fracture surfaces of pellets sintered at 1150 °C in Al_2O_3 crucibles with BP-ratio 2 and holding times of 1 h and 6 h. The grain size distribution is close to bimodal. Generally, transgranular fracture seems to take place in the larger grains, while intergranular fracture occurs in the smaller grains. The density of the samples sintered for 6 h appears to be higher than for the samples sintered for 1 h.

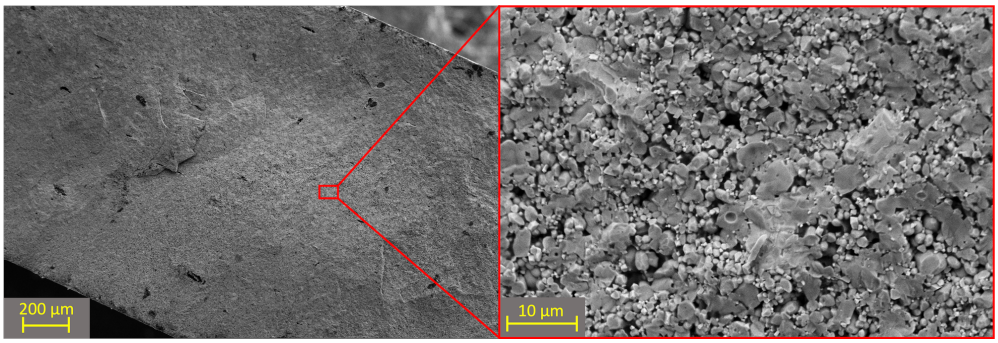

(a) Ta=0.25, 1150@1h/BP2/Al_2O_3 (b) Ta=0.25, 1150@1h/BP2/Al_2O_3

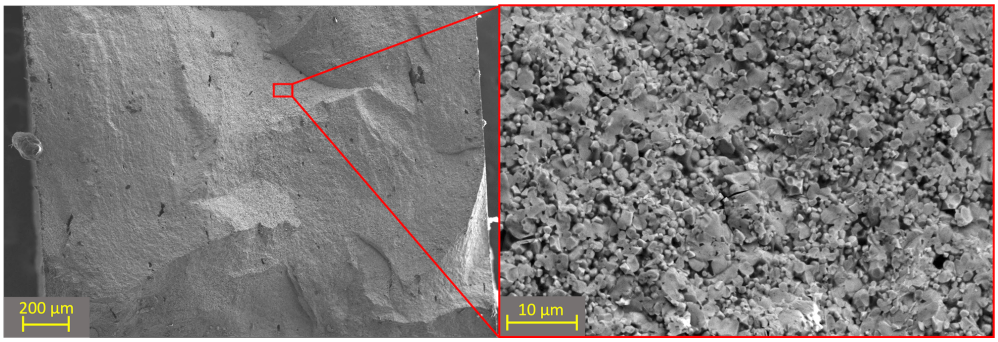

(c) Ta=0.25, 1150@6h/BP2/Al_2O_3 (d) Ta=0.25, 1150@6h/BP2/Al_2O_3

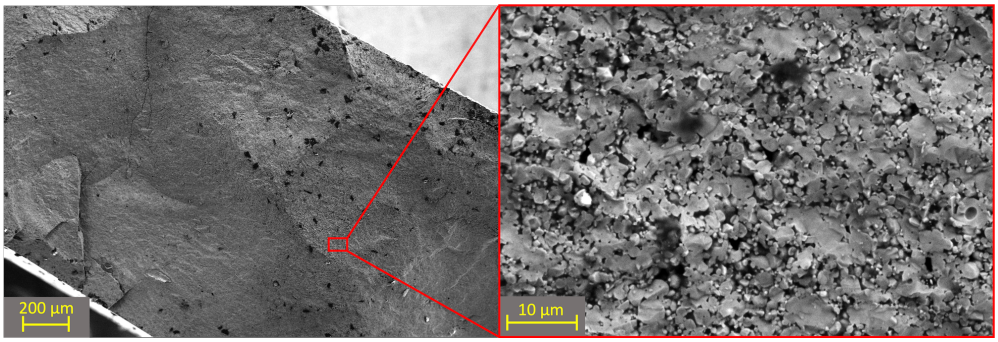

(e) Ta=0.6, 1150@1h/BP2/Al_2O_3 (f) Ta=0.6, 1150@1h/BP2/Al_2O_3

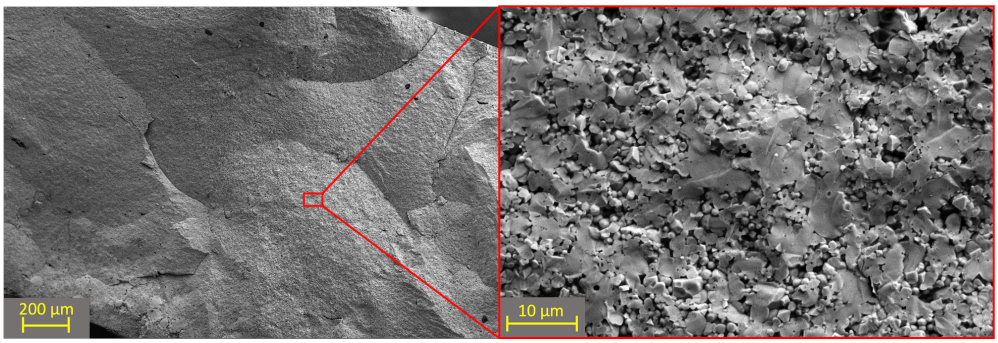

(g) Ta=0.6, 1150@6h/BP2/Al_2O_3 (h) Ta=0.6, 1150@6h/BP2/Al_2O_3

Figure D.1: Secondary electron micrographs of pristine fracture surfaces of $Li_{6.75}La_3Zr_{1.75}Ta_{0.25}O_{12}$ and $Li_{6.4}La_3Zr_{1.4}Ta_{0.6}O_{12}$ pellets sintered at 1150 °C in Al_2O_3 crucibles with BP-ratio 2. The holding times are 1 h and 6 h.

E Ionic conductivity calculations

The bulk ionic conductivity is calculated according to Equation E.1. The total ionic conductivity is calculated according to Equation E.2. t [cm] is the thickness of the sample, A [cm^2] is the surface area, and d [cm] is the diameter. R_1 [Ω] is the bulk resistance and R_2 [Ω] is the grain boundary resistance. The relevant equivalent circuit is shown in Figure 3.6b.

$$\sigma_b = \frac{t}{R_1 A} = \frac{4t}{R_1 \pi d^2} \tag{E.1}$$

$$\sigma_t = \frac{t}{(R_1 + R_2)\, A} = \frac{4t}{(R_1 + R_2)\, \pi d^2} \tag{E.2}$$

Table E.1 shows the bulk resistance and the grain boundary resistance obtained from the fitted EIS data. The table also provides the diameter and thickness of the samples. The total resistance for the circuit in Figure 3.6b is the sum of the bulk and grain boundary resistance.

Table E.1: Bulk resistance, R_1, grain boundary resistance, R_2, pellet diameter, d, and pellet thickness, t. The total resistance is R_1+R_2.

Sintering program	**Sample**	**R_1 [Ω]**	**R_2 [Ω]**	**d [mm]**	**t [mm]**
1150@1h/BP2/MgO	Ta=0.25	662	1112	8.22	1.41
1150@1h/BP2/MgO	Ta=0.6	946	1004	8.43	1.48
1150@6h/BP2/MgO	Ta=0.25	889	2123	8.17	1.84
1150@6h/BP2/MgO	Ta=0.6	980	1200	8.17	1.90

F Phase diagrams

The phase diagram of the Li_2O-Al_2O_3 system is shown in Figure F.1.

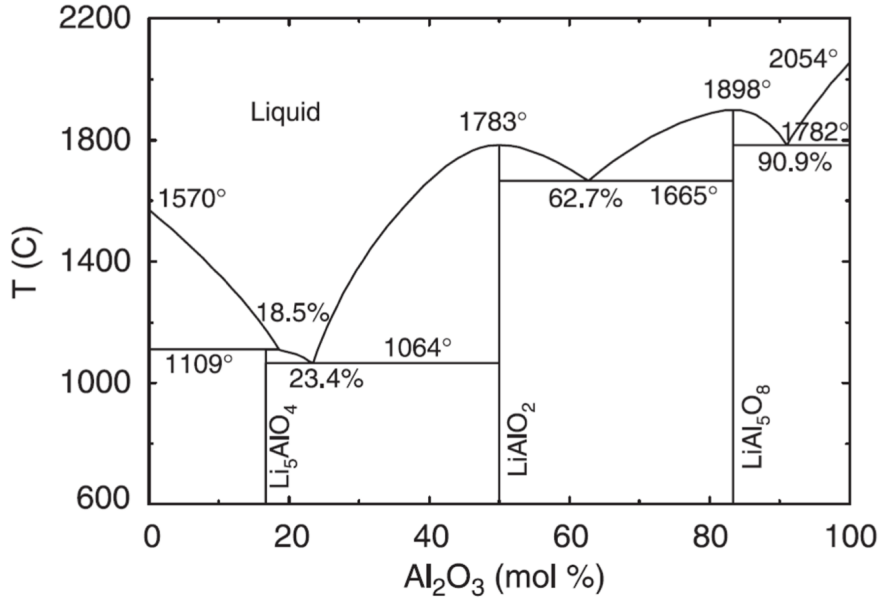

Figure F.1: Phase diagram of the Li_2O-Al_2O_3 system. Reprinted from [59].

The phase diagram of the Li_2O-SiO_2 system is shown in Figure F.2.

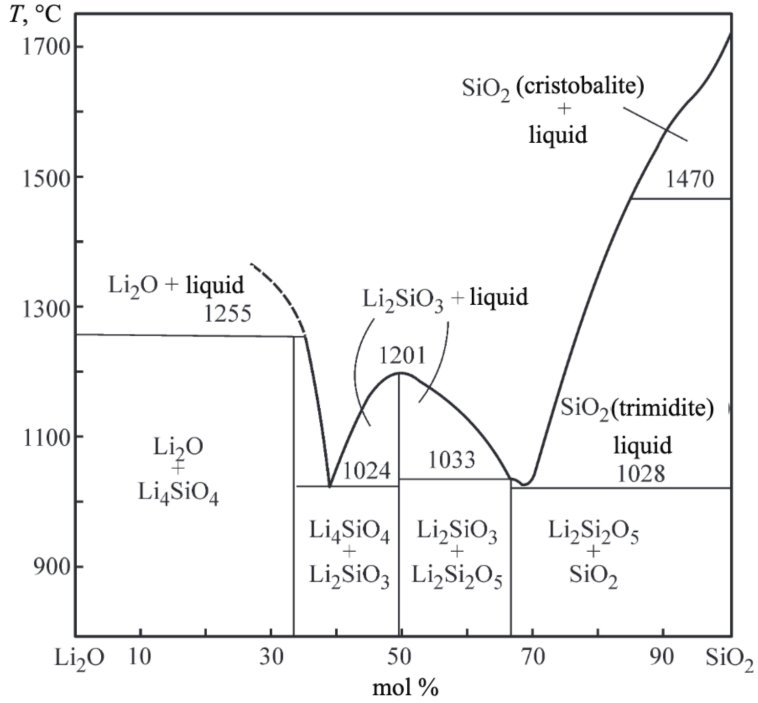

Figure F.2: Phase diagram of the Li_2O-SiO_2 system. Reprinted from [60].

G Crystal structure of LLZO

Unit cell models of the cubic and tetragonal phased LLZO crystal structures are shown in Figure G.1a and Figure G.1b, respectively. The main deviations between the cubic and tetragonal LLZO are the arrangement of Li ions and the site occupancy. The cubic structures of $Li_{6.75}La_3Zr_{1.75}Ta_{0.25}O_{12}$ and $Li_{6.4}La_3Zr_{1.4}Ta_{0.6}O_{12}$ are presented in Figure G.2a and Figure G.2b, respectively. These are different in terms of Ta content. All structures are obtained from the Vesta V3.4.8 software.

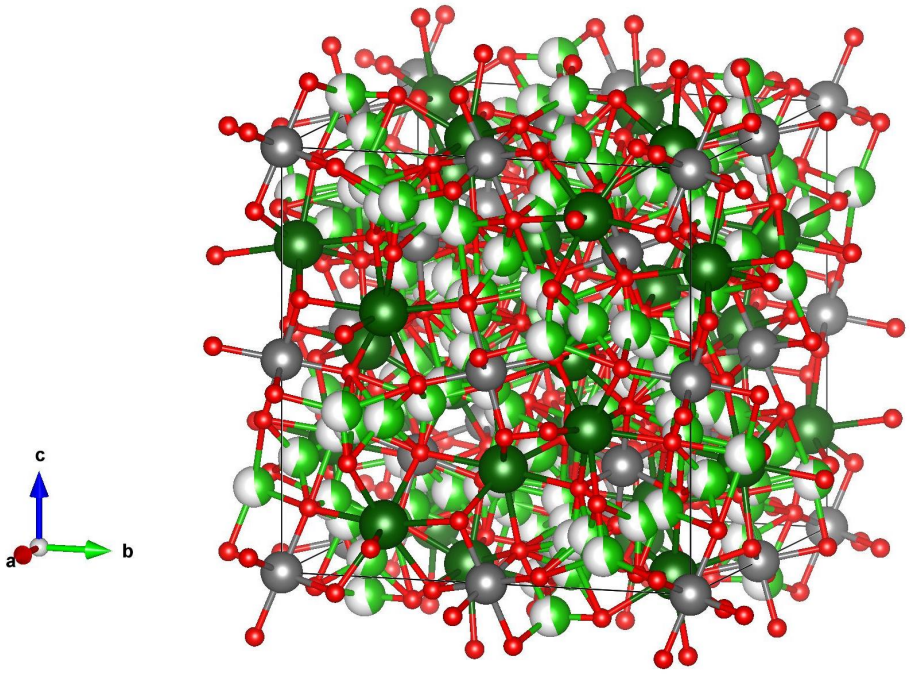

(a) Cubic LLZO

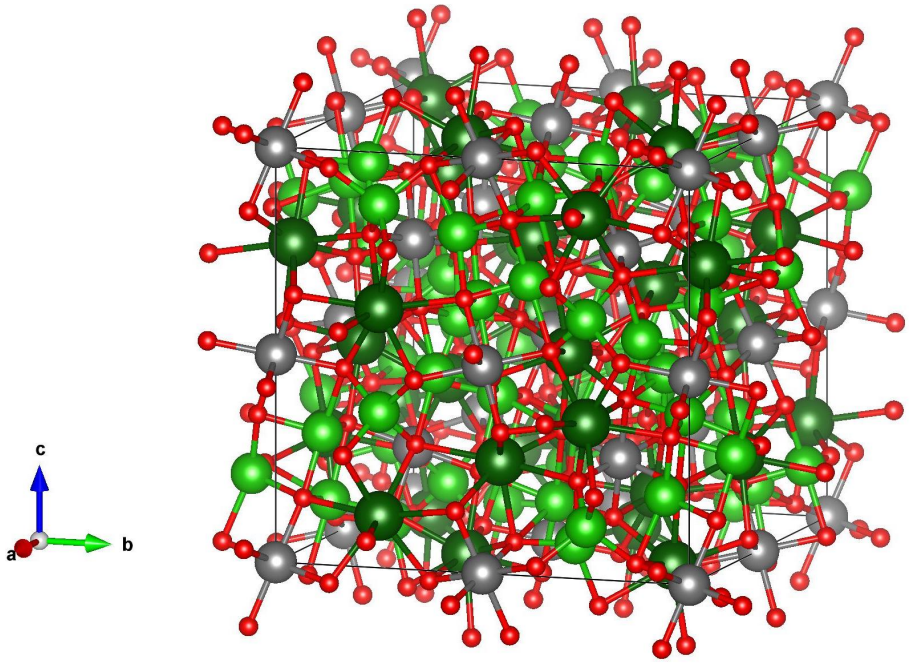

(b) Tetragonal LLZO

Figure G.1: Unit cell crystal structure of (a) cubic LLZO and (b) tetragonal LLZO. The colors represent different ions. Light green is Li, dark green is La, gray is Zr, and red is O. White represents the vacancies. Partially colored spheres are sites that are partially occupied, and the occupancy is denoted by the fraction of the corresponding color.

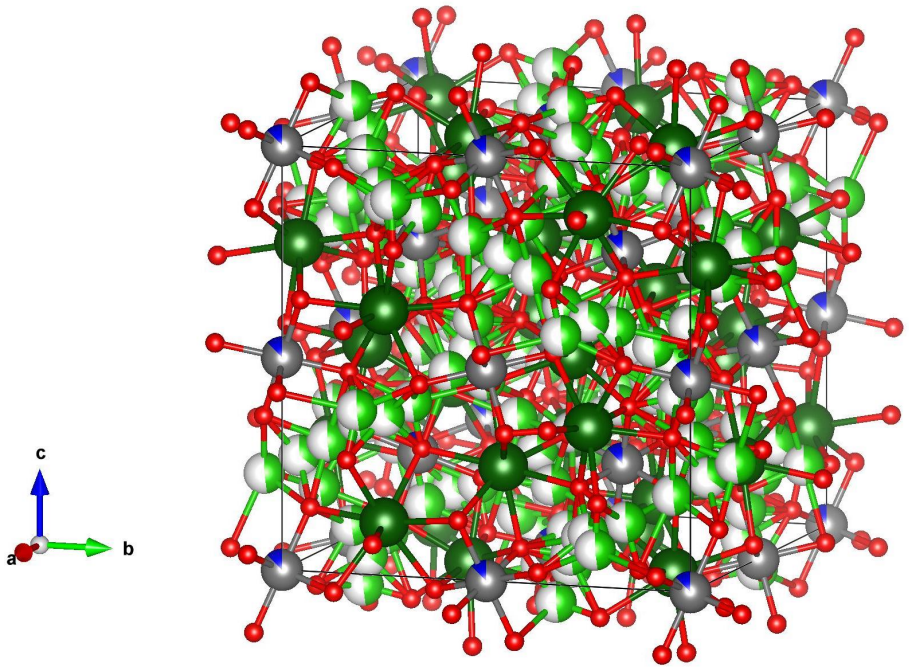

(a) Cubic $Li_{6.75}La_3Zr_{1.75}Ta_{0.25}O_{12}$

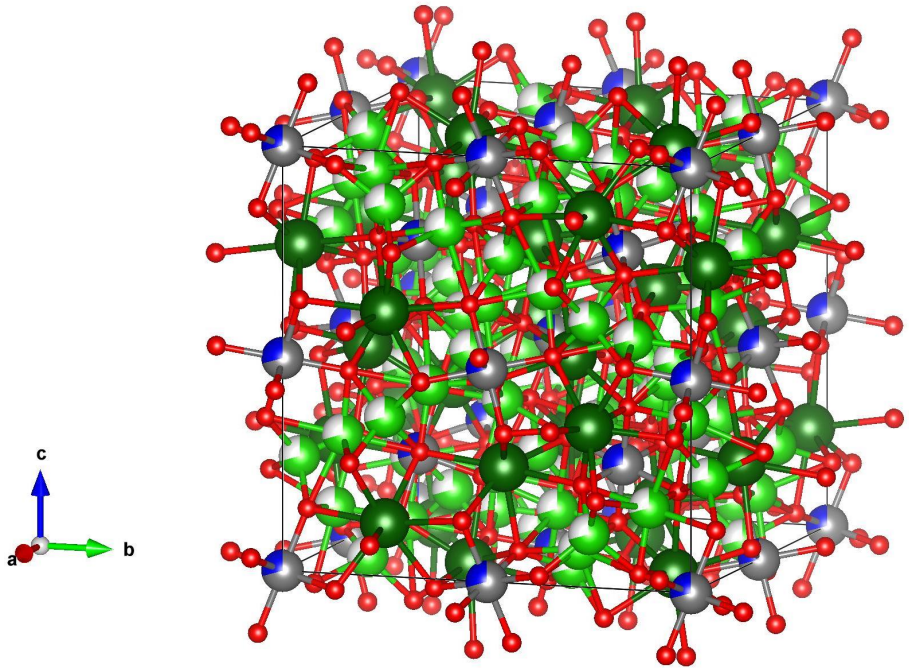

(b) Cubic $Li_{6.4}La_3Zr_{1.4}Ta_{0.6}O_{12}$

Figure G.2: Unit cell crystal structure of (a) cubic $Li_{6.75}La_3Zr_{1.75}Ta_{0.25}O_{12}$ and (b) cubic $Li_{6.4}La_3Zr_{1.4}Ta_{0.6}O_{12}$. The colors represent different ions. Light green is Li, dark green is La, gray is Zr, red is O, and blue is Ta. White represents the vacancies. Partially colored spheres are sites that are partially occupied, and the occupancy is denoted by the fraction of the corresponding color.

Hanna Kvam Herskedal

Master's Thesis

NTNU
Norwegian University of
Science and Technology